Simulating Heat Transfer in an Underground Thermal Storage Facility

MASTER THESIS

MAIERHOFER MATTHIAS

Department of Mineral Resources and Petroleum Engineering

Chair of Reservoir Engineering

University of Leoben

11/6/2013

I dedicate this report to my wife Judith

Eidesstattliche Erklärung

Ich erkläre an Eides statt, dass ich diese Arbeit selbständig verfasst, andere als die angegebenen Quellen und Hilfsmittel nicht benutzt und mich auch sonst keiner unerlaubten Hilfsmittel bedient habe.

Affidavit

I declare in lieu of oath, that I wrote this thesis and performed the associated research myself, using only literature cited in this volume.

11/06/2013	
Datum	Unterschrift

Abstract

To increase the efficiency of corn drying an underground thermal energy storage (UTES) facility stores waste heat from a combined heat and power unit (CHPU) during the summer to use it for corn drying in autumn. The storage consists of a high permeable gravel layer, which is bordered by an impermeable clay layer at the top and the bottom and two artificial cylindrical walls. The storage has a diameter of 33m and a height of 11m.

In this thesis, this real world system is replaced by a thermal reservoir simulator, in which a corn drying control system (CDCS) is implemented. The simulator is used to calculate transport of heat in the UTES during the charging and the discharging period and for the optimal determination of well locations and schedules to optimize the corn drying process.

The created simulator uses the CSMP++ software library and is based on the hybrid finite-element finite-volume discretization method. This numerical scheme combines the robustness of FVM in solving advection - dominated problems, with the capability of FEM to handle diffusion-dominated problems. The simulator is verified by comparing the numerical solution with analytical ones, as well as benchmarking it against TOUGH ("Transport of Unsaturated Groundwater and Heat") simulator and the PHT ("Pressure Enthalpy Temperature") simulator. PHT is a compressible flow simulator, also generated from the CSMP++ libraries.

Simulations prove that production wells during the controlled discharge period should be located near the top, and the injection wells near the bottom. Whenever possible, distance between wells should be maximized to prevent thermal breakthrough for as long as possible. The charging and discharging period should both be carried out at the highest possible rate to reduce diffusive heat loss. The highest energy output is thus achieved by charging the UTES with hot water at one well at the top section and discharging the storage from the same well. In such a scenario, composed by four months of charging followed by two months of discharging, fifty percent efficiency may be achieved.

The simulator created and described in this thesis provides a useful and computationally efficient tool to design UTES systems.

Kurzfassung

Um den Wärmetransport in einem oberflächennahen Wärmespeicher zu modellieren, wurde ein Simulator basierend auf der Boussinesq - Annahme in der CSMP++ Entwicklungsumgebung entwickelt. Der Wärmespeicher sollte zusätzliche Energie für die Maistrocknung eines Energielandwirtes zur Verfügung stellen. Um die Maistrocknung zu optimieren, wird mit Hilfe des Simulators das detaillierte Temperaturfeld im Speicher während der Be- und Entladung ermittelt. Diese Information ermöglicht eine effektive Entladung des Speichers.

Die verwendete numerische Simulationssoftware verwendet einen Hybridsimulationsansatz, welche den konduktiven Wärmefluss mit der Finiten Element Methode und den advektiven mit der Finiten Volumen Methode simuliert. Der Simulator wurde durch Benchmark-Tests verifiziert.

Die Simulationsergebnisse zeigen konduktiven und advektiven Wärmetransport während der Be- und Entladung des Speichers. Die wärmsten Stellen sind im oberen Bereich des Speichers, daher ist während der Entladung darauf zu achten, dass sich die Fördersonden im oberen Bereich des Speichers befinden. Die Einlasssonden befinden sich im unteren Bereich des Speichers. Weiters befinden sich diese Sonden in der Nähe der Speicherwand, um eine möglichst weite Distanz zwischen Einlass- und Fördersonde zu erhalten.

Be- und Entladung sollten so schnell wie möglich, sprich mit der höchsten Rate, durchgeführt werden, um den Wärmeverlust zu reduzieren. Die höchste Energieausbeute wird erzielt, wenn der Speicher im oberen Bereich beladen und entladen wird. Mit dieser Konfiguration konnten etwa 680 MWh an Energie dem Speicher während der 4-monatigen Beladung zugeführt werden. Davon konnten 340 MWh an Energie während der Entladung der Maistrocknung zugeführt werden. Dies ergibt eine Effizienz von etwa 50%.

Acknowledgements

I would like to thank the following people: Julian Mindel for supervising my thesis and constant support, Florian Aichinger from ADS for his constant support and explanations, Roman Manasipov for his help with C++ programming, Alina Yapparova for her support to create the geothermal simulator and Siroos Azizmohammadi for answering my questions.

I am also grateful to Advanced Drilling Solutions GmbH and the "Österreichische Forschungsförderungsgesellschaft", for their funding support.

Most of all I want to thank my wife Judith, whose love and patience got me through this thesis. Thank you very much for your permanent support.

Table of Contents

1. Introduction 1

2. Background 6

2.1 Types of UTES 6

2.2 Numerical modeling of UTES systems 9

3. Methodology 11

3.1 Conceptual model of the storage system 11

3.1.1 Fluid flow in porous media 11

3.1.2 Thermal conduction and convection 12

3.2 Process inventory 13

3.2.1 Thermal reservoir simulator 13

3.2.2 Corn drying control system 14

3.3 Mathematical description of the conceptual model 18

3.3.1 Governing Equations 18

3.3.2 Simplifying assumptions 21

3.4 Discretization approach of the governing equations via Hybrid FE-FV method 23

3.4.1 Numerical discretization of the pressure equation 24

3.4.2 Numerical discretization of the temperature advection-diffusion equation 25

3.5 Verification and benchmark cases 27

3.5.1 Comparison cases excluding gravity effects 27

3.5.2 Comparison cases including gravity effects 29

3.6 Pseudo codes 32

3.7 Model setup 34

3.7.1 Geology of the projected test site 34

3.7.2 Geometry and geometric discretization 36

3.7.3 Model properties and essential conditions 39

3.7.4 Model setup for the simulations with the CDCS 40

4. Results 43

4.1 Simulations without the CDCS 43

4.2 Simulations with the CDCS 60

5. Discussion 76

6. Conclusions 78

7. Outlook 80

8. References 81

A.1 Dimensionless Numbers 85

List of Figures

Fig. 1.1: Facility overview of the biogas plant. 2
Fig. 1.2: Heating energy utilization. 3
Fig. 2.1 Classification of UTES systems regarding heat transfer mode. 6
Fig. 2.2. Scheme of a central solar heating plant with seasonal storage. 7
Fig. 2.3. Construction types of UTES 7
Fig. 2.4. Cavern thermal energy storage and gravel-water pit. 8
Fig. 2.5. Hybrid storage 9
Fig. 3.1: Sketch of the corn drying facility 15
Fig. 3.2: Corn drying principle 16
Fig. 3.3: Communication between the thermal simulator and the CDCS 17
Fig. 3.4: Hybrid finite element finite volume grid 25
Fig. 3.5. Comparison between the analytical and the numerical solution 27
Fig. 3.6: Comparison between TOUGH, CSMP_PHT and CSMP_Boussinesq results 29
Fig. 3.7: Comparison via the L∞-norm 31
Fig. 3.8: Frequency plot of absolute error ranges 31
Fig. 3.9: Cross section through the expected site near - surface geology 34
Fig. 3.10. Geometric and material description of the storage system 35
Fig. 3.11: Dimensions of the storage system 36
Fig. 3.12: Vertical cross section of the storage after the meshing process 37
Fig. 3.13: Horizontal middle y-plane mesh cross section of the storage system 38
Fig. 3.14: Zoomed in vertical cross section view of the material interfaces. 38
Fig. 3.15: Graphical description of the three operation modes for discharging 42
Fig. 4.1: Temperature cross section after 1 day for Run 1 44
Fig. 4.2: Temperature cross section after 45 days for Run 1 45
Fig. 4.3: Temperature cross section after 90 days for Run 1 46
Fig. 4.4: Groundwater flow around the storage system 47
Fig. 4.5: Velocity vectors and pressure contours for Run 1 48
Fig. 4.6: Monitored temperature at production well 3 49
Fig. 4.7: Energy and exergy flow rate over the 90 days charging period 51
Fig. 4.8: Integrated heat flux and total heat transferred 52
Fig. 4.9: Temperature cross after 90 days for Run 5 53
Fig. 4.10: Temperature vs. time at production well 3 54
Fig. 4.11: Integrated heat flux and total heat transferred. 55
Fig. 4.12: Temperature cross section at a vertical cut plane for Run 6 57
Fig. 4.13: Temperature profile at different wel locations 57
Fig. 4.14: Integrated heat flux and total heat transferred for Run 6 59
Fig. 4.15: Temperature cross section and velocity vectors during discharging for Run 1 61
Fig. 4.16: Temperature cross section and velocity after 42 days of discharging for Run 1 62
Fig. 4.17: Temperature cross section and velocity after 20 days of discharging for Run 2 64

Fig. 4.18: Temperature cross section and velocity after 56 days of discharging for Run 2 65
Fig. 4.19: Temperature cross section of discharging for Run 3 67
Fig. 4.20: Temperature cross section and velocity vectors for Run 5 68
Fig. 4.21: Temperature cross section and velocity vectors for Run 6 70
Fig. 4.22: Energy and exergy flow rate over the 120 days charging period for Run 2 - 6 71
Fig. 4.23: Temperature at the production well(s) during the discharging period for Run 1 - 6 72
Fig. 4.24: Energy and exergy flow rate during the discharging period 74

List of Tables

Table 3.1: Rock and fluid parameters and boundary conditions for benchmark 28
Table 3.2: Fluid parameters, material properties for gravity-driven benchmark test case. 30
Table 3.3: Boundary conditions for gravity-driven benchmark test case. 30
Table 4.1: Material properties for the loess, gravel, wall and clay marl region. 39
Table 4.2: Fluid properties for water at 40°C 39
Table 4.3: Essential conditions for Run 1 - 6 40
Table 4.4: Fluid properties for water at 55°C 40
Table 4.5: Three operation modes for discharging 41
Table 5.1 - Table 5.8: Simulation parameters 43
Table 5.9: Energy analyses of the storage system for Run 1 - 6 75
Table 5.10: Exergy analyses of the storage system for Run 1 - 6 75

Abbreviations

ATES	Aquifer Thermal Energy Storage
BTES	Borehole Thermal Energy Storage
CDCS	Corn Drying Control System
CHPU	Combined Heat and Power Unit
CSP/CSMP	Complex System Modeling Platform
CTES	Cavern Thermal Energy Storage
EOS	Equation of State
FD	Finite Difference
FE	Finite Element
FV	Finite Volume
IMPIS	Implicit Pressure Implicit Saturation
PTES	Pit Thermal Energy Storage
SSTES	Seasonal Solar Thermal Energy Storage
TRNSYS	Transient System Simulation Program
TTES	Tank Thermal Energy Storage
UTES	Underground Thermal Energy Storage

Nomenclature

Symbols

c	specific heat, J/kg·K
c_p	specific heat at constant pressure, J/kg·K
E	total energy, J
g	acceleration due to gravity, m/s^2
H	enthalpy per unit mass (specific enthalpy), J/kg
k	permeability, m^2
L	Length (along a heat flow path), m
$\dot{m}$	mass flow rate, kg/s
p	pressure, Pa
Q	quantity of heat, J
q''	heat flux per unit area, W/m^2
T	temperature, K or °C
t	time, s
v	flow velocity, m/s
v_D	Darcy velocity, m/s
W	work, J
x	distance, m

β	temperature coefficient of thermal expansion, 1/K
λ	thermal conductivity, W/m·K
$\varkappa_m$	thermal diffusivity, m^2/s
μ	dynamic viscosity, Pa·s
ν	kinematic viscosity, m^2/s
ρ	mass density, kg/m^3
σ	heat capacity ratio
τ	(viscous) momentum flux tensor, N/m^2
ϕ	porosity
η	energy efficiency
ψ	exergy efficiency

Subscripts

m	media
s	solid
f	fluid
inj	injection
prod	production

1. Introduction

Heat storage for thermal solar energy applications and biogas plants is a way to compensate the time shift between heat production and energy consumption. Fluctuating energy sources, like solar thermal energy, generate energy supply at different times from the demand. Energy is produced during the warm season of the year, but consumed for heating during the cold season. Due to the time lag between energy production and consumption, a thermal energy storage is required to avoid wasting energy during peak power generation periods. Energy that would otherwise be wasted is stored by warming up water, can be introduced into an underground thermal energy storage (UTES) facility to reduce loss. At times of high energy demand, the warm water from this storage can be re-circulated, thus recovering the leftover energy (Lindblom, 1980; Novo et al., 2010).

Over the past decades, computer simulation has increasingly become a reliable and cost effective tool for designing and optimizing in many engineering areas. Different approaches also exist for simulating UTES systems. Ucar and Inalli (2005), applied the finite element simulation software ANSYS to model the transient heat transfer between a seasonal storage facility and the surrounding ground to develop different types of central solar heating plants with the storage. Sweet and McLeskey Jr. (2012), simulated a system that stores solar energy collected during the summer for use during the following winter. TRNSYS simulates the transient behavior of thermal energy systems and has been used to simulate the whole process, including the thermal load of a typical home, the gained energy from the solar collectors, and the storage system. In addition to standard TRNSYS components, so called TYPEs, are developed by different authors. Type 342 (Eftring and Hellström, 1989) was chosen to simulate a seasonal solar thermal energy storage bed and is capable of simulating heat storage in a cylindrical water filled tank in the ground. This tank is charged with hot water that is injected at the top and cold water that is produced at the bottom and for discharging cold water is injected at the bottom and hot water is produced from the top. Urbaneck et al. (2002), simulated a gravel-water pit using TRNSYS. Type 343 (Hornberger, 1997) has been used which is applicable for vertically stratified storage bed for heat and cold storage. They investigate large-scale flow currents, which has negative effects to the thermal stratification in the storage. A higher

permeability in the upper and lower section of the storage can work against these currents. Papanicolaou and Belessiotis (2009), studied the charging process in an UTES for thermal solar energy. A linear temperature profile with decreasing values from top to bottom is observed. Yumrutas (2000), presents an analytical and computational model to determine the performance of a solar space heating system with an UTES. They found out that earth with lower thermal conductivity gives better annual system performance. The storage radius and the burial depth have only small effects on the performance.

It must be mentioned, that although there is much research about the performance of UTES with central solar heating plants, there are very few reports about the efficiency of UTES with biogas plants and their optimization.

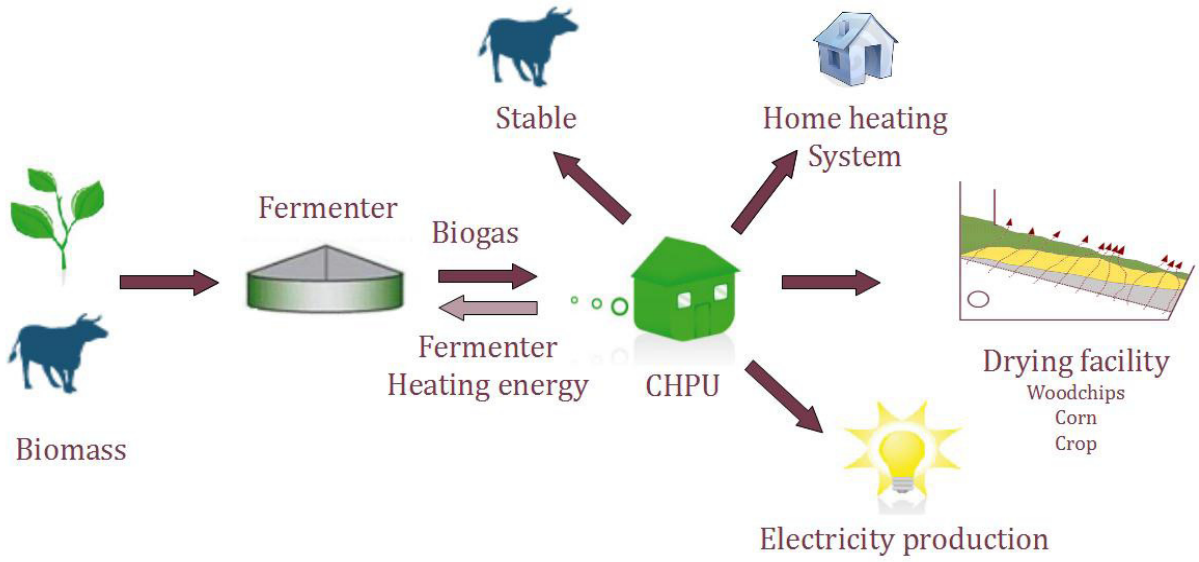

Fig. 1.1: Facility overview of the biogas plant. Biogas from the fermenter is converted to electricity and heat in the CHPU. Most of the heat is used for the drying facility.

My Master's thesis is encompassed by a longer term construction project, where a biogas plant is envisaged to connect with an underground thermal energy storage (UTES) facility to use the waste heat from the combined heat and power unit (CHPU) more efficiently (a CHPU is a power station that generates simultaneously electricity and useful heat) (Fig. 1.1). The biogas plant provides 330 kW of electrical and 500

kW of thermal power. The thermal power is used for domestic and fermenter heating, and for drying of corn, crops and woodchips. The situation is such, that a certain amount of energy is unused from June until September. It would be more efficient to store this waste heat in a UTES and use it for corn drying in autumn (Fig. 1.2), as no heating oil would be required for the corn drying. Further excess capacity could be used for drying woodchips.

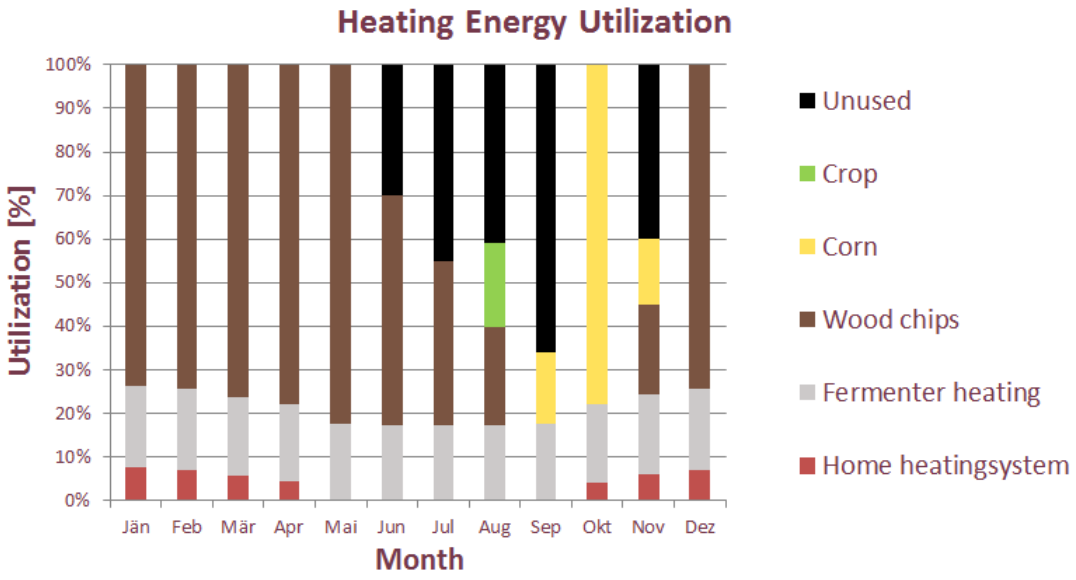

Fig. 1.2: Heating Energy Utilization. Unused energy in summer shall be used to increase the corn drying capacity in October.

To analyze the viability of this process, a thermal reservoir simulator can be used to predict real-world behavior. This is particularly the case when a high degree of detail is required and a high number of variables are in question. In such cases, analytical means might not provide adequate results, and experimental means could prove to be very costly.

A thermal reservoir simulation is needed to understand the heat transport in the storage system, and thus to charge and discharge the storage in a most efficient manner. It can also be used to identify locations, causes and magnitudes of design-related heat losses and help to develop operation strategies. It is also possible to vary input parameters, like flow rate, injection temperature, thermal and rock conditions to investigate different physical phenomena and their impact on efficiency. This sensitivity analysis recognizes the overall control system response, and thus the

storage may be better integrated (Dincer and Rosen, 2002; Reuß, 2003). Another advantage of numerical analysis is observability, where pressure, temperature, velocity and other important parameters can be sampled at any spatial and temporal point in the system.

For the purpose of optimization, the reservoir simulator must be part of an iterative program that simulates real world usage of the storage facility. In all iterations (i.e a change in the number and location of available wells) the CDCS has to account for daily and seasonal changes that affects the corn drying process. The first iteration would thus start with a certain well configuration for injection and production. While the simulation runs, the CDCS monitors the discharge temperature amongst other external variables (e.g. outside air temperature), and uses the information to fine-tune the well schedule. The CDCS can be set to monitor continuously, or at time intervals relevant to a real-world system, always in an attempt to optimize the corn drying process. After the cycle of charging and discharging finishes, an analysis must be made based on the simulated data to either arrive at the conclusion that the configuration is efficient enough, or that a new iteration must take place (i.e. well related change) to produce better results.

In this thesis, I perform a number of optimization iterations. Each iteration leads to a different simulation of a charge and discharge cycle, where the overall geometry of the UTES has been kept constant, while varying the well schedule. In each case, I simulate fluid flow and heat transfer in a three-dimensional model of an underground thermal energy storage system to optimize the corn drying process.

Chapter 2 provides a brief background on different types of storage facilities and discusses numerical simulation of heat transport in such geothermal storage facilities. The methodology used for simulation in this thesis is presented in Chapter 3, beginning with the description of the conceptual model and including governing equations and simplifying assumptions. I later discuss the usage of these assumptions for geothermal systems where the fluid flow is dominated by buoyancy forces and describe other simplifications (Ingerbritsen and Sanford, 1998). Verification and benchmarking cases of the solution approach for simulation are also presented. The final section of chapter 3 provides the model setup, including its planned geological site, the storage geometry, material properties, and the geometric discretization. Simulation results and the performance of the system are presented in

Chapter 4. I conclude my thesis with a discussion of my findings in Chapter 5. Conclusions and outlook are given in Chapter 6 and 7.

2. Background

Systems which use the natural underground for thermal energy storage are called Underground Thermal Energy Storage (UTES). Heat is usually stored underground and relatively close to the surface (Bakema et al., 1995; Novo et al., 2010). UTES can be classified depending on the type of heat transfer in convective, conductive and combined storage systems (Fig. 2.1).

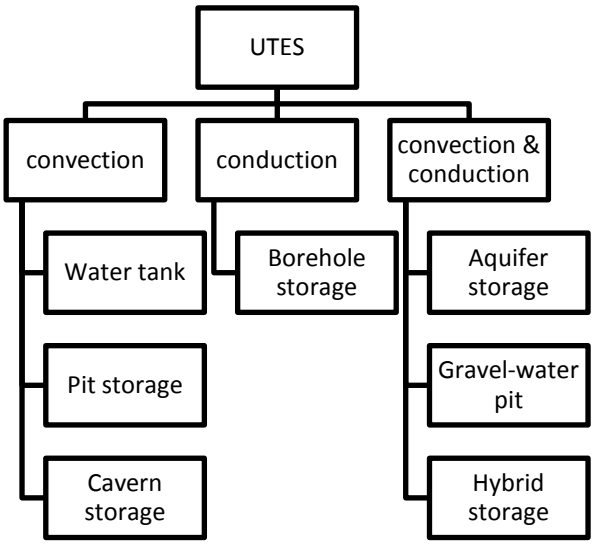

Fig. 2.1 Classification of UTES systems regarding heat transfer mode. Water tank and pit storage, cavern storage, borehole storage, aquifer storage, gravel-water pits and hybrid storage systems. The latter can be used in combination with biogas plants. Factors which have major influence in the selection of the proper storage are the geology, the temperature ranges and the storage volume. While potential heat loss depends largely on storage volume, it also affected by the geometric design and the location of the charging and discharging wells (Bakema et al., 1995).

2.1 Types of UTES

Depending on the storage time requirements, heat storage can be classified in short-term storage and long-term or seasonal storage. In the first type, the stored fluid is kept at high temperatures (maximum 95 °C) from a few hours to maximum one week. The storage requirement for seasonal storage is up to three or four months and lower

temperatures are used than in short-term storage. Heat pumps are used to raise the temperature of water (Fig. 2.2).

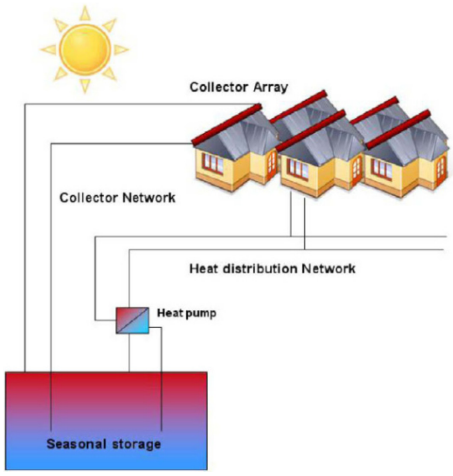

Fig. 2.2. Scheme of a central solar heating plant with seasonal storage. The main components are the collector array, the heat storage unit, the heat pump and the piping network (fig. 1 of Novo et al., 2010)

Water tank (TTES) and pit storage (PTES) are artificial structures built below the ground and used predominantly as high temperature storage systems. Therefore a good thermal insulation is necessary. Most of them are constructed with concrete and have different shapes (Fig. 2.3a, b).

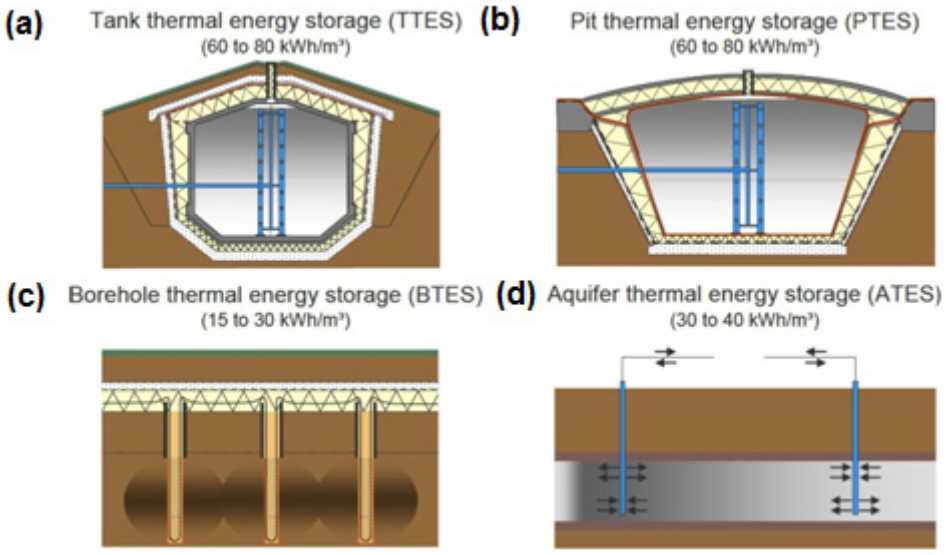

Fig. 2.3. Construction types of UTES. a) TTES and b) PTES are built with artificial structures below the ground. C) BTES uses vertical heat exchangers for heat transfer. d) ATES uses the natural underground as storage medium (Schmidt, 2007).

Borehole storage (BTES) uses vertical heat exchangers, which are inserted deeply below the soil to ensure the transfer of thermal energy from the ground (Fig. 2.3c). Adequate undergrounds are saturated clays with no or few groundwater motion. The typical diameter of injection and production well is between 100 to 150 mm, the distance between them is about 1.5 to 4 m and the depth ranges from 20 to 100 m. Only big storage systems (> 50 000 m^3) are feasible, because there is just an insulation at the top possible (Schmidt, 2005).

Aquifer storage (ATES) uses natural water in a saturated and permeable underground layer and the rock matrix as the storage medium (Fig. 2.3d). The transfer of thermal energy is carried out by discharging groundwater from the aquifer and by re-injecting it, after harnessing the stored energy, at a different temperature in a nearby well. In the summer, hot water is injected and cold water is extracted. In the winter the system works vice versa. The requirements for such storage systems are hydrogeological and hydro-chemical conditions which avoid precipitation.

Cavern thermal energy storage (CTES), where large underground water reservoirs serve as thermal energy storage systems, are shown in Fig. 2.4a. A basic requirement is a homogeneous rock without fractures to avoid leakage.

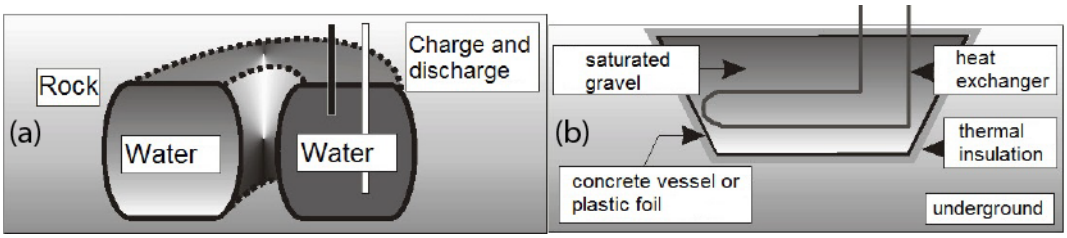

Fig. 2.4. (a) Cavern thermal energy storage. (b) Gravel-water pit (figs. 4 and 7 of Reuß, 2003).

Gravel-water pits are filled with water and gravel, which acts as the storage material. This artificial structure is buried in the ground and covered with a watertight plastic liner. Heat exchange occurs either by direct water exchange or by installed piping in different layers inside the store. Due to the gravel inside the storage system, no supporting structure, like for TTES and PTES, is necessary (Fig. 2.4b).

Hybrid storage systems consist of an underground concrete water pit combined with a field of borehole heat exchangers (Fig. 2.5). The water pit serves as short-term storage while the surrounding borehole field is used as long-term storage. The

concrete vessel is built without thermal insulation at bottom and side walls, because heat, which is transferred by conduction, is recovered from the borehole field. The top of the system, however, is insulated (Novo et al., 2010; Reuß et al., 2006; Reuß, 2003).

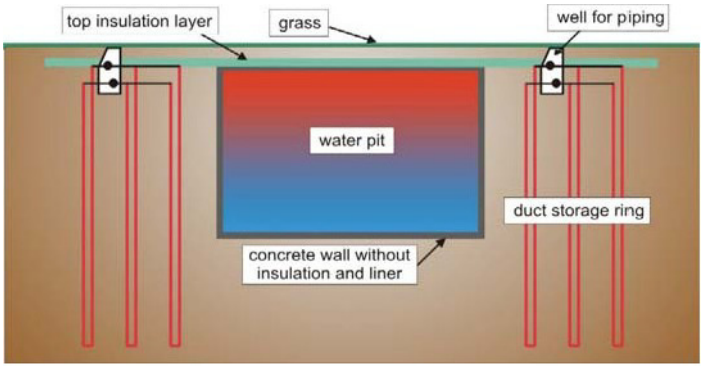

Fig. 2.5. Hybrid storage, a combination of water pit and borehole storage (fig. 2 of Reuß et al., 2006)

2.2 Numerical modeling of UTES systems

Practical problems of heat transfer by conduction and convection are often complex and cannot be solved by analytical methods. Nonlinear differential equations, complex geometries, complex boundary conditions and variable properties pose a problem that must be solved via numerical methods (Kreith et al., 2010). Numerical analyses use approximations that make governing equations solvable to a certain tolerance and can approximate real-world behavior with a high degree of accuracy (Dincer and Rosen, 2002).

There are some software programs that allow numerical analysis for UTES applications. Most of them use the finite element method (FEM), or the finite volume method (FVM). The Finite Difference method (FDM) may be used, however it is limited in terms of handling complex geometries. FLUENT^{TM}, for example, is an FVM commercial code that is able to simulate heat transfer and fluid flow in UTES (Dincer and Rosen, 2002).

Each numerical simulation starts with the discrete geometric representation of the system. Unstructured grids are referred to as "mesh". A mesh is the subdivision of a volumetric geometry into a group of non-overlapping smaller and simpler elements, like triangles, or tetrahedrons. The accuracy of the numerical simulation is highly

dependent on the detail captured by the geometrical model. Such models must be constructed bearing in mind sufficient simplicity to permit simulations with the available computing capabilities, while resolving higher amount of detail. With the latter being associated with higher computational expense, a balance must obtained between computational cost and detail (Dincer and Rosen, 2002). Typical commercial meshing applications are, Ansys Gambit, Ansys ICEM CFD, Triangle, GiD.

After the model is built and geometrically discretized, property modeling and configuration is needed. Initial and boundary conditions must be set, to close the system of equations posed by the discrete problem. If the energy equation is to be used (i.e. non-isothermal fluid flow), each cell must be assigned an initial temperature and pressure before computation of a transient solution begins.

Boundary conditions are needed in all domain boundaries. Normally, an inflow boundary condition goes together with a Dirichlet temperature setting. Outflow boundary conditions might also need such a condition, depending on the spatial discretisation. For those geometries that have boundaries representing walls, often a zero velocity (also termed no-slip) on the surface is established (Dincer and Rosen, 2002). Since, however, we are dealing with porous media, it is reasonable to assume a no-normal flow (or slip) boundary condition.

The simulation process involves the time-iterative sequence of the solution of the system of equations posed by the discrete version of the PDE's involved. Solution of the system, which varies depending on the strategy used, typically determines velocity, pressure, and temperature fields.

In addition to FLUENT^{TM} and the finite element code ANSYS (Ucar, Inalli, 2005), TRNSYS is a popular software to simulate energy storage systems. This simulation library is mainly used for vertically stratified storage systems. Amongst others (Sweet, McLeskey Jr., 2012; Terziotti et al., 2012; Urbaneck et al., 2002) use this software for numerical simulation of UTES.

3. Methodology

Fluid flow and heat transfer play a key role in geothermal storage systems. Numerical simulation is an application of physical theories that represent the underlying physical process in such an underground thermal energy storage. The conceptual model is what encompasses all of the ideas behind a simulation paradigm, and thus includes all of the theories and assumptions, equations, processes, algorithms, and even generated pseudo-code, which exists prior to programming a simulator. The idea and terminology behind the conceptual model was presented by Refsgaard and Henriksen (2004).

This chapter describes, in as much details as the scope allows, the theories, governing equations, and assumptions behind the conceptual model used to construct the simulator used in this thesis. It also presents a series of verifications and benchmark cases, and ends with the establishment of the model setup to be used for the main simulations presented in the following chapter.

3.1 Conceptual model of the storage system

With the intent of modeling fluid flow and heat transfer, the conceptual model used for this simulator is based on a series of assumptions imposed on well-known conservation laws. For a better understanding a brief overview of these physical processes and their mathematical modeling is given.

3.1.1 Fluid flow in porous media

Fluid flow involves the transport of mass of various chemical species and the transport of momentum. The equation of continuity can be derived from mass balance, and the well-known Navier Stokes equations can be derived from general momentum balance of a fluid particle. In a porous medium the equation of motion may be simplified and replaced by Dracy's law, which applies for low speed viscous flow. Combining these two laws, we can obtain one of the ruling equations for our prospective simulator (Ahmed, 2006; Bird et al., 2007).

Theories behind fluid flow in porous media are well established, with many advances and research being carried out in attempt to tackle the problem of simulating flow in

highly heterogeneous media. While Darcy's law provides significant simplifications for the governing equations in comparison to the Navier Stokes equations, underground media compensates this lack of difficulty with a provision of obstacles related to material interfaces and chemical interactions. While such interactions are beyond the scope of this thesis, it is important to mention that while flow in the underground is essentially of a very low Reynolds number, it is beset with other intricate issues which are not normally present in free flow. The mathematical description of the governing equations and assumptions used by my simulator is presented in section 3.3.1.

3.1.2 Thermal conduction and convection

Energy in the form of heat can be transferred by diffusion (conduction), advection (convection), and radiation. In my simulations I will only consider the first two processes. I neglect the possibility of heat transfer by radiation, which is heat transfer between two surfaces at different temperatures in the absence of a medium, because in heat-transport modeling it becomes significant only at temperatures greater than about 600°C (Incropera et al., 2007; Ingebritsen et al., 2006).

Conductive heat flux is given by Fourier's law of heat conduction. Mathematically, Fourier's law for the one-dimensional plane wall is expressed as (Fourier, 1829)

$$q_x'' = -\lambda \frac{dT}{dx} \tag{3.1}$$

where q_x'' [W/m^2] is the heat flow in the x direction, which is proportional to the temperature gradient dT/dx. The parameter λ is the thermal conductivity [W/m·K] and characterizes the effectiveness by which heat is transferred through a medium (Incropera et al., 2007). Fourier's law is analogous to Darcy's law. All these laws describe a linear relationship between a flux and the gradient of a potential (Ingebritsen, Sanford, 1998).

Convection within an isothermal fluid is the spatial translation of a property along the flow lines of a velocity field. In the presence of heat transfer, convection typically refers to that same macroscopic movement, which is caused by density changes due to temperature changes. Convection may therefore happen, for a single fluid, in one of two ways: free/natural, or forced.

In free (natural) convection the flow is induced by buoyancy forces in the fluid that arise from density differences. Brownian motion causes local thermal or density perturbations that will trigger a self organization process into convection cells (Bejan and Kraus, 2003; Dincer and Rosen, 2002). This type of convection may therefore only happen under the presence of gravity. Forced convection is induced by external forces, other than gravity (e.g. direct external cooling/heating of some portion of the domain through a pump or fan, much like in a convection oven). Generally the heat transfer by natural convection is much lower than for forced convection (Dincer and Rosen, 2002).

In porous media advection typically occurs together with diffusion. The Peclet number and the Raleigh number, two non-dimensional numbers (see Appendix), help to evaluate the diffusion - advection balance in a system.

These two heat transfer modes, together with the flow equations, yield to a coupled group of partial differential equations (eqn. (3.3), (3.5) and (3.14) below) in a non-isothermal system:

- The law of conservation of mass (continuity equation)
- Newton's second law of motion (momentum conservation equation)
- The first law of thermodynamics (energy conservation equation)

With the aim of simplifying the coupling effects which would otherwise incur further computational expense and algorithm complexity, the Boussinesq approximation can be applied.

3.2 Process inventory

This section describes the two basic simulation processes, which are necessary to simulate the real-world system. These are a thermal reservoir simulator and a corn drying control system (CDCS).

3.2.1 Thermal reservoir simulator

For modeling the physical behavior in the UTES a thermal reservoir simulator is required. This is essentially a numerical simulation stemming from the solution of a mathematical model that, due to practical reasons, may not be solved analytically.

Nonlinear differential equations, complex geometries, complex boundary conditions and variable properties must be assembled and discretized via numerical discretization methods (Kreith et al., 2010).

The numerical simulations presented in this work are carried out using the Complex Systems Modeling Platform (CSMP++), an object-oriented software framework written in C++. It is designed for the simulation of complex geologic processes in two or three spatial dimensions and their interaction over time. Finite-element (FE) and finite volume (FV) discretization methods are implemented in CSMP++. An important advantage of FE and FV methods in contrast to Finite Difference methods is the usage of unstructured meshes facilitate computations on complex geometries (Matthäi et al., 2001).

Hybrid finite element-finite volume discretization (Paluszny et al., 2007a) is used for solving heat transport in the geothermal storage facility. This combined method enables the calculation of the advective components of the advection-diffusion equation using the finite volume method and the diffusive components with the finite element method. Darcy's law is used to obtain the velocity field of the entire model and an equation of state (EOS) for pure water, which is based on the NBS/NRC Steam Tables (Haar et al., 1984) to calculate the fluid density, are required for a realistic numerical simulation.

For validating my simulator, I benchmark the results against results from the PHT simulator. This is a compressible flow simulator generated from CSMP libraries, which is computationally more expensive.

3.2.2 Corn drying control system

The simulator also assumes the role of the real word system for the optimization of the corn drying process. Thus a cyclic physical system, called corn drying control system (CDCS), is implemented into the simulator, which has the ultimate goal of optimizing the corn drying process. For a better understanding of this control system it is important to introduce the basic principles of the corn drying process.

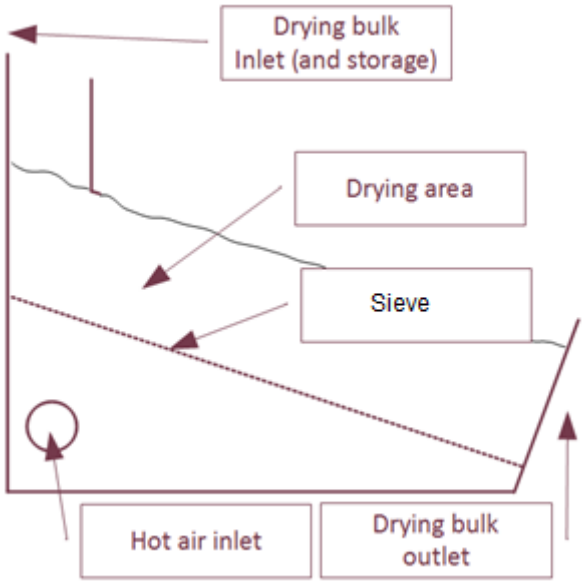

Fig. 3.1: Sketch of the corn drying facility

The corn drying facility consists of a container, into with the drying bulk is loaded batchwise. Ambient air is sucked in and heated by a heat exchanger with the waste heat of the combined heat and power unit (CHPU). The hot air flows through a mesh into the drying area and removes excess moisture from the corn (Fig. 3.1).

Hot water from the storage system can be used to add heat to the air through a second heat exchanger (Fig. 3.2a). This heated mass flow of air will increase the corn drying efficiency. Fig. 3.2b shows that the corn drying process relates on the capacity of air to hold water. A higher temperature of the airflow increases the capacity of air to contain water vapor. Corn drying capacity can thus be control via air temperature or air flow rate.

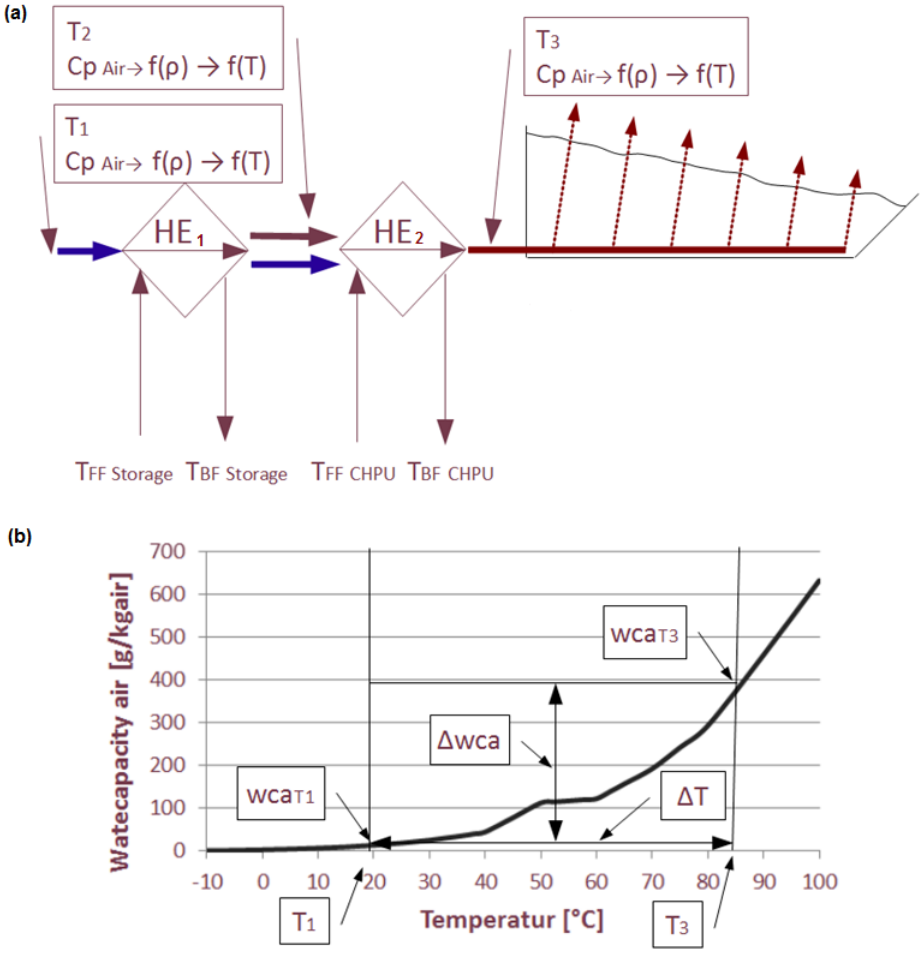

Fig. 3.2: Corn drying principle. a) The air flow with ambient temperature T_1 heats in heat exchanger 1 with the hot water from the storage $T_{FF,\ Storage}$ to T_2 and heats again in heat exchanger 2 with the waste heat from the CHPU $T_{FF,\ CHPU}$ to T_3. The mass air flow with temperature T_3 dehydrate the corn in the container. b) Water capacity of air versus temperature. A high air temperature represents a high water absorptive capacity of air.

After the corn drying process is known, I explain the role of the CDCS and how it is integrated into the geothermal simulator. The CDCS can be used to test different geometries and injector-producer configurations. With the aim of optimizing storage capabilities and deployment of the stored energy for corn drying, the simulator has to account for influences from daily and seasonal changes in atmospheric conditions. This is achieved through an internal control algorithm that reads output from the simulator such as production temperatures, and adjusts flow rates accordingly.

The CDCS forms a feedback loop implemented in the simulator. The internal control algorithm obtains the temperature at the production well(s) and calculates the injection temperature and injection rate, which are then input at the next time iteration (Fig. 3.3).

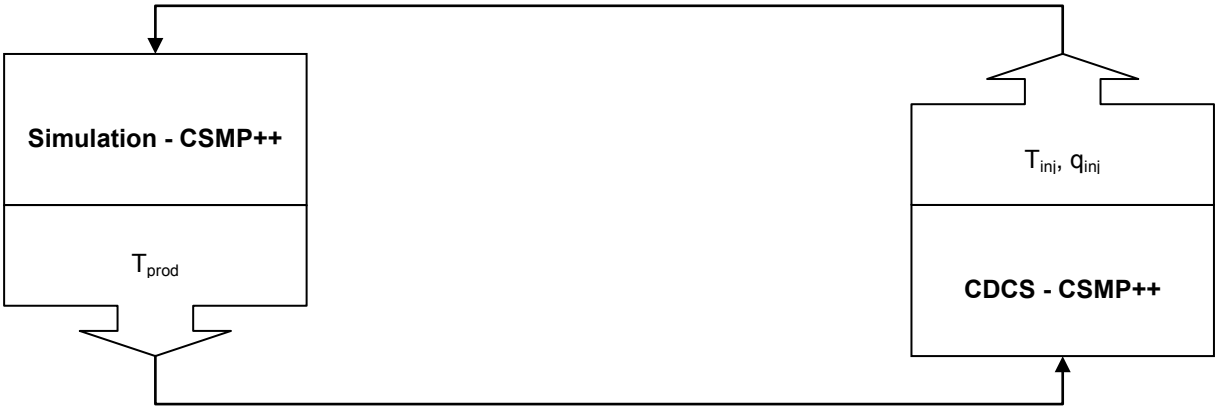

Fig. 3.3: Communication between the thermal simulator and the CDCS. The simulator receives the injection temperature and rate for the next time iteration and the CDCS obtains the temperature at the production well.

I have inserted command-line arguments into the code of the simulator to operate the simulator at the beginning of a charging or discharging simulation (Algorithm 2). Initially the simulator will ask the user to input the simulation time (i.e. time of charging or discharging period). It is possible then to also input a temperature value at the top boundary of the model, to account for seasonal changes of surface temperature. Next, the user has the option to start a simulation with or without the CDCS. For the first case the user chooses injection and production wells and has also the possibility to deactivate/reactivate a well completely. The internal control algorithm contains the input parameters for the corn drying calculations and performs the required calculations to obtain an optimal injection rate and temperature in the current configuration. The final output of the simulator is the delivered energy from the storage system. For the second case an injection/production rate, as well as an injection temperature for each well can be inserted. Following this input section the simulator calculates the evolution of pressure and temperature fields depending on the simulation time until the next control checkpoint. The simulator then outputs the temperature at the production wells to the screen. If the simulation is continued, the

described input process begins again, and the simulation continues with the new parameters.

3.3 Mathematical description of the conceptual model

As already mentioned there are three fundamental conservation laws that are relevant for fluid flow in geothermal systems in porous media (Darcy, 1856):

- The law of conservation of mass (continuity equation)
- Newton's second law of motion (momentum conservation equation)
- The first law of thermodynamics (energy conservation equation)

These three laws define partial differential equations, which therefore become governing equations.

3.3.1 Governing Equations

I first introduce the continuity equation and then the momentum balance equation. These two equations are the starting point for modeling isothermal flow of a pure fluid. Following this, I introduce the last energy conservation equation for non-isothermal fluid flow.

3.3.1.1 The Equation of Continuity

The continuity equation is a mass balance over a volume element$\Delta x\ \Delta y\ \Delta z$, through which a fluid is flowing:

$$\left\{\begin{matrix} rate\,of \\ increase \\ in\,mass \end{matrix}\right\} = \left\{\begin{matrix} rate\,of \\ mass \\ in \end{matrix}\right\} - \left\{\begin{matrix} rate\,of \\ mass \\ out \end{matrix}\right\} \tag{3.2}$$

It translates this physical statement into mathematical language. And as the size of the volume element approaches zero, the equation of continuity is arrived. This law describes the time rate of change of fluid density at a fixed point in space (i.e. in Eulerian coordinates) (Bird et al., 2007):

$$\frac{\partial \rho}{\partial t} + \nabla \cdot (\rho \mathbf{v}) = 0 \tag{3.3}$$

Here ρv is the mass flux and ∇·(ρv) is the divergence of the mass flux, which is the net rate of mass flux per unit volume.

3.3.1.2 The Equation of Conservation of Momentum

The equation of motion is developed by writing a momentum balance over a volume element Δx Δy Δz of the form

$$\left\{\begin{matrix}rate\,of\\increase\\of\ momentum\end{matrix}\right\}=\left\{\begin{matrix}rate\,of\\momentum\\in\end{matrix}\right\}-\left\{\begin{matrix}rate\,of\\momentum\\out\end{matrix}\right\}+\left\{\begin{matrix}external\\force\,on\\the\ fluid\end{matrix}\right\} \tag{3.4}$$

to obtain the equation of motion, also known as the Navier-Stokes equations (Bird et al., 2007):

$$\underbrace{\frac{\partial}{\partial t}\rho\mathbf{v}+\nabla\cdot\rho\mathbf{v}\mathbf{v}}_{Intertia\ \ forces}=\underbrace{-\nabla p}_{pressure\ forces}-\underbrace{\nabla\cdot\tau}_{viscous\ forces}+\underbrace{\rho g}_{body\ forces} \tag{3.5}$$

Here, v is the flow velocity, p is the pressure and τ is the component of the total stress tensor. If the flow is slow enough the inertia forces may be neglected. Assuming that the only external forces are gravitational forces, then the equation of motion can be simplified to the well-known Darcy's equation, which describes the flow of a Newtonian fluid through a porous medium (Darcy, 1856):

$$\mathbf{v}_D=\frac{k}{\mu}(-\nabla p+\rho\mathbf{g}) \tag{3.6}$$

Darcy's law states that the Darcy velocity v_D [m/s] of a homogeneous fluid in a porous medium is proportional to the pressure gradient ∇p [Pa/m] and inversely proportional to the fluid viscosity μ [Pa·s]. The proportionality constant k [m^2] is the permeability of the porous medium. The average flow velocity v in the pore space is calculated as (Darcy, 1856)

$$\mathbf{v}=\frac{\mathbf{v}_D}{\phi} \tag{3.7}$$

and is called interstitial or pore velocity.

3.3.1.3 The Equation of Conservation of Energy

The third fundamental law, necessary to describe fluid flow influenced by temperature and/or compressibility effects, is the law of conservation of energy. It states that the total energy in a closed system is not created or destroyed. When applied to any control volume (Hess, 1840), I have,

$$E_2 - E_1 = \Delta Q - \Delta W \tag{3.8}$$

where E_1 [J] and E_2 [J] are the initial and final values of the total energy in the control volume. ΔQ [J] is the change in heat content and ΔW [J] is the mechanical work performed inside the system. Introducing the enthalpy H and mass flux $\dot{m}$ the total rate of change in energy for a control volume is obtained. This balance is also known as the energy equation (Arpaci et al., 2000),

$$\underbrace{\frac{dE_{CV}}{dt}}_{Energy\ rate} = \underbrace{\sum_{i=1}^{N} \dot{m}_i H}_{Enthalpy\ flow} + \underbrace{\frac{\partial Q_{CV}}{\partial t}}_{Heat\ flux} + \underbrace{\frac{\partial W_{CV}}{\partial t}}_{Work\ rate} \tag{3.9}$$

where ∂Q is the received rate of net heat by the control volume and ∂W is the rate of net work done by the control volume (Arpaci et al., 2000; Kaviany, 2011).

Furthermore, I apply the first law of thermodynamics to flow through porous media while assuming that the medium is isotropic, viscous dissipation and the work performed by pressure changes is generally small and can be neglected. Additionally, when there is local thermal equilibrium between the fluid and the medium, the energy equation becomes (Bejan, Kraus, 2003),

$$\left(\rho c\right)_m \frac{\partial T}{\partial t} + \left(\rho c\right)_f \mathbf{v}_D \cdot \nabla T = \nabla \cdot \left(\lambda_m \nabla T\right) + q'''_m \tag{3.10}$$

where,

$$\left(\rho c\right)_m = (1-\phi)\left(\rho c\right)_s + \phi\left(\rho c_p\right)_f \tag{3.11}$$

$$\lambda_m = (1-\phi)\lambda_s + \phi\lambda_f \tag{3.12}$$

$$q'''_m = (1-\phi)q'''_s + \phi q'''_f \tag{3.13}$$

$(\rho c)_m$ is known as the overall heat capacity per unit volume, λ_m is the overall thermal conductivity and q''_m is the overall heat source per unit volume of the medium, respectively. Equation (3.10) may be also written as (Bejan, Kraus, 2003),

$$\sigma \frac{\partial T}{\partial t} + \mathbf{v} \cdot \nabla T = \nabla \cdot (\kappa_m \nabla T) + \frac{q'''_m}{(\rho c_p)_f} \tag{3.14}$$

where σ is the heat capacity ratio,

$$\sigma = \phi + (1+\phi)\frac{(\rho c)_s}{(\rho c_p)_f} \tag{3.15}$$

and κ_m is the thermal diffusivity of the fluid,

$$\kappa_m = \frac{\lambda_m}{(\rho c_p)_f} \tag{3.16}$$

3.3.2 Simplifying assumptions

The governing equations for convective flow are non-linear, and coupled. To simplify these equations I assume that

- The Boussinesq approximation is valid
- The flow is incompressible
- Density varies linearly with temperature in the buoyancy term

The Boussinesq approximation neglects the variation in density for a single fluid (effectively treating the flow as incompressible), and accounts for it only in the buoyancy term. This assumption is reasonable when the variation of density within the expected ranges of temperature is very small (Boussinesq, 1897) :

$$\frac{\Delta\rho}{\rho_{ref}} << 1 \tag{3.17}$$

Neglecting the density variation in the continuity equation (3.3), we obtain (Bejan and Kraus, 2003):

$$\nabla \cdot \mathbf{v} = 0 \tag{3.18}$$

This formulation holds true for an incompressible porous media.

The density difference for the thermal buoyancy is approximated as a pure temperature effect via (Boussinesq, 1897),

$$\rho \approx \rho_0[1 - \beta(T - T_0)] \tag{3.19}$$

in which β [1/K] is the thermal expansion coefficient,

$$\beta = -\frac{1}{\rho}\left(\frac{\partial \rho}{\partial T}\right)_p \tag{3.20}$$

and thus, the effect of pressure on the density is neglected.

The Boussinesq approximation is deemed valid if $\beta(T-T_0) \ll 1$, which translates to small density differences, where the variation of density is assumed linear and affecting only the buoyancy term. It should be noted that this also assumes that β remains essentially constant (Bejan and Kraus, 2003). These conditions apply for thermal energy storage heating and cooling applications and therefore are adopted in many case studies that take convection into consideration (Dincer, Rosen, 2002; Ievers and Lin, 2009; Rysanek, 2009; Urbaneck et al., 2002).

Substituting the Boussinesq approximation (3.19) into Darcy's law (3.6), the second governing equation can be written as (Nield and Barletta, 2010):

$$\frac{\mu}{k}\mathbf{v} = -\nabla p + \rho_0 \mathbf{g} - \rho_0 \mathbf{g}\beta(T - T_0) \tag{3.21}$$

Now we insert the simplified momentum equation (3.21) into the continuity equation (3.18) to obtain:

$$\nabla \cdot \left(\frac{k}{\mu}\left(-\nabla p + \rho_0 \mathbf{g} - \rho_0 \mathbf{g}\beta(T - T_0)\right)\right) = 0 \tag{3.22}$$

Equation (3.22) expresses the fluid mass conservation in the systems in terms of changes in fluid pressure and is often called pressure equation (e.g. Geiger et al., 2006a).

Canceling the heat production part of the energy equation (3.14), the third governing equation, also called the temperature advection-diffusion equation, is written as (Kawada et al., 2004)

$$\sigma \frac{\partial T}{\partial t} + \mathbf{v}_D \cdot \nabla T = \nabla \cdot (\kappa_m \nabla T) \tag{3.23}$$

It is assumed that the porosity, the heat capacities, the heat conductivities are constant and that there is an instantaneous local thermal equilibrium so that the

temperatures for the solid and fluid phases are the same (Bejan and Kraus, 2003; Kawada et al., 2004).

Due to the simplicity of the Boussinesq approximation, it is often used for numerical modeling and simulation of thermal energy storage systems (Dincer and Rosen, 2002; Urbaneck et al., 2002). It is also applied for studying hydrothermal circulation (Kawada et al., 2004) and buoyancy driven fluid flow in porous media, where thermal and chemical variations in the fluid cause density differences (Schoofs, 1999).

3.4 Discretization approach of the governing equations via Hybrid FE-FV method

The governing equations are non-linear and have mixed parabolic (diffusive) and hyperbolic (advective) character. The system of equations is solved within the framework of the object-oriented C++ code Complex System Modeling Platform (CSMP) (Matthäi et al., 2001). The numerical solution technique combines finite element and finite volume methodologies (Geiger et al., 2006a, 2006b). FE-FV combines the robustness of FVM in solving advection -dominated problems, with the capability of FEM to handle diffusion-dominated problems.

In the FE-FV method the pressure equation (3.22) is solved in sequence with the energy conservation equation (3.23). Assuming that the fluid and porous medium are incompressible, the resulting elliptic pressure diffusion equation is conveniently discretized using the FE method. An FV method is used to solve the advective part of the energy equation, while the FE method is used to account for the contribution of the diffusive terms. In the case of the transient energy equation, a fully implicit time discretization strategy is used.

The governing equations are decoupled through the operator-splitting technique described by Strang (1968), and is similar to the well-known implicit pressure, implicit saturation (IMPIMS) approach used in reservoir engineering applications, with the exception that temperature is transported in this case instead of saturation. In a first step the initial temperature field is calculated, then the fluid density calculated from the equation of state as a function of temperature (eqn. (3.17)) through the initial values. In the next step of the sequential procedure, the fluid pressure is calculated

through equation (3.22). Fluid velocities are obtained from Darcy's law (eqn. (3.21)). The advection and diffusion of the temperature field is then calculated via (3.23). The solution process is detailed further in Algorithm 1 (Coumou et al., 2006; Geiger et al., 2006a; Geiger and Emmanuel, 2010).

3.4.1 Numerical discretization of the pressure equation

Pressure equation (3.22) is discretized and ultimately solved via the FE method. The computational domain must thus be subdivided into non-intersecting elements. If I write the integral form of equation (3.22) and apply the method of weighted residuals I obtain,

$$-\int \nabla \cdot \left(\frac{k}{\mu} \nabla p - \rho_B \mathbf{g} \right) W dV = \int q W dV \tag{3.24}$$

where W are the arbitrary weight functions, ρ_B is the Boussinesq density (3.19) and *q* is the source term. After integrating by parts I reach the weak form of equation (3.24) to which I substitute the finite element shape functions N to get the Galerkin Weak form,

$$\sum_{j=1}^{N_{nodes}} \underbrace{\left[\int_{V_e} \nabla N_i^T \cdot \frac{k}{\mu} \cdot \nabla N_j dV \right] p_j}_{pressure\,term} = \underbrace{\int_{V_e} \nabla N_i \left(\frac{k}{\mu} \rho_B \mathbf{g} \right) dV}_{buoyancy\,term} + \underbrace{\int_{V_e} N_i q dV}_{source\,term} \tag{3.25}$$

where the sum represents an assembly of contributions from each element connected to a node. This finally yields a system of equations, one for each node. This system can be expressed algebraically via the matrix equation,

$$\mathbf{Kp} = \mathbf{f} \tag{3.26}$$

with

$$\begin{aligned} K_{ij} &= \int_{V_e} \nabla N_i^T \cdot \frac{k}{\mu} \cdot \nabla N_j dV \\ f_i &= \int_{V_e} \nabla N_i \left(\frac{k}{\mu} \rho_B \mathbf{g} \right) dV + \int_{V_e} N_i q dV \end{aligned} \tag{3.27}$$

where K is typically known as the stiffness matrix.

3.4.2 Numerical discretization of the temperature advection-diffusion equation

To solve the advection - diffusion equation (3.23) including sources the finite element mesh is then used to construct finite volume cells as shown in Fig. 3.4. For the finite volume formulation, integration on node-centered finite volume cells is required. Thus, advective and diffusive heat transfer are required at each “facet”. For calculating advective fluxes, the fluid velocity field is used which consists of the application of Darcy's law (3.6) via the gradient of the pressure FE solution. The diffusive fluxes are assembled in the same manner as they would in a FE discretization. Hence, temperature transport is discretized through the FV method, however diffusion effects are accounted for by replacing equivalent FE terms from elements connected to each individual FV.

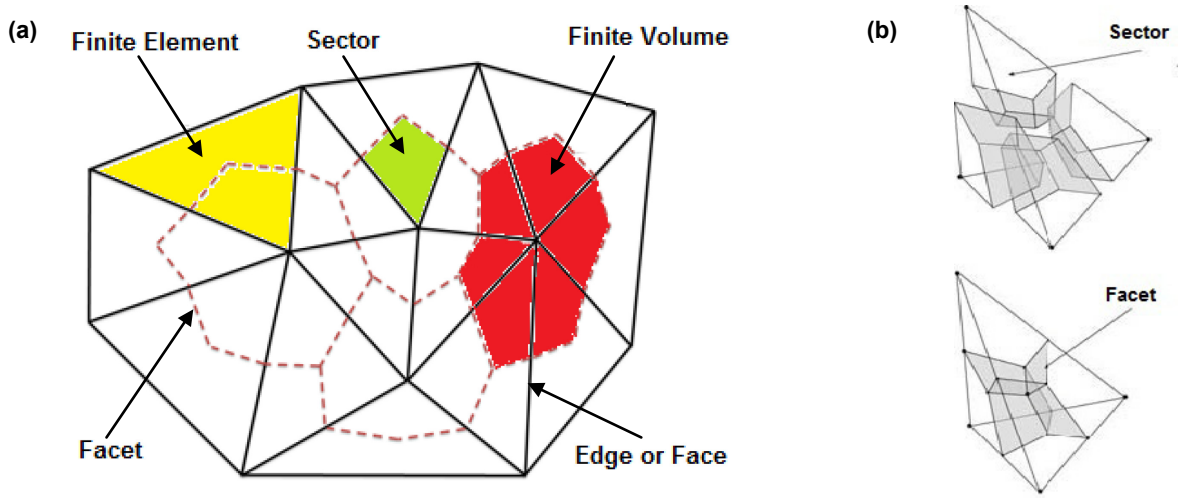

Fig. 3.4: Hybrid finite element finite volume grid (a) in 2D. Finite volumes are created around the FE nodes by connecting the midpoints of the element edges with the element's barycenter (Baliga and Patankar, 1980) . (b) Finite volume stencil for a tetrahedron element (fig. 8 of Paluszny et al., 2007b)

The integration over the finite volume V_i connected to node i of both advective parts and diffusive parts of equation (3.23) yields,

$$\underbrace{\int_{V_i} \sigma_i \frac{\partial T}{\partial t} dV_i}_{\text{Transient term}} = \underbrace{-\int_{V_i} \mathbf{v} \cdot \nabla T dV_i}_{\text{Advective term}} + \underbrace{\int_{V_i} \nabla \cdot (\kappa_m \nabla T) dV}_{\text{Diffusive term}} \tag{3.28}$$

Taking a closer look at sector i of the FV, which corresponds to node i the diffusive term becomes:

$$\int_{V_e} \nabla \cdot (\kappa_m \nabla T) N_i dV \tag{3.29}$$

Integration by parts yield to the Galerkin weak form,

$$\int_{V_e} \nabla N_i^T \cdot (\kappa_m \nabla T) dV = \sum_{j=1}^{N_n} \left[\int_{V_e} \nabla N_i^T \kappa_m \nabla N_j dV \right] T_j \tag{3.30}$$

where N_n is the number of nodes corresponding to this specific element e and V_e is the volume of the finite element e. The integral is solved by numerical integration using Gauss points:

$$\sum_{j=1}^{N_n} \left[\sum_{k=1}^{N_{gp}} \omega_k \left| \mathbf{J}^{(e)} \right| \cdot \left(\nabla N_i^e \right)^T (\zeta_k) \kappa_m \nabla N_j^e (\zeta_k) \right] T_j \tag{3.31}$$

Discretizing in time leads to the final solution $T^{t+\Delta t}$

$$\underbrace{\sigma \frac{T_i^{t+\Delta t} - T_i^t}{\Delta t} |V_i|}_{Transient\,term} = \underbrace{-\sum_{j=1}^{N_f} \left[A_j \mathbf{v}_j^t T_{j*}^{t+\Delta t} \right] \cdot \mathbf{n}_j}_{Advective\,term} + \underbrace{\sum_{e=1}^{N_{ce}} \sum_{j=1}^{N_n} \sum_{k=1}^{N_{gp}} \omega_k \left| \mathbf{J}^{(e)} \right| \cdot \left(\nabla N_i^e \right)^T (\zeta_k) \kappa_m \nabla N_j^e (\zeta_k) T_j^{t+\Delta t}}_{Diffusive\,term} \tag{3.32}$$

where A_j is the surface area of the FV element facet j , V_i is the volume of the control volume i, n_j is the outward normal of facet j, N_f is the total number of facets belonging to the finite volume, N_{ce} is the number of parent elements, which are connected to node i, N_n is the total number of nodes of element e, N_{gp} is the local number of integration points for each element connected to node *i* (i.e. control volume *i*), ω_k is the weight coefficient, J is the determinant of the Jacobian matrix, ξ_k is the integration point and j* means that the value of T is taken from the upwind finite volume at segment j.

Once the matrices, which arise from equations (3.25) and (3.32), have been assembled, CSMP employs the algebraic multigrid solver SAMG (Stüben, 2002) to solve the algebraic linear system of equations that arises from the finite element and finite volume discretizations (Geiger et al., 2006a).

3.5 Verification and benchmark cases

The simulator is verified by comparing the numerical solution with analytical ones as well as benchmarking it against TOUGH simulator and the PHT simulator. Comparison cases are conducted by excluding and including gravity.

3.5.1 Comparison cases excluding gravity effects

A verification of the modeling methodology has been made via a comparison with an analytical solution as well as benchmarks with other simulators. In the first instance, results are compared for one-dimension advection-diffusion only case in the absence of gravitational force. Advection and diffusion of temperature at different Péclet numbers is calculated under the influence of flow of an incompressible fluid.

The advection-diffusion equation has the analytical solution (Ogata and Banks, 1961)

$$T(x,t) = \frac{T_{x=0}}{2} erfc\left[\frac{x - \mathbf{v}_x t}{2\sqrt{\kappa t}}\right] + \frac{T_{x=0}}{2}\exp\left[\frac{\mathbf{v}_x x}{\kappa}\right] erfc\left[\frac{x + \mathbf{v}_x t}{2\sqrt{\kappa t}}\right] \tag{3.33}$$

where erfc is the complementary error function. There is a good agreement between the numerical and analytical solutions (Fig. 3.5).

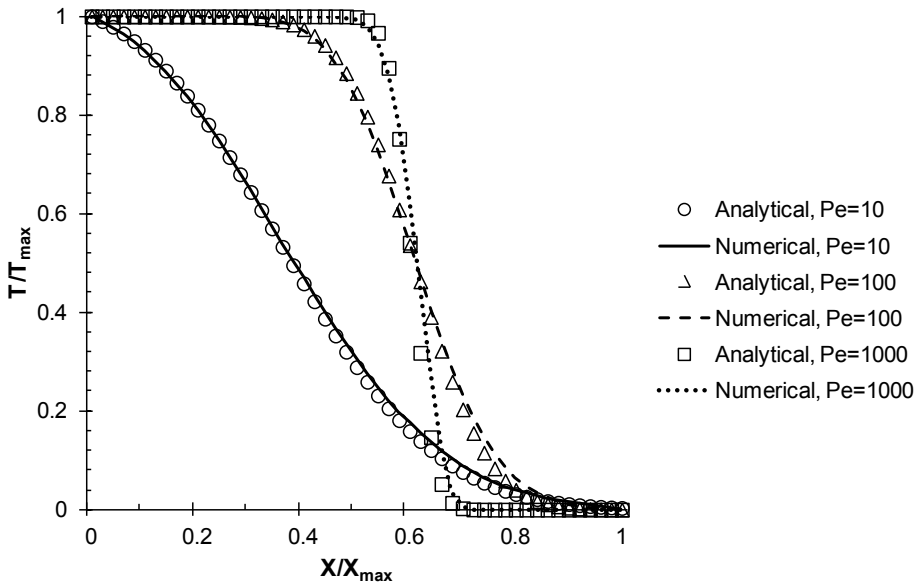

Fig. 3.5. Comparison between the analytical (open symbols) and the numerical (lines) solution for the advection - diffusion equation for heat transport by incompressible fluid at different Péclet numbers. The transport includes diffusion dominated flow at Pe=10 (circle and solid lines), an intermediate case at Pe=100 (triangles and dashed lines), and advection dominated flow at Pe=1000 (squares and dotted lines). The space-step Δx is 0.1m, the normalized grid resolution $\Delta x/\Delta x_{max}$ is 0.02.

To further verify that my simulator represents the advection - diffusion processes properly, I benchmarked it against the results obtained from TOUGH ("Transport of Unsaturated Groundwater and Heat") simulator and PHT ("Pressure Enthalpy Temperature") simulator. In this benchmark test case, gravitational forces are also neglected. The simulation model is a cross-sectional 2000 x 1000 m vertical square. The initial temperature is set to 50°C and the initial pressure is set to 1 atm. The parameters and the boundary conditions are shown in Table 3.1.

Table 3.1: Rock and fluid parameters and boundary conditions (BC) for advection-diffusion benchmark test case without gravity. All these parameters are constant, except of fluid density.

Parameter	Symbol	Unit	Value
Porosity	Φ	fraction	0.3
Permeability	k	m^2	1e-13
Rock density	ρ_r	kg/m^3	2650
Heat capacity of rock	c_r	J/kgK	1000
Total thermal conductivity	λ	W/mK	2
Fluid density	ρ_f	kg/m^3	988
Fluid viscosity	μ	Pa·s	0.000547
Fluid heat capacity	c_f	J/kgK	4181
fluid pressure (Dirichlet BC Left)	p_f	atm	2
fluid pressure (Dirichlet BC Right)	p_f	atm	1
temperature (Dirichlet BC Left)	T	°C	80
temperature (Dirichlet BC Right)	T	°C	50

The results (Fig. 3.6) show a good agreement with the other two simulators. This benchmark test provides initial proof that the geothermal simulator I present is able to simulate advection and diffusion of a scalar in the absence of gravity, correctly.

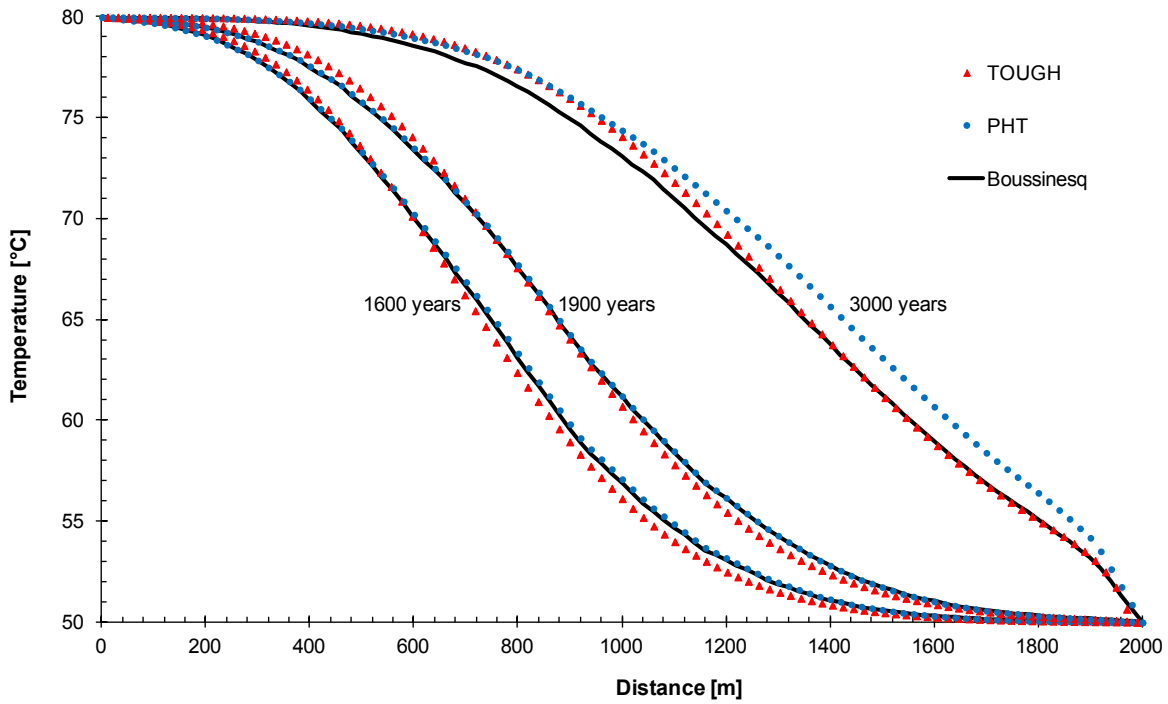

Fig. 3.6: Comparison between TOUGH (red triangles), CSMP_PHT (blue circles) and CSMP_Boussinesq (black line) results at different times for advection - diffusion benchmark test case without gravity. A time-step Δt of 1 year was chosen.

3.5.2 Comparison cases including gravity effects

To finally verify that my simulator represents the advection - diffusion processes under the influence of gravity properly, I benchmarked it against the results obtained from the PHT ("Pressure Enthalpy Temperature") simulator. In this benchmark fluid flow is gravity dominated. The simulation model is a simplified version of the final storage system shown in Fig. 3.10. The model contains a gravel region, surrounded by a box, with the rock properties of the loess region. The rock and fluid properties are shown in Table 3.2 and boundary conditions are shown in Table 3.3.

Table 3.2: Fluid parameters at 45°C, material properties for gravel (left) and loess (right) region for gravity-driven benchmark test case.

Parameter	Symbol	Unit	Value
Fluid density	ρ_f	kg/m^3	990.22
Fluid viscosity	μ	Pa·s	0.000596
Thermal expansion coefficient	β	1/K	0.00041974
Porosity	Φ	-	0.43/0.5
Permeability	k	m^2	$1.2^{-11}/1.2^{-15}$
Total specific heat capacity	c	J/kgK	2150/1500
Total thermal conductivity	λ	W/mK	2.6/1.54
Density (grain)	ρ_r	kg/m^3	2650/2740

Table 3.3: Boundary conditions for gravity-driven benchmark test case.

Essential conditions	Type	Parameter	Location	Value
Boundary condition	Dirichlet	fluid pressure	Top	101325 Pa
Region condition	Dirchlet	temperature	Groundwater region	12 °C
Region condition		Injector absolute rate	Injection well 1	0.0016 m^3/s
Region condition		Producer absolute rate	Production well 3	-0.0016 m^3/s
Initial condition		fluid pressure	Global	101325 Pa
Initial condition		temperature	Global	12 °C

For the analyses of the results (Fig. 3.7 and Fig. 3.8) only those nodes are selected across which heat transfer occurs. Fig. 3.7 shows the infinity norm of the temperature difference and the average of the absolute error between the CSMP_PHT and the CSMP_Boussinesq simulator. The infinity norm is the maximum temperature difference at a certain node in the domain. This is quite big in the beginning, however decreases after 4 days below 10°C. The average of the absolute error in the domain where heat transfer occurs shows a similar behavior as the infinity norm. After 7 days of simulation this error is slightly above 2°C and stays constant. Fig. 3.8 shows the frequency for different absolute error ranges. Absolute errors above 8°C are very seldom and more than 50% are below 2°C. This graph also shows that approximately 90% of the nodes in the considered domain have an absolute error below 4°C.

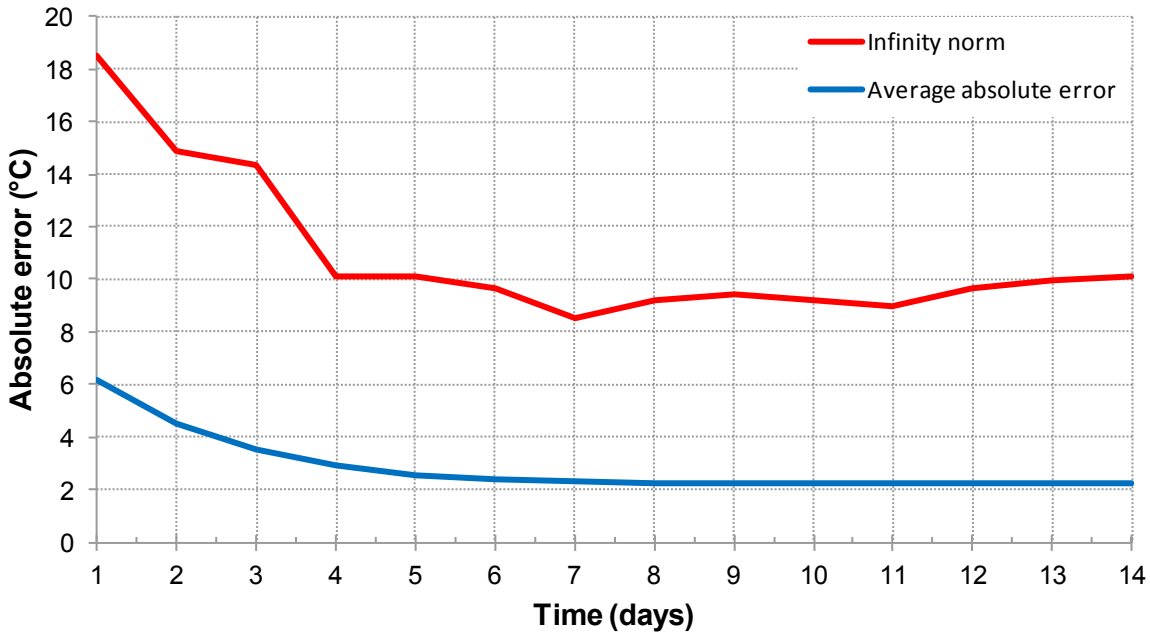

Fig. 3.7: Comparison via the L∞-norm (red lines) and the average of the absolute error for temperature difference between CSMP_PHT and CSMP_Boussinesq simulator. Only nodes are considered, where heat transfer occurs. After 6 days the average of the absolute error is approximately 2 and the infinity norm is 10. The simulation time is 2 weeks and a time-step Δt of 1 year was chosen.

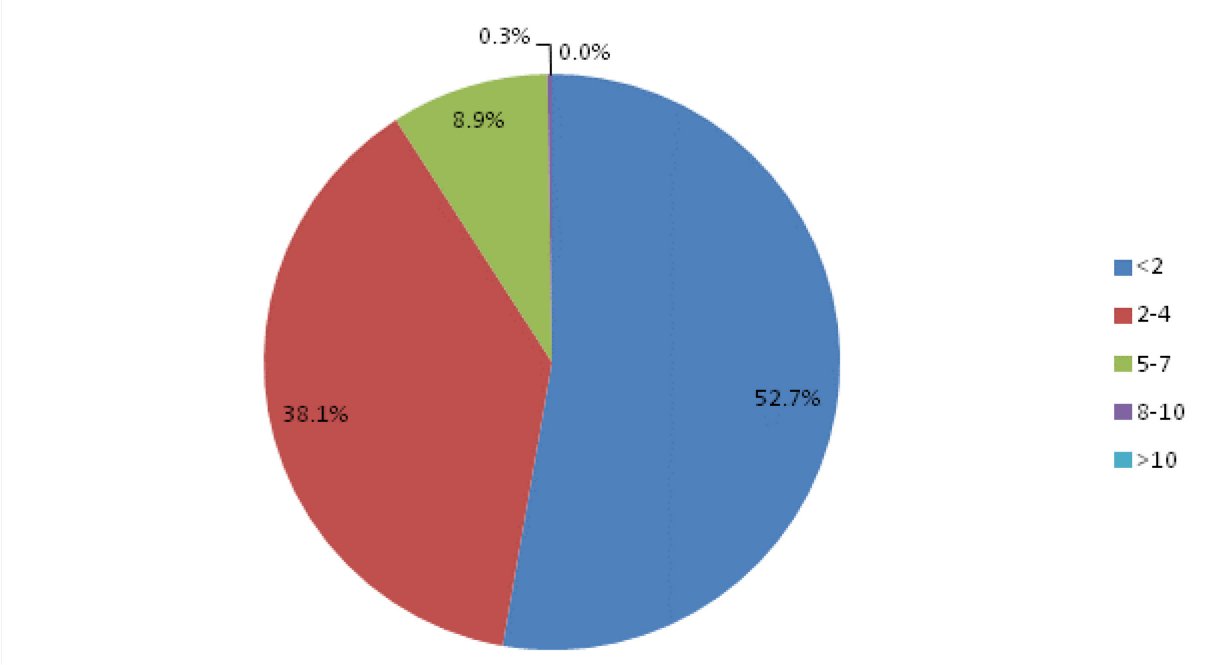

Fig. 3.8: Frequency plot of absolute error ranges after 10 days. 52.7% of all considered nodes in the domain have an absolute error below 2°C. 38.1% of the nodes have an absolute error between 2 and 4°C and just 8.9% of them have an error between 5 and 7°C. Only 0.3% of the nodes have an absolute error above 8°C

This benchmark test provides final proof that the geothermal simulator I present is able to simulate advection and diffusion of a scalar under the influence of gravity, correctly.

3.6 Pseudo codes

This section shows the pseudo codes for the solution process to model fluid flow and heat transfer (Algorithm 1) and for the communication between the simulator and the CDCS (Algorithm 2).

Algorithm 1: Pseudo code for the sequential solution process to model fluid flow and heat transfer

The weighted heat capacity (3.11) , the weighted thermal conductivity (3.12) and the initial thermal equilibration are calculated.

loop (model time)

Computation of Boussinesq gravity term and single phase mobility.

loop (nodes)
Calculation of Boussinesq density (3.19) at each node.
end loop
loop (elements)
Calculation of factor $\boldsymbol{K = \frac{\rho k}{\mu}}$
Multiplying K with gravitational constant g and calculate gravity term depending on element dimension.
end loop

Solve the incompressible single phase pressure diffusion equation (3.22), which includes the Boussinesq term, for pressure using standard finite elements to obtain a pressure field.

Computation of Darcy velocity including gravity effects

loop (elements)
Calculation of pressure gradient from pressure field and multiplying it with the mobility to get the Darcy velocity, $\boldsymbol{v = \nabla p \cdot \frac{k}{\mu}}$
Multiplying with gravity term to get velocity
end loop

Computation of heat transfer velocity

loop (elements)
Calculation of heat transfer velocity, $\boldsymbol{v_h = v \cdot \rho_f \cdot c_f}$
if
heat transfer velocity is divided through density and heat capacity of rock, $\boldsymbol{v_h = v \cdot \frac{\rho_f \cdot c_f}{\rho_r \cdot c_r}}$
end if
end loop

Solve the FE-FV advection - diffusion equation (3.23) for temperature using the computed heat transfer velocity.

end loop

Algorithm 2: Pseudo code for the communication with the CDCS and the user

while (*Finish* = *true*)
call function to change the injection and production rate and the temperature for a specific well

Defines the maximum number of wells

Input: Simulation time in hours (= time iteration)
Input: (Initial) temperature at the top boundary

loop *(number of wells)*
Show list of possible wells
end loop

Question1: Do you want to use the automatization? (y/n)
if "y" the user can choose injection/production wells and get to question 5. Then the simulation will run with the internal control algorithm. Finally it outputs the delivered energy from the storage system.

if "n" the user gets to question 2

Question2: Do you want to change the injection rate? (y/n)
if "y" there will be set a fluid volume source for the chosen injection well region
switch *(Injection rate)*
case "y"
Choose the appropriate well or continue
while *(Stop)*
if *(well number ≥ 1 or ≤ number of max. wells)*
Input fluid volume source for injection well(s)
else
continue
end while
break switch

Question 3: Do you want to change the production rate? (y/n)
if "y" a fluid volume source will be set for the chosen production well. The procedure is analogous
to question 1.

Question 4: Do you want to change the injection temperature? (y/n)
if "y" an injection temperature will be set for the chosen injection well. The procedure is then analogous to question 1.

Question 5: Do you want to deactivate some well? (y/n)
if "y" the property status of some will be changed from DIRICH to PLAIN and the fluid volume source will be set to zero.

call function to set a Dirichlet BC at the Top boundary
This function sets a Dirichlet BC for temperature (specific input value) at the Top boundary of the model

loop *(model time)*
solve for pressure and temperature
end loop

call function to output the temperature at the production well(s) to the screen

end while

3.7 Model setup

This section describes the geometry and design of the storage system and the geometric discretization of the model. Furthermore, rock properties, fluid properties, boundary conditions, and initial conditions for the numerical simulation are presented.

3.7.1 Geology of the projected test site

The storage system is located in the Molasse basin near St. Georgen bei Obernberg am Inn in Upper Austria. The typical near-surface stratigraphy in this region is shown in Fig. 3.9. First there is a small impermeable clay layer, then a Quaternary high permeable gravel layer and finally an impermeable pelitic deposition. The groundwater level is approximately 10 m below the ground level and its minimum inclination is 3‰ (up to 13‰). Hence, groundwater flow occurs in the lower part of the gravel layer with a Darcy flow velocity of about 10^{-6} m/s (FFG, 2011).

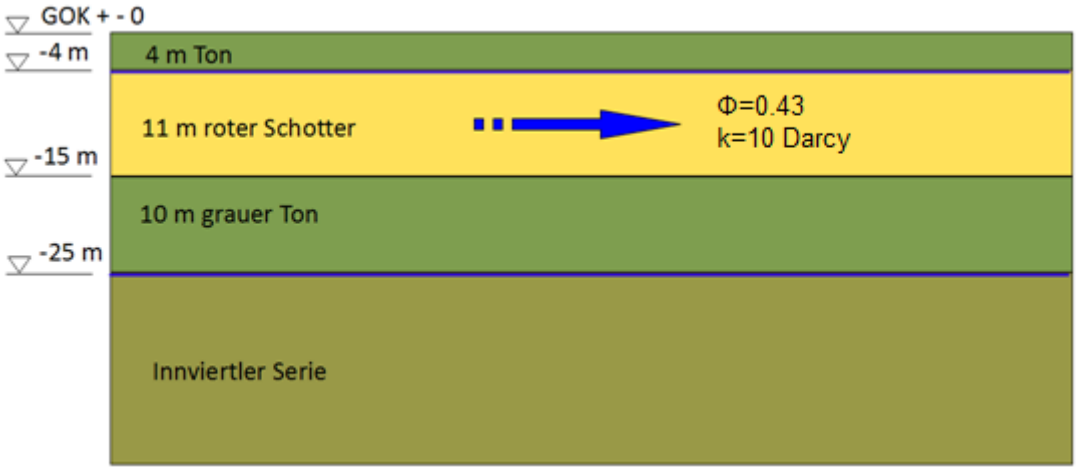

Fig. 3.9: Cross section through the expected site near - surface geology. The blue arrow indicates the groundwater flow in the yellow region (11m roter Schotter/gravel). The storage system is placed in this region and the two green regions above (Ton/clay) and below (grauer Ton/clay) border it, acting as insulators (fig. 27 of FFG, 2011).

This geology allows the usage of the natural underground as a geothermal storage system. The radial cross-sectional description of the storage system is shown in Fig. 3.10. The upper clayey and silty loess layer is impermeable and therefore serves as insulating top zone. The bottom of the storage system is the impermeable clay

marl layer, which also acts as insulator. The actual storage, where the water is injected and produced, is located in the intermediate gravel zone. This saturated gravel has a very high permeability and porosity (Müller and Schön, 2012). Due to the high flow velocity of the groundwater two vertical artificial walls are to be created by jet grouting, thus forming a confined cylindrical region. The impermeable walls consist of a clay/gravel mixture and help reduce advective heat losses to the surroundings.

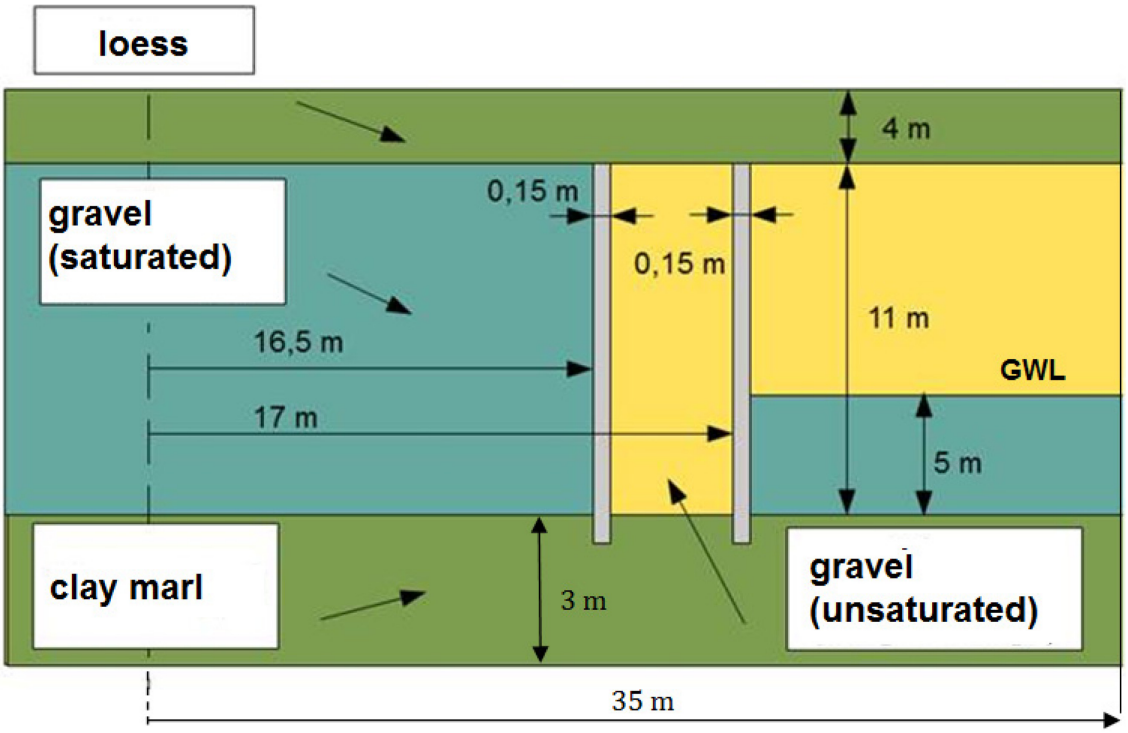

Fig. 3.10. Geometric and material description of the radial cross section of the storage system. The saturated gravel region (blue) on the left hand side is the actual storage, where water is injected and produced. The loess and clay marl region (green) and the two artificial walls (grey) boarder the storage and act as insulator. The unsaturated gravel region (yellow) exists between the artificial walls and outside the storage system above the groundwater level (GWL). Between the walls the groundwater is exhausted to reduce the heat loss from the storage system, consequently, just conduction and no convection occurs there.

3.7.2 Geometry and geometric discretization

The storage system has a cylindrical form with a diameter of 33m, a height of 11m and a porosity of 0.43. The resulting pore volume is 4050 m^3. I made a model of the storage geometry with the commercial software Rhinoceros 4.0. The exact dimensions of the storage system, and the extent and position of the wells can be observed in Fig. 3.11.

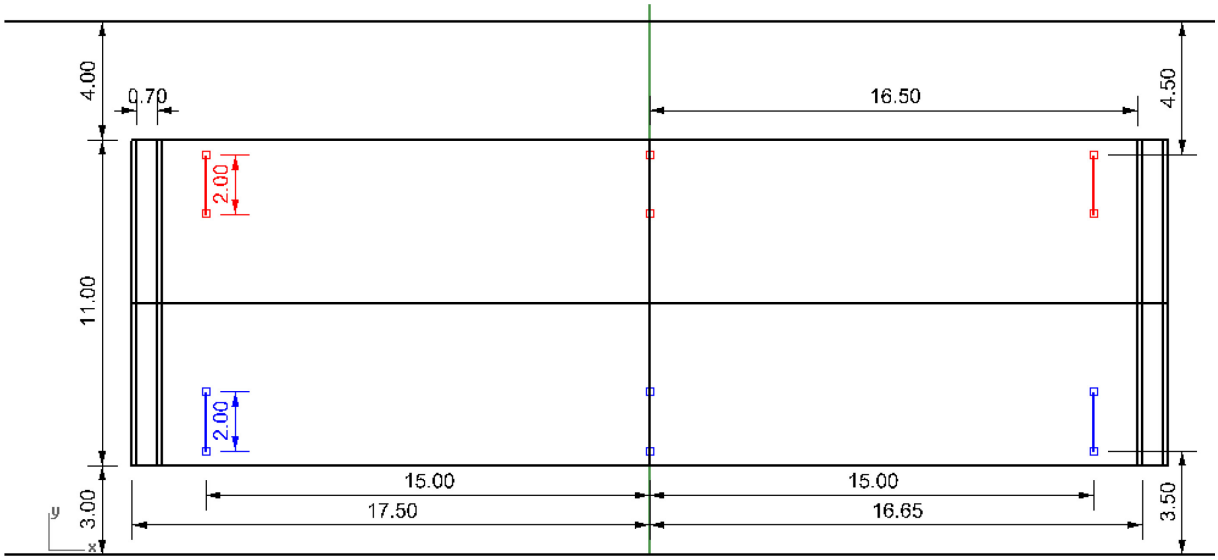

Fig. 3.11: Vertical middle plane cross section showing the dimensions in meters of the storage system. The blue lines represent the injection wells and the red ones the production wells. They are offset by 90° and defined by straight paths.

I discretize the three-dimensional domain using the meshing application ANSYS ICEM CFD to construct an unstructured grid. (Unstructured grids allow for easier resolution of complex geometries, as would be needed otherwise by structured grids). The meshing program subdivides the geometry into tetrahedral elements and surfaces with triangular ones. Unstructured meshes allow for an easier concentration of resolution at important places such as in the vicinity of wells or at small and thin structures within the geometry. I choose to locate finer elements near the wells, and above the saturated gravel region, because the latter region is particularly important since a Dirichlet temperature is set at the top boundary. The wells are represented by a collection of line elements, which are also generated by the tetra mesher.

The figures below show some vertical and horizontal cross sections of the storage system. A full domain vertical cross section can be observed in Fig. 3.12, where the locations of 4 out of 9 wells are also depicted. The other 4 wells are offset by 90° and therefore in the middle of the x-plane cross section. Producer well 9 is in the center of the gravel region near to the loess region. Fig. 3.13 shows a full domain horizontal cross section and Fig. 3.14 shows a zoom in of a vertical cross section near the bottom of the storage walls.

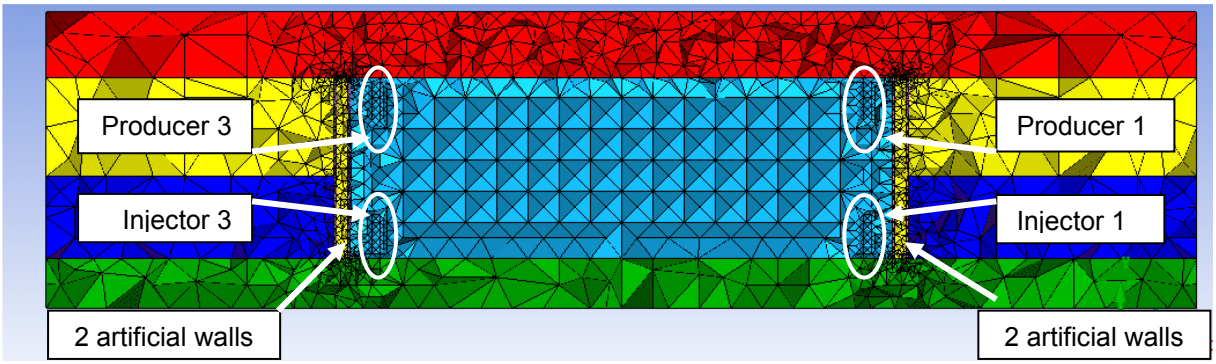

Fig. 3.12: Vertical cross section of the storage and its surrounding after the meshing process middle z-plane mesh. The colors represent the different regions in the system, saturated gravel/actual storage (light blue), clay marl (green), loess (red), groundwater region (dark blue) and unsaturated gravel (yellow). A finer mesh has been generated near the wells and above the storage in the loess region, because of temperature changes during the simulation at the top boundary of the domain. Fluid flow occurs in the saturated gravel region and in the groundwater region.

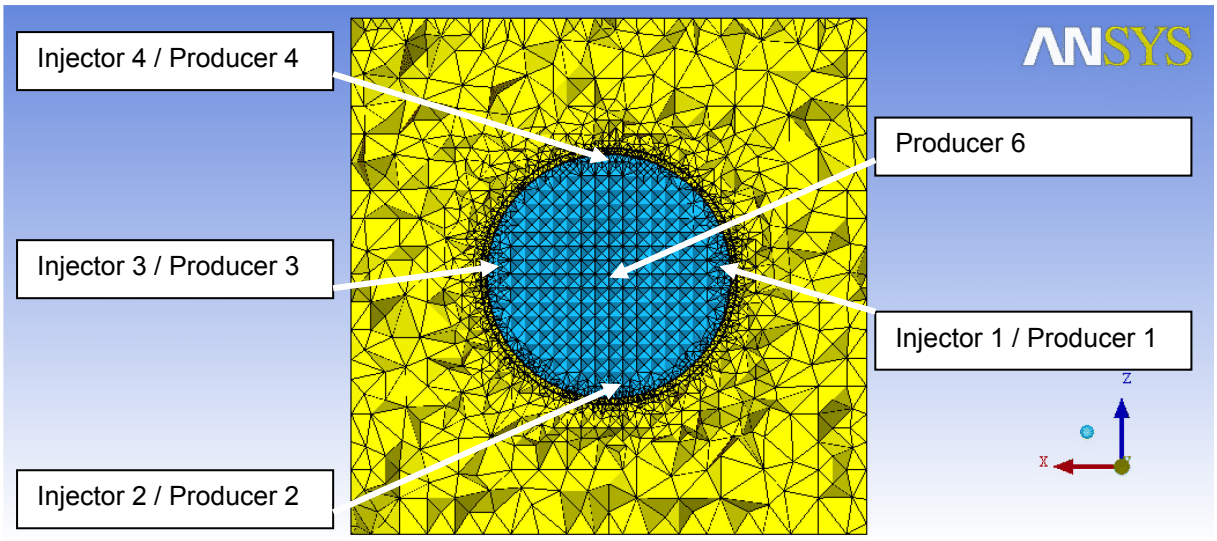

Fig. 3.13: Horizontal middle y-plane mesh cross section of the storage system. A finer mesh is generated near the two artificial walls, which are the boarder of the saturated gravel region (light blue) and the unsaturated gravel region (yellow). The positions of the wells are at the outer region of the storage and one production well (Producer 6) is in the center (light blue). The 4 injectors are near the bottom of the storage zone and the 4 producers are near the top of the storage zone. One injector and producer pair (e.g. Injector 1 and Producer 1) have the same x- and z- coordinates. The actual storage (light blue) is inside a box shape model with 70m x 70m x 18m extension, which allows to set appropriate boundary conditions for groundwater flow (Table 3.6). The groundwater region is below the unsaturated gravel region (yellow) (Fig. 3.12).

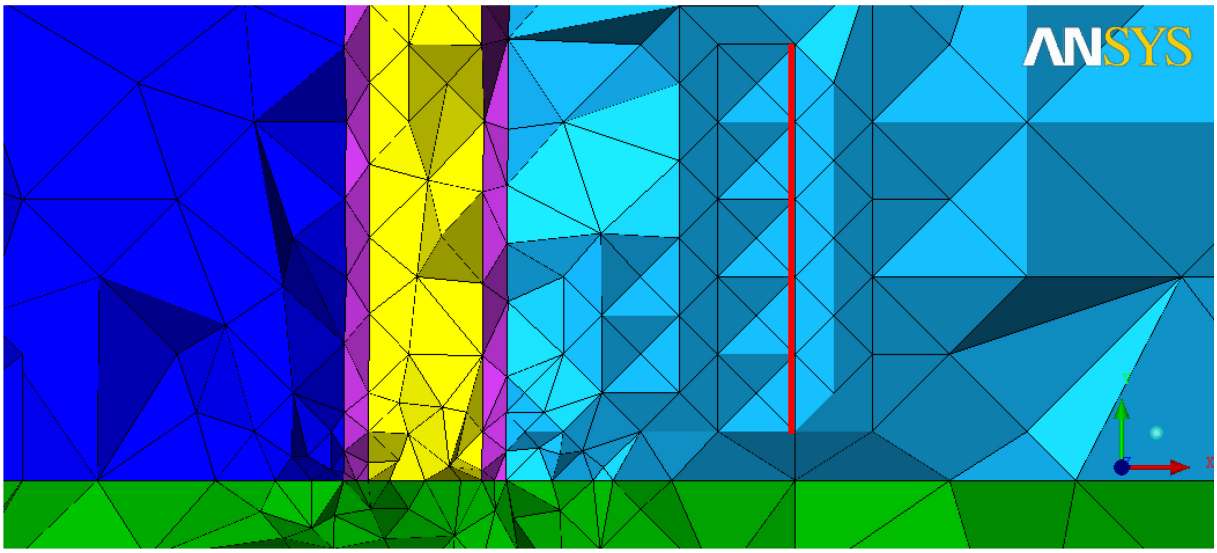

Fig. 3.14: Zoomed in vertical cross section view of the material interfaces between gravel, wall and clay marl. The position of injection well 3 is represented by a red line.

3.7.3 Model properties and essential conditions

The material and fluid properties used for the simulations without the control system (Run 1 -6) are summarized in Table 3.4 and Table 3.5, respectively.

Table 3.4: Material properties for the loess, gravel, wall and clay marl region of the modeled domain. Specific heat capacity and thermal conductivity refer to water saturated properties.

Material Region	Loess	Gravel	Wall	Clay marl
Porosity Φ [-]	0.5	0.43	0.5	0.5
Permeability k [m^2]	1.2e-15	1.2e-11	1.e-15	1.2e-15
Specific heat capacity c [J/kg·K]	1500	2150	1500	1500
Thermal conductivity λ [W/m·K]	1.54	2.6	1.5	1.56
Density (grain) ρ_r [kg/m^3]	2740	2650	2710	2770

Table 3.5: Fluid properties for water at 40°C. Density and thermal expansion coefficient refer to a water temperature of 20°C. All these parameters, except of the fluid density are constant.

Parameter	Symbol	Unit	Value
Fluid density	ρ_f	kg/m^3	998.2
Specific heat capacity	c_f	J/kgK	4182
Thermal conductivity	λ_f	W/mK	0.63
Fluid viscosity	μ	Pa·s	0.000653
Thermal expansion coefficient	β	1/K	0.000207

The essential conditions used for the simulations without the CDCS (Run 1 - 6) are summarized in Table 3.6. I calculated the boundary conditions for the groundwater flow with the help of a groundwater map, which shows the decline of the groundwater level over a certain distance. With that information I have calculated the hydrostatic pressure at the front -and backside of the simulation model. This relative pressure difference in the groundwater region, about 5.5 kPa, allows fluid flow from back to front and is set as Dirichlet boundary condition.

The groundwater flow is calculated separately and once only within the CSMP library. The FEM is used to calculate relative fluid pressure and groundwater flow in the groundwater region. The Darcy velocities resulting from these relative fluid pressure gradients are assumed constant over time and added each time step to the resulting full model velocity field. This final velocity field is used for the transport of

temperature. Furthermore, it is assumed that the groundwater velocity doesn't penetrate into the storage system, but flows around the storage walls.

Table 3.6: Essential conditions for Run 1 - 6. The boundary conditions are valid for all runs.

Essential conditions	Type	Parameter	Location	Value
Boundary condition	Dirichlet	fluid pressure	Top	101325 Pa
Boundary condition	Dirchlet	groundwater relative fluid pressure	Back	5483.71 Pa
Boundary condition	Dirchlet	groundwater relative fluid pressure	Front	0 Pa
Boundary condition	Dirchlet	temperature	Back	12°C
Region condition	Dirchlet	temperature	Injection well(s)	90/75/60 °C
Initial condition		fluid pressure	Global	101325 Pa
Initial condition		temperature	Global	12/90°C

3.7.4 Model setup for the simulations with the CDCS

The material properties used for the simulations with the CDCS (Run 1 – 6, see section 4) are the same as for the simulations without it and summarized in Table 3.4. The fluid properties are summarized in Table 3.7. The essential conditions are very similar to Table 3.6, except for the temperature at the injection well, which varies during the discharging period.

Table 3.7: Fluid properties for water at 55°C

Parameter	Symbol	Unit	Value
Fluid density	ρ_f	kg/m^3	985.65
Specific heat capacity	c_f	J/kgK	4183
Thermal conductivity	λ_f	W/mK	0.63
Fluid viscosity	μ	Pa·s	0.000504
Thermal expansion coefficient	β	1/K	0.00048553

In addition to the injection temperature, the injection/production rate and the temperature at the top of the domain vary during the discharging period. These

parameters depend on the outside temperature (i.e. the top boundary simulates external air temperature conditions), the temperature at the production well(s) and the injection well(s) and the operation mode.

There are three main operation modes for discharging. In each mode the storage system delivers a certain amount of power to the corn drying process. The amount of power depends on the preheating air stream temperature, which is the air temperature T2 after passing heat exchanger 1 (Fig. 3.2a). Adding the temperature difference in the heat exchanger to the preheating air stream temperature, the minimum required storage temperature is obtained. As long as the storage system can deliver this temperature, in this case 52°C, operation mode 1 is active. If the temperature decreases below this value, operation mode 2 becomes active (see Table 3.8). This process is also represented graphically in Fig. 3.15.

The corn drying season typically starts early in September and takes 1.5 - 2 months. During that time the average outside temperature decreases linearly from 11.8°C to 1.8°C, regarding notations from the Zentralanstalt für Meteorologie und Geodynamik (ZAMG). Each day the actual outside temperature is set as a Dirichlet boundary condition at the top of the model domain. This temperature also influences the temperature at the injection well.

Table 3.8: Three operation modes for discharging. Operation mode 1 and 2 are valid for all five runs. The values in brackets of operation mode 3 are valid for Run 4.

Parameter	Unit	Operation mode 1	Operation mode 2	Operation mode 3
Preheating air stream temperature	°C	42	34	20 (25)
Storage power/day	kW	312.7	209.6	88 (127.3)
∆T Heat exchanger	°C	10	6.4	2.7 (3.9)
Minimum required storage temperature	°C	52	40.4	22.7 (28.9)

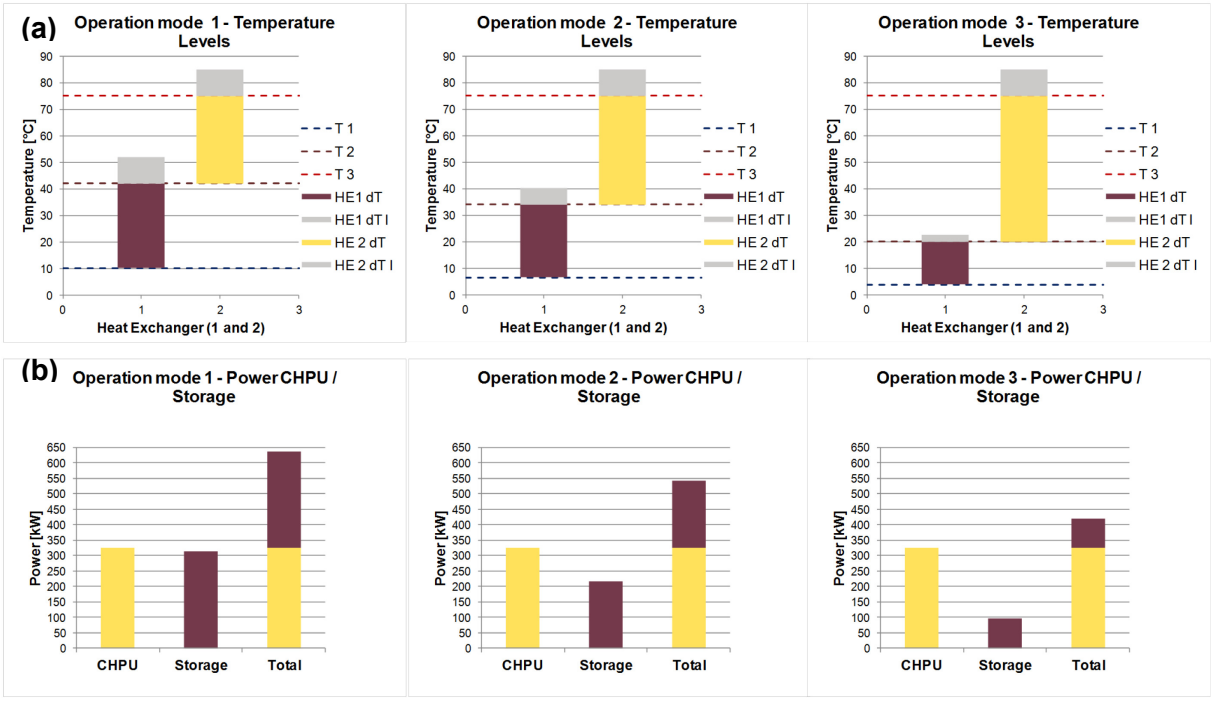

Fig. 3.15: Graphical description of the three operation modes for discharging. a) Temperature levels of the air stream at heat exchanger 1 (hot water from storage) and heat exchanger 2 (hot water from CHPU). For operation mode 1, air stream enters heat exchanger 1 with 10°C and enters heat exchanger 2 with 42°C. Air is then delivered to the corn drying facility at 85°C (Fig. 3.1). If the produced temperature decreases below 52°C (HE1 dT I), operation mode 2 becomes active. The principle for operation mode 2 and 3 is the same as for operation mode 1, just with different temperature levels. b) The contributed power from the CHPU and the storage to the corn drying process at the three operation modes. The power from the storage (313 kW/d for operation mode 1) should never be higher than that of the CHPU (330 kW/d for operation mode 1). Therefore the maximum preheating air stream temperature is 42°C (see Table 3.8).

4. Results

This chapter presents three-dimensional simulation results with and without the control system. The simulations run without the control system simulate the charging period, while the ones run with the control system simulate charging and discharge. The aim of the simulations is to investigate flow behavior and heat transport, analyze temperature profiles, and assess losses system efficiency.

4.1 Simulations without the CDCS

These simulations model the charging period of the thermal storage system without any connection to the control system. The purpose of these simulations is to understand the flow behavior and heat transfer in the storage system, and to identify locations and magnitudes of heat losses. They also support the discharging strategy, which will depend on the overall temperature profile near wells.

I have changed the injection temperatures for Runs 1 - 3 to assess charged temperature distribution and heat loss. The active wells in these three runs are for injection Well 1 and for production Well 3. Table 4.1 provides the simulation parameters, which are complementary to the information provided in Table 3.4, Table 3.5 and Table 3.6.

Table 4.1: Simulation parameters for Run 1 - 3. All three runs have the same parameters, except of injection well temperature. The injection temperature for Run 1 is 90°C, for Run 2 is 75°C and for Run 3 is 60°C.

Simulation Parameter	Symbol	Unit	Value
Initial domain temperature	T_i	°C	12
Injection well temperature at Well 1	T_{inj}	°C	90/75/60
Reference pressure	p_{ref}	Pa	101325
Injector/Producer absolute rate at Well 1/Well 3	q	m^3/s	0.001
Time step	Δt	h	2.4
Total simulation time	t	days	90

Fig. 4.1 to Fig. 4.3 show the temperature distribution of the storage system and its surroundings, when charging the initially cold system with hot water. The maximum Peclet number for Runs 1 - 3 is approximately 330 which indicates that heat in the

UTES is transferred via advection and diffusion, which is also visible in the figures below. All vertical cross sections shown in this chapter are perpendicular to the flow direction of the groundwater.

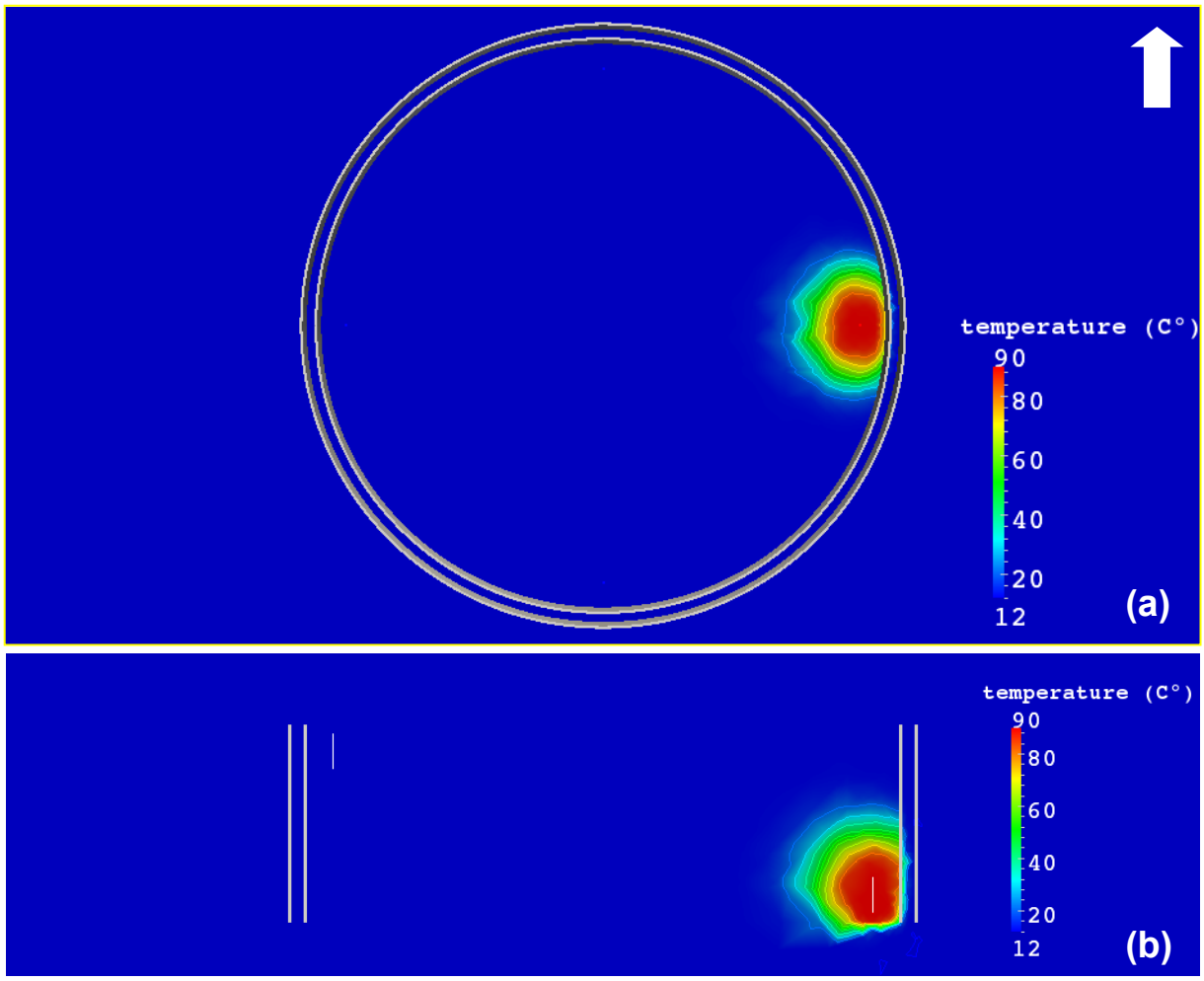

Fig. 4.1: Temperature cross section after 1 day for Run 1. a) Horizontal cut-plane through the injection well. b) Vertical cut-plane through both wells. The injection well is located at the bottom right and the production well is located at the top left of the storage system. The two grey hollow cylinder represent the walls of the storage. The arrow shows the direction of the groundwater flow. Temperature contours are separated by 10 °C.

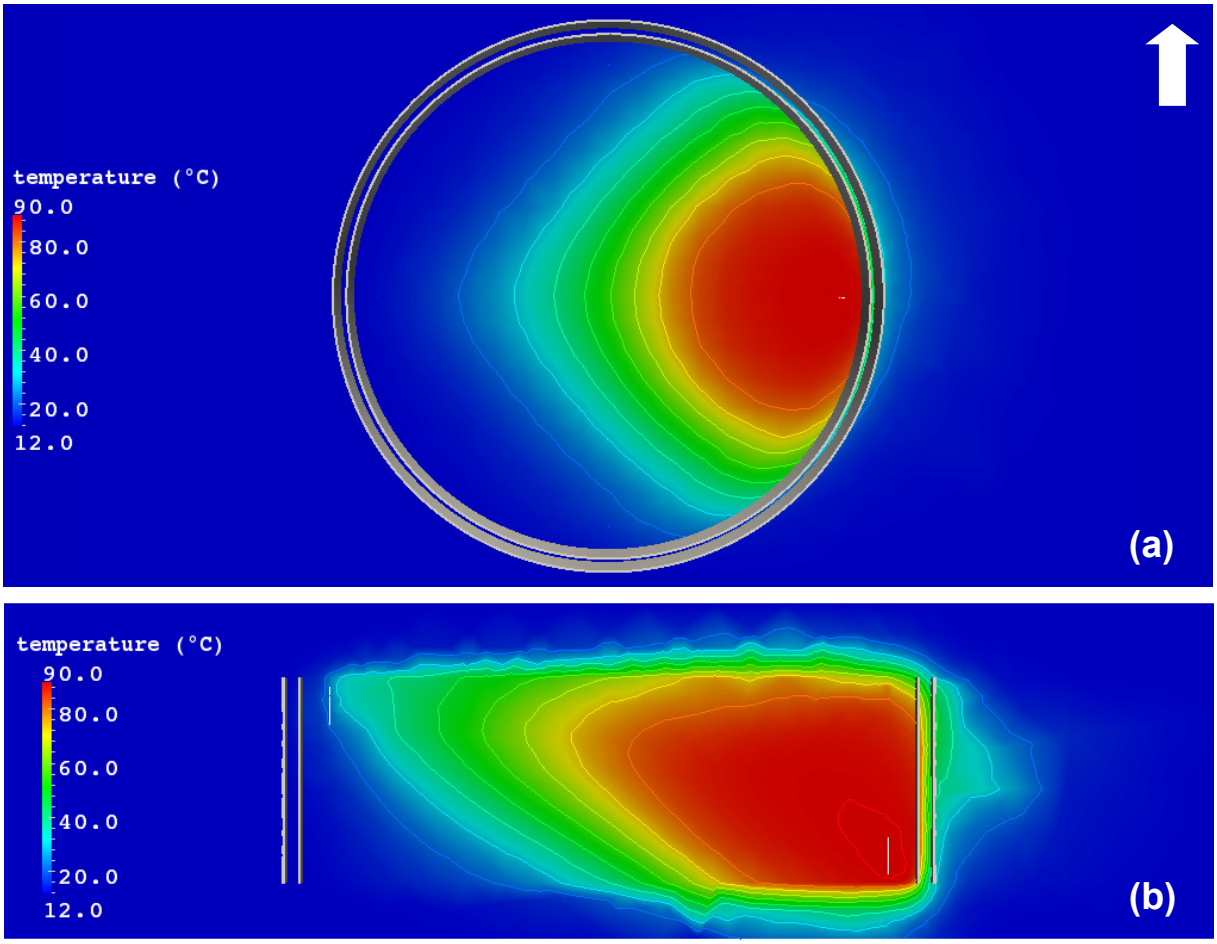

Fig. 4.2: Temperature cross section after 45 days for Run 1. a) Horizontal cut-plane through the injection well. b) Vertical cut-plane through both wells. Hot fluid rises, because its density is lower than that of cool fluid. Therefore the hotter regions develop at the top of the storage. The arrow shows the direction of the groundwater flow. Temperature contours are separated by 10 °C.

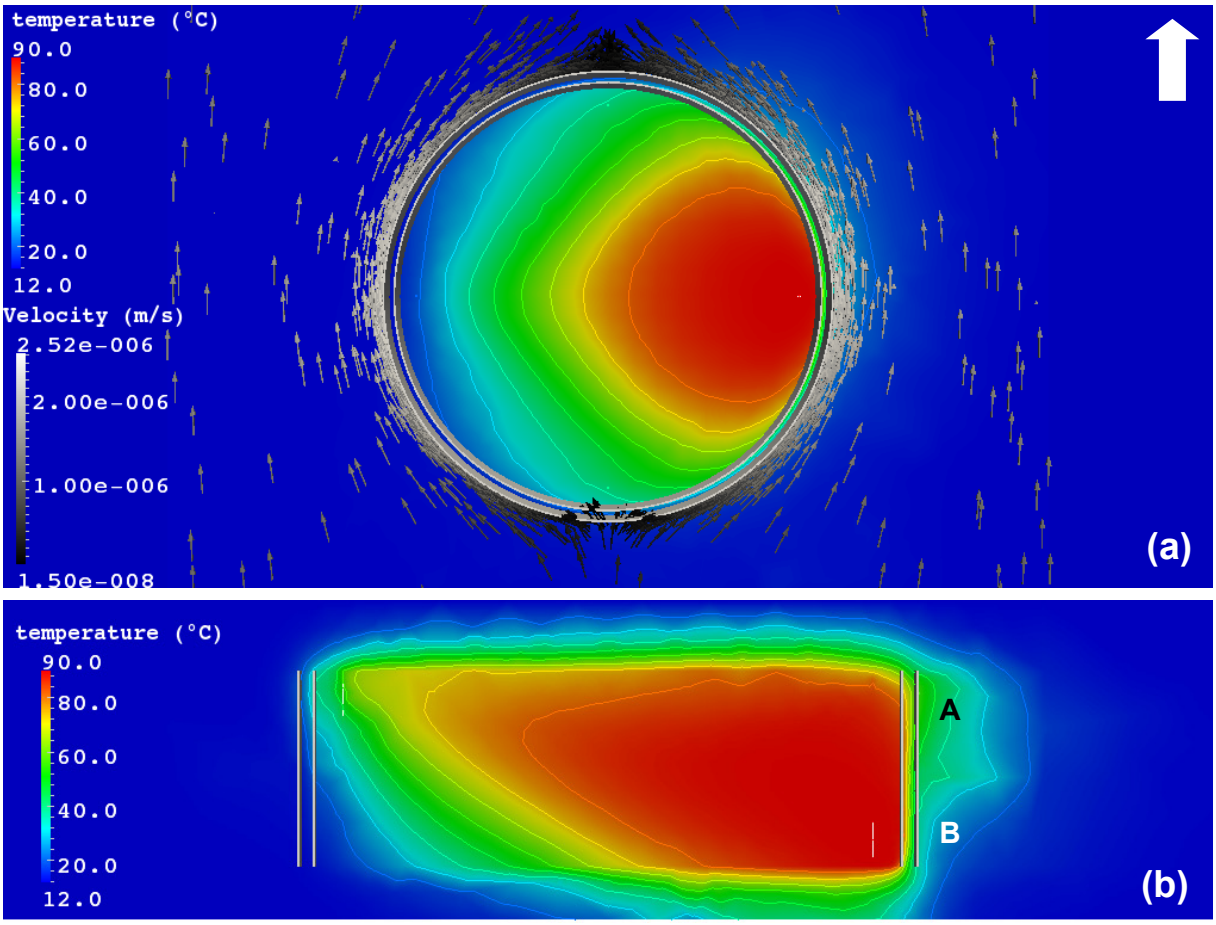

Fig. 4.3: Temperature cross section after 90 days for Run 1. a) Horizontal cut-plane through the injection well including groundwater flow pattern. The speed of the groundwater flow is approximately $1x10^{-6}$ to $1x10^{-8}$ m/s, b) Vertical cut-plane through both wells perpendicular to the flow direction of the groundwater. Temperature contours are separated by 10 °C. A) Due to heat conduction through the walls the unsaturated gravel region located outside of the storage is warmed. B) Groundwater flow occurs in the saturated gravel region located outside of the storage below the unsaturated one (Fig. 4.4). The groundwater is warmed due to heat conduction through the walls. The maximum temperature of the groundwater after 90 days of charging is approximately 40°C.

The groundwater flow around the storage system is shown in Fig. 4.4. This flow is fast, nevertheless it is heated due to diffusion by the hot fluid inside the storage. The velocity is higher at the left and right side of the storage and lower at the front and back side. The temperature gradient between the storage system and its groundwater region is the highest, which causes high heat conduction through the storage boundaries and therefore higher losses.

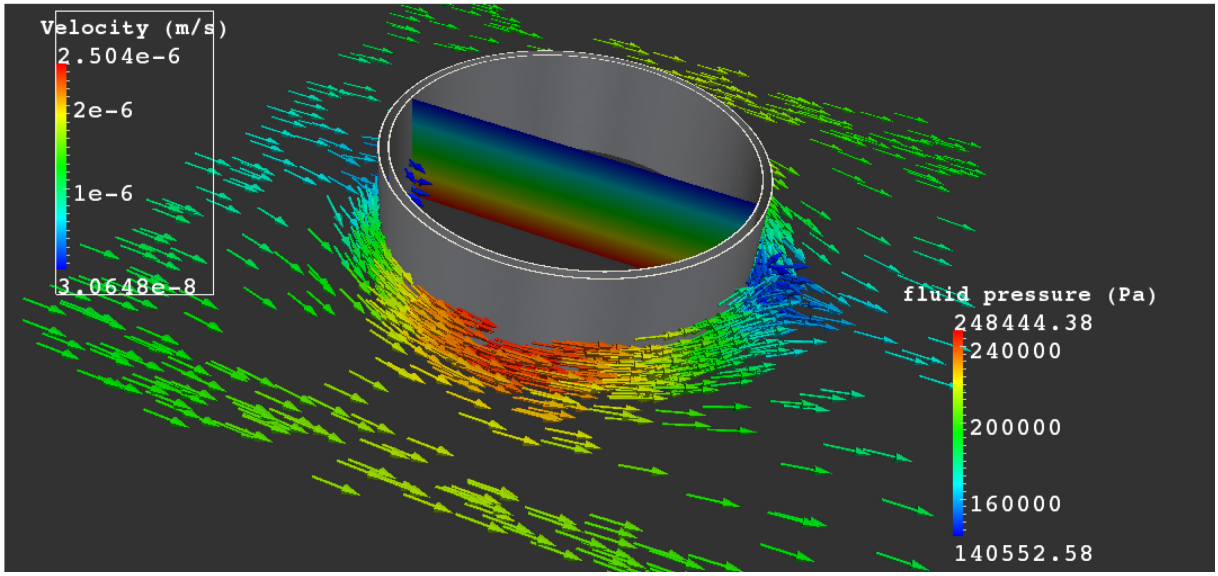

Fig. 4.4: Groundwater flow around the storage system and fluid pressure profile inside the storage. The groundwater velocity is approximately $1x10^{-6}$ m/s.

Velocity direction and magnitude together with pressure is shown in Fig. 4.5. The relative pressure causes fluid flow and has its extreme value near the wells.

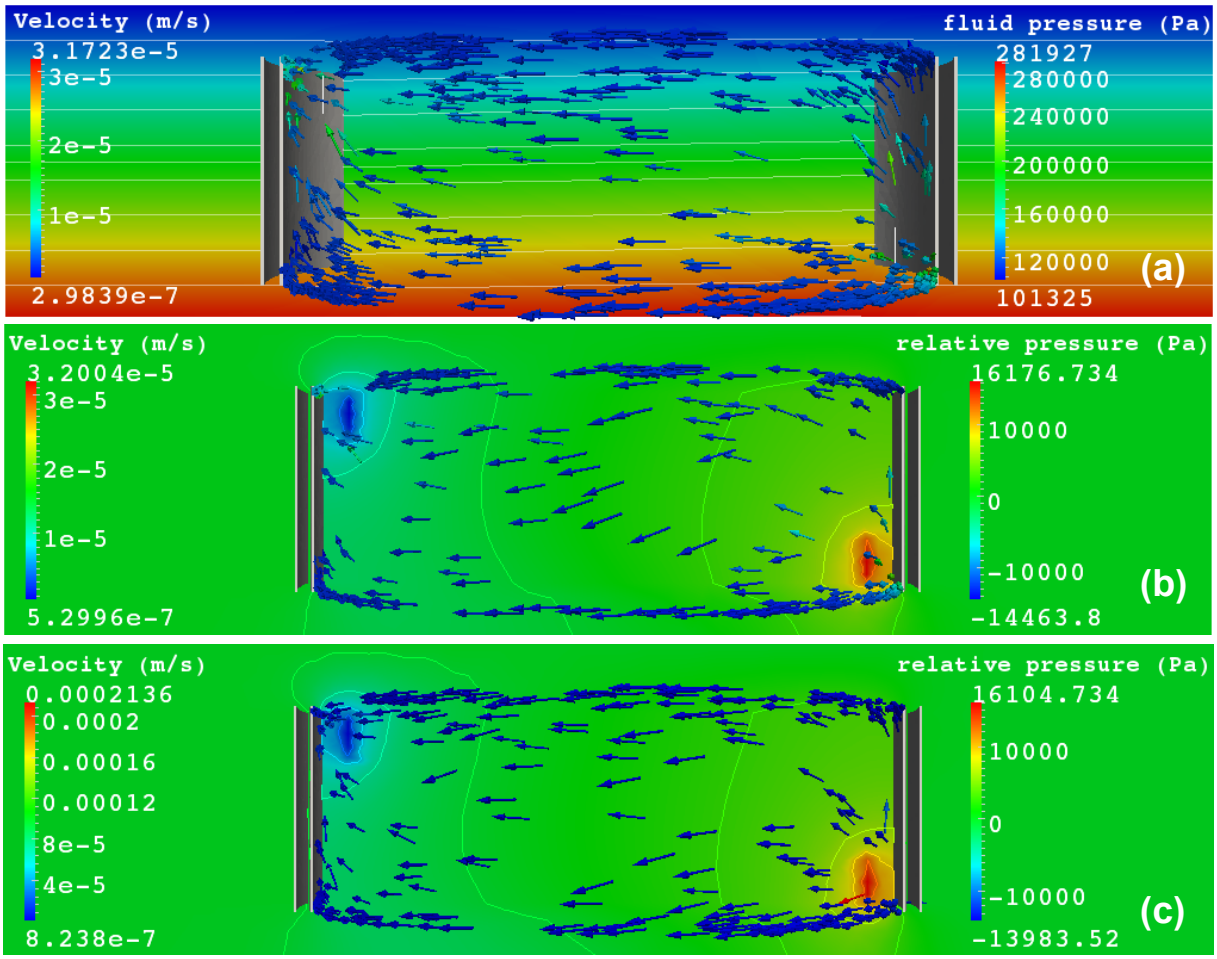

Fig. 4.5: Velocity vectors and pressure contours on a vertical cut-plane through both wells for Run 1. a) Velocity magnitude and fluid pressure after 1 day. b) Velocity magnitude and relative pressure after 45 days. c) Velocity magnitude and relative pressure after 90 days. Hot fluid rises due to convection to the top and cools as it approaches the producer and consequently moves downward. The velocity differences increases with time and are highest near the wells and near the walls.

(a)

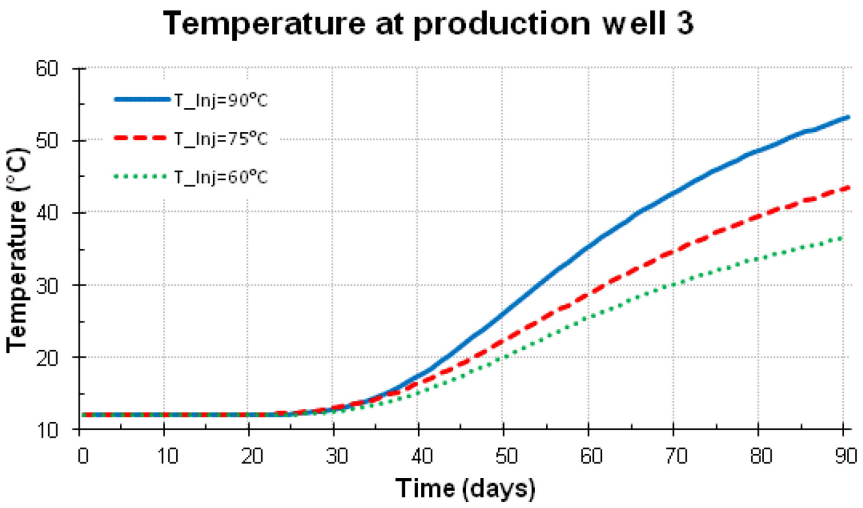

(b)

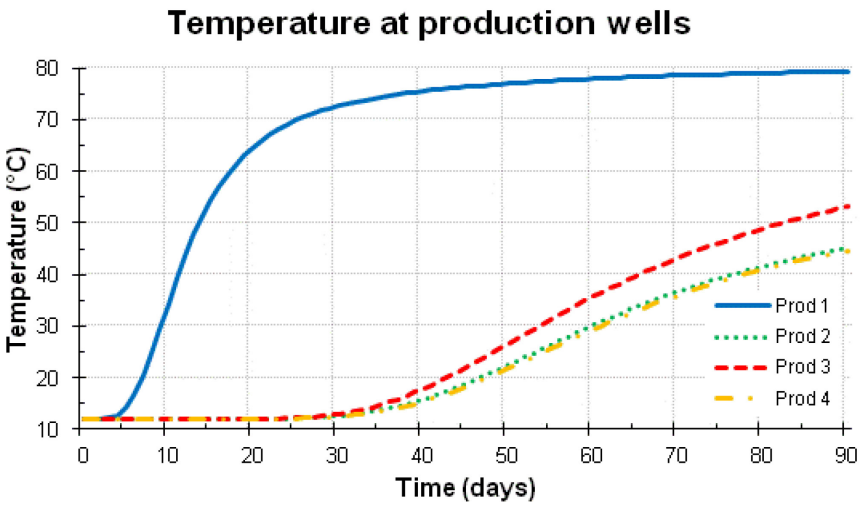

Fig. 4.6: Monitored temperature at production well 3 and well 1,2 and 4. In all 3 runs well 3 is the one that is always producing with injection well 1 a) Temperature profile at production well 3 for Run 1 - 3. The "breakthrough" is approximately after 25 days. The temperature at the production well after 90 days is for Run 1 (T_{inj}=90°C) 53°C, for Run 2 (T_{inj}=75°C) 43°C and for Run3 (T_{inj}=60°C) 37°C. b) Monitored temperature at all 4 wells. The highest temperature is at well 1, which is directly above the injection well. The exact well locations are shown in Fig. 3.11, Fig. 3.12 and Fig. 3.13.

The simulation for charging yields an evolution of producer well temperature shown in Fig. 4.6. These graphs give an idea when, where and how fast the temperature of the produced fluid grows.

The evolution of temperature at production well 3 for Runs 1 - 3 is shown in Fig. 4.6a. It is relatively obvious that higher injection temperatures yield higher temperatures at the production wells. Taking a closer look however, at end point temperatures, the temperature difference between Run 1 and Run 2 is 10°C and the difference

between Run 2 and Run 3 is 6°C. This means that higher injection temperatures yield higher heat losses. This observation is also complementary to the results shown in Fig. 4.8.

Fig. 4.6b observes the evolution of temperature at all 4 production well locations. This graph can support the decision of an efficient discharging strategy because the exact temperature at any time at all production wells is known.

The energy -and exergy flow rate during charging are shown in Fig. 4.7. Energy is the capacity of doing work and the energy input to a storage system during charging is expressed as (Dincer and Rosen, 2002),

$$E_c = \dot{m}_c c t_c (T_{in} - T_{out}) \tag{4.1}$$

where $\dot{m}_c$ is the constant water injection rate, t_c the time period for charging, T_{in} the injection temperature and T_{out} the produced temperature. The energy inputs for Run 1 (T_{inj} =90°C), Run 2 (T_{inj} =75°C) and Run 3 (T_{inj} =60°C) after 90 days are 575 MWh, 555 MWh and 358 MWh, respectively.

Exergy is defined as the maximum useful work that can be produced by a stream of energy as it comes in equilibrium with the reference environment and is often called available energy. Exergy analysis is useful in identifying magnitudes of process inefficiencies and provides an alternative of assessing and comparing UTES. The exergy input during charging to a storage system is expressed as (Dincer and Rosen, 2002),

$$\varepsilon_c = E_c - \dot{m}_c c t_c T_0 \ln\left(\frac{T_{in}}{T_{out}}\right) \tag{4.2}$$

where E_c is the energy input, T_0 is the surrounding temperature. The exergy inputs for Run 1 (T_{inj}=90°C), Run 2 (T_{inj}=75°C) and Run 3 (T_{inj}=60°C) after 90 days are 75.9 MWh, 63.8 MWh and 30.8 MWh, respectively.

The power output and the cumulative heat transferred through the boundaries of the storage system are shown in Fig. 4.8. Most of the heat (-194 kWh) is lost through the artificial walls of the storage system. After 90 days the total heat loss for Run 1 is about -460 kWh, for Run 2 -380 kWh and for Run 3 -280 kWh. For the heat loss calculations I have assumed that the walls and clay layers are essentially impermeable, only conductive heat flow is addressed.

(a)

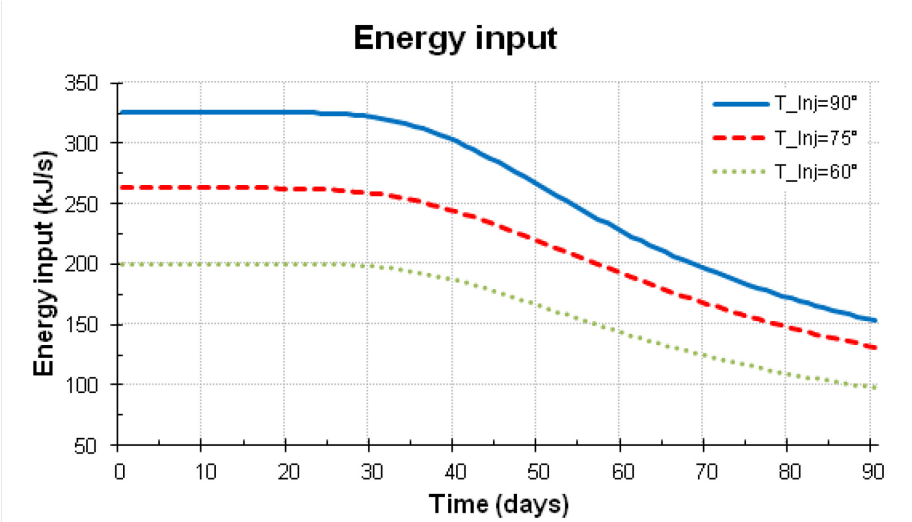

(b)

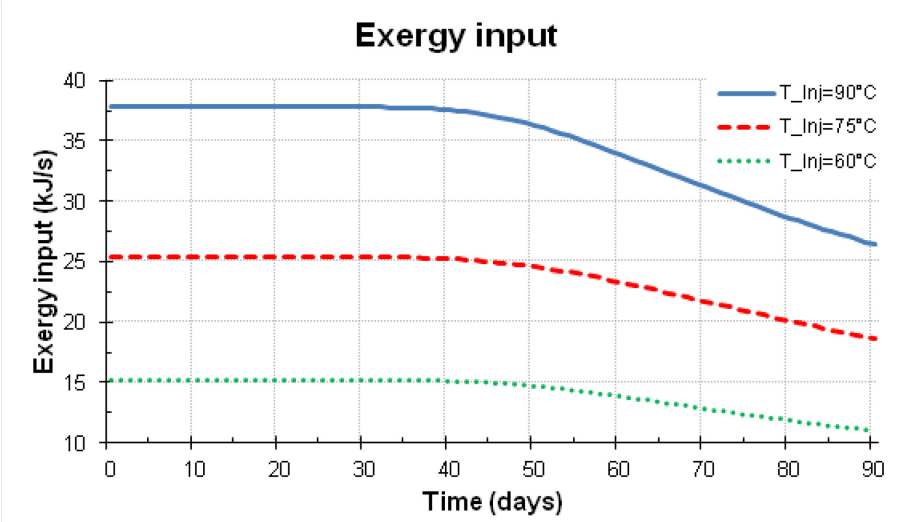

Fig. 4.7: a) Energy flow rate over the 90 days charging period at different injection temperatures. b) Exergy flow rate over the 90 days charging period at different injection temperatures.

(a)

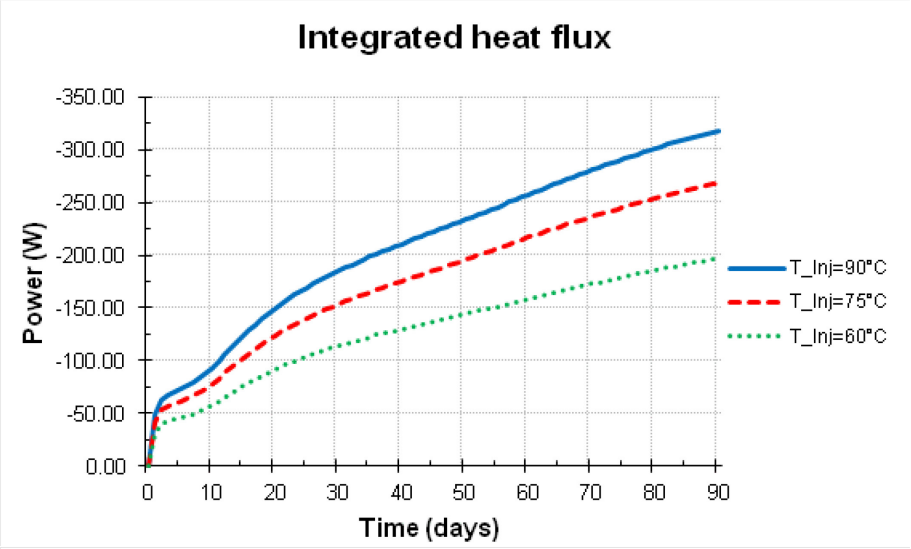

(b)

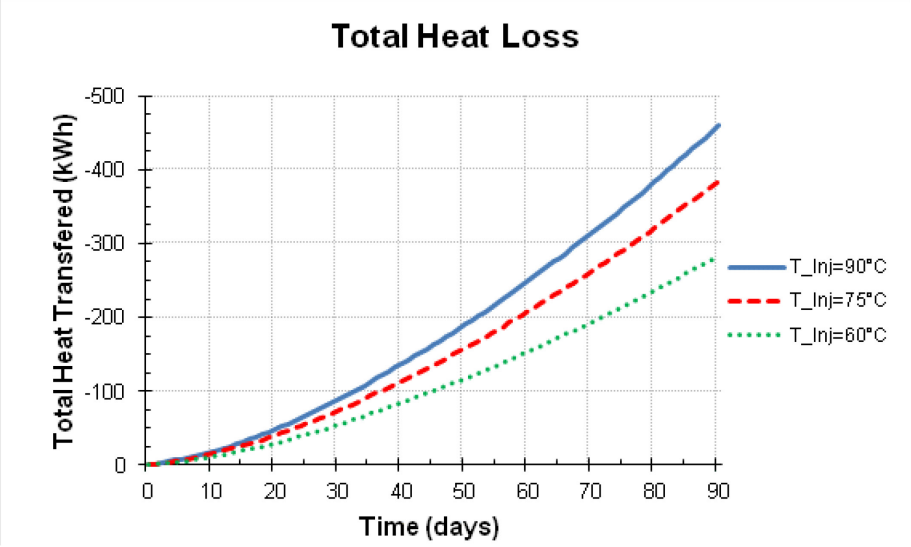

Fig. 4.8: a) Integrated heat flux through inner concrete wall, top -and bottom material interface of the storage system at different injection temperatures. b) Total heat transferred through the gravel-material boundaries of the storage system at different injection temperatures.

For Runs 4 - 5 I have changed the injection rate to investigate the effect to heat transport, temperature distribution and heat loss. The active wells for injection and production are the same as for Runs 1 - 3. Run 4 has the same simulation parameters as Run 1, however the simulation time is approximately 5 months. In Run 5 I have reduced the injection rate from 1 l/s to 0.5 l/s. Table 4.2 provides the simulation parameters, which are complementary to the information provided in Table 3.4, Table 3.5 and Table 3.6.

Table 4.2: Simulation parameters for Run 4 - 5. Both runs have the same parameters, except of injection well rate. The injection rate for Run 4 is 0.001 m^3/s (≈1l/s), for Run 5 is 0.0005 m^3/s (≈0.5l/s).

Simulation Parameter	Symbol	Unit	Value
Initial domain temperature	T_i	°C	12
Injection well temperature at Well 1	T_{inj}	°C	90
Reference pressure (Top)	p_{ref}	Pa	101325
Injector/Producer absolute rate at Well 1/Well 3	q	m^3/s	0.001/0.0005
Time step	Δt	h	2.4
Total simulation time	t	days	150

Fig. 4.9 shows the temperature distribution in the storage system after 90 days of charging with hot water. It shows a gravity-driven fluid flow caused by density difference of hot and cold water. A comparison between Fig. 4.9 and Fig. 4.2 indicates that at lower injection rates the heat flow has more time to diffuse and therefore the temperature outside of the storage system, especially at the bottom, is higher.

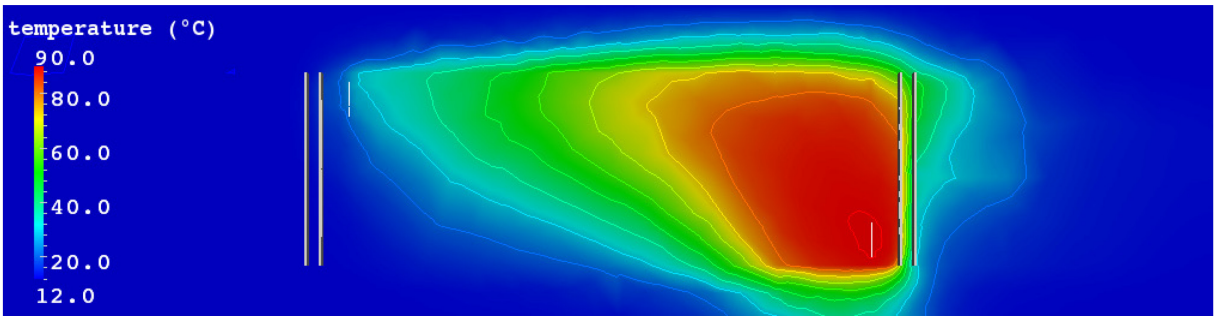

Fig. 4.9: Temperature cross section at a vertical cut-plane through both wells after 90 days for Run 5. A higher amount of diffusion can be observed comparing to Fig. 4.2. Temperature contours are separated by 10 °C.

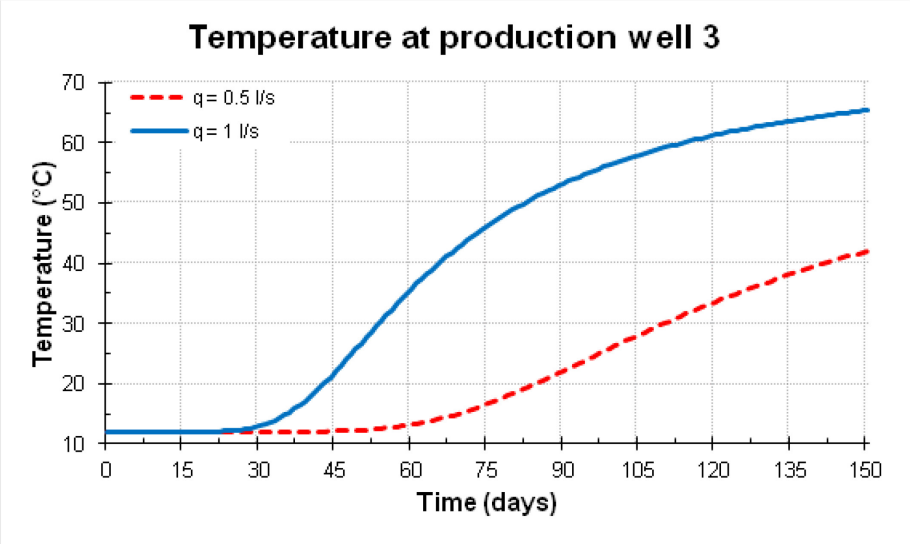

Fig. 4.10: Temperature vs. time at production well 3 when injecting at different rates. The "breakthrough" for Run 4 (q=0.5l/s) is approximately after 50 days and for Run5 (q=1l/s) is approximately after 25 days.. The temperature at production well 3 after 150 days is for Run 4 42°C and for Run 5 65°C.

The temperature evolution at production well 3 for Runs 4 and 5 is shown in Fig. 4.10. The temperature after 150 days for Run 4 (q = 0.5 l/s) is approximately 42 °C and the temperature after 75 days for Run 5 (q = 1 l/s) is approximately 46 °C. At these times the same amount of hot fluid has been injected, however the temperature at production well 3 is approximately 4 °C higher for the run with higher injection rate. A possible reason for this could be the higher amount of diffusion due to lower velocity magnitudes.

Fig. 4.11 shows the power output and the cumulative heat transferred through the boundaries of the storage system for Run 4 and Run 5. The total heat loss after 150 days for Run 4 (q = 0.5 l/s) is approximately -590 kWh and after 75 days for Run 5 (q = 1 l/s) it is -340 kWh. At these times the same amount of hot fluid has been injected, however the total heat loss is roughly 250 kWh higher, when injecting the water at lower rates. This means that at higher rates, less heat is lost through the boundaries and the storage system is more efficient.

(a)

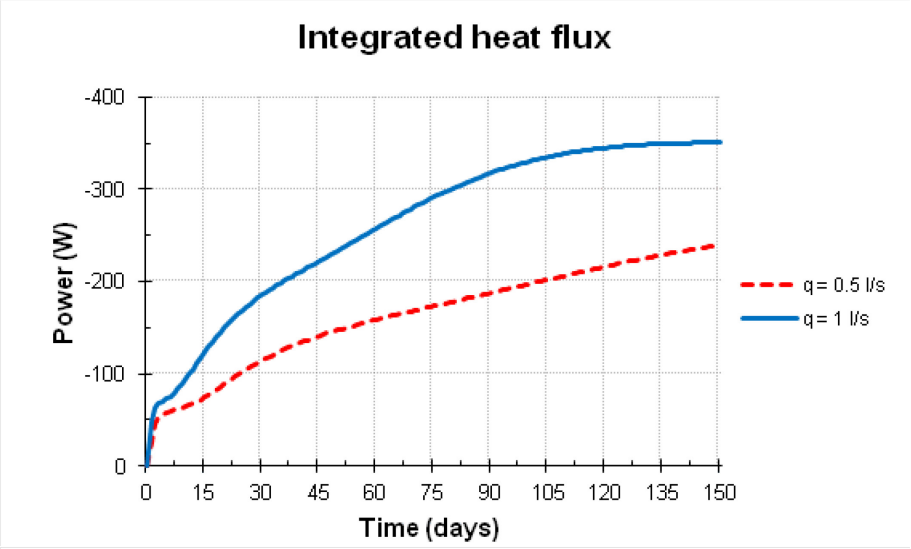

(b)

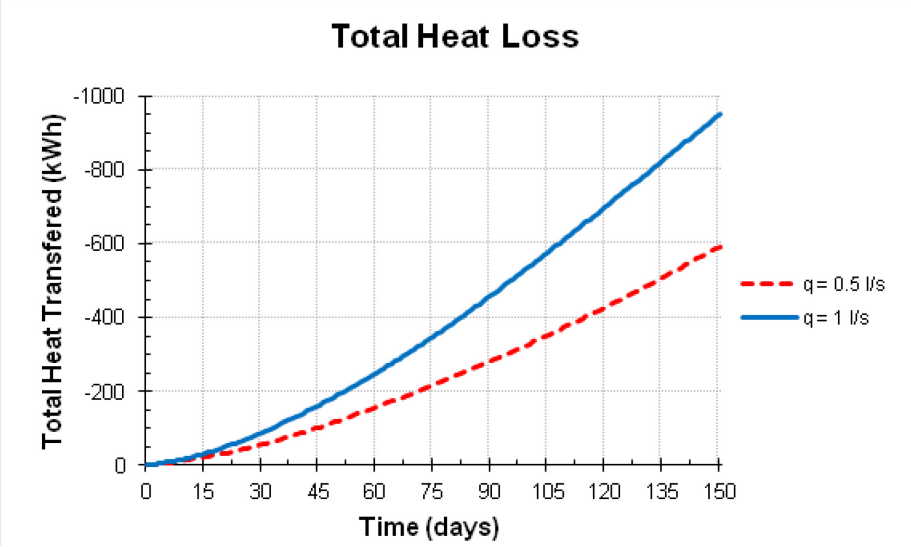

Fig. 4.11: a) Integrated heat flux through inner concrete wall, top -and bottom material interface of the storage system at different injection rates (Run 4 = 0.5 l/s, Run 5 = 1 l/s). b) Total heat transferred through the gravel-material boundaries of the storage system at different injection rates.

Run 6 simulates the storage period of the UTES, thus no fluid is injected or produced. This run is a particular case to address how well the storage system prevents heat loss and also helps to investigate heat transport effects on temperature distribution and heat loss. However in the practical application such long storage period does not really exist. In this run I assume that the storage (gravel region) is uniformly charged to 90°C, while all other regions have an initial temperature of 12°C. Table 4.3 provides the simulation parameters, which are complementary to the information provided in Table 3.4, Table 3.5 and Table 3.6.

Table 4.3: Simulation parameters for Run 6.

Simulation Parameter	Symbol	Unit	Value
Initial temperature for gravel (storage) region	T_i	°C	90
Initial temperature for all other regions	T_i	°C	12
Reference pressure (Top)	p_{ref}	Pa	101325
Time step	Δt	h	2.4
Total simulation time	t	days	150

Fig. 4.12 shows the temperature distribution of the model after 75 days and 150 days of hot water storage. In the middle of the storage the water stays warm the longest. Circular motion of fluid, higher velocities along the storage walls and lower ones at the bottom are observations which are attributable to natural convection. These great downward velocities arise, because the cell nearest to the walls exhibit the lowest temperatures and greatest densities in the domain (Dincer and Rosen, 2002).

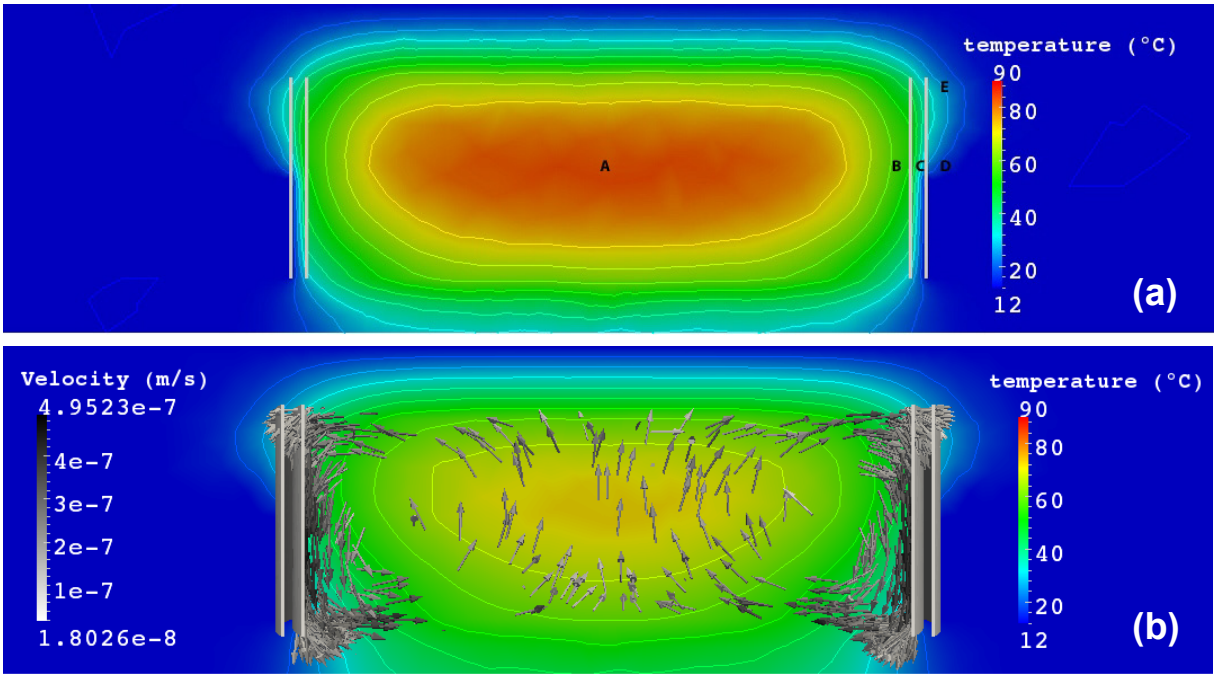

Fig. 4.12: Temperature cross section at a vertical cut plane for Run 6. (a) Temperature distribution in the whole domain after 75 days. The capital letters indicate the location of the temperature profiles in Fig 4.13 (b) Temperature distribution and velocity vectors after 150 days showing natural convection.

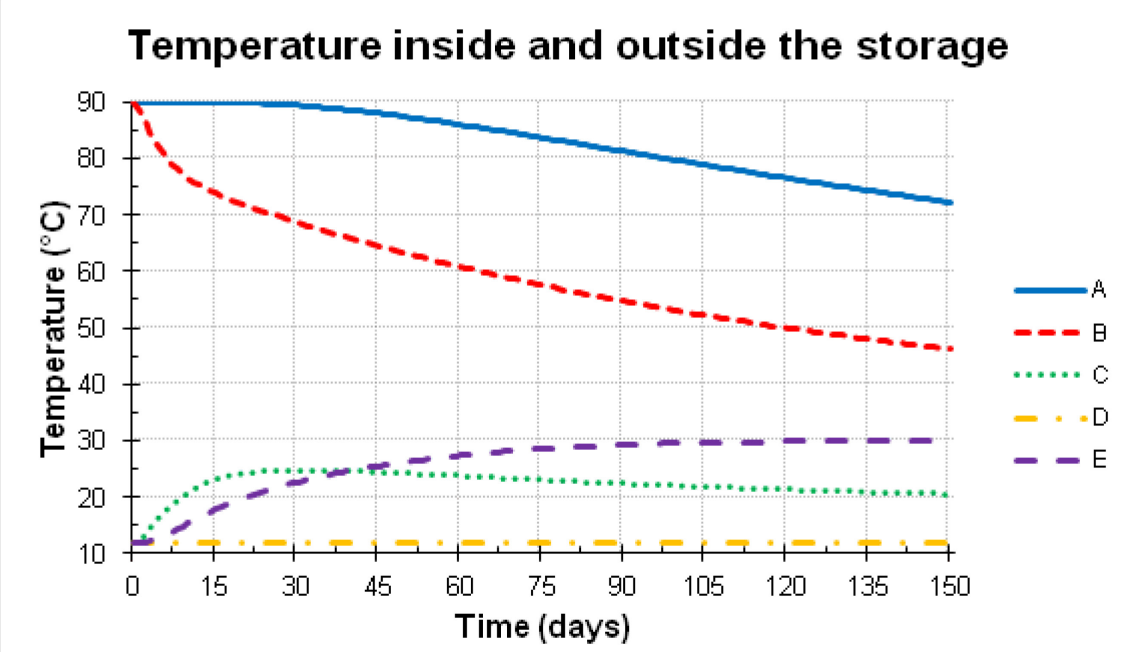

Fig. 4.13: Temperature profile at different locations (Fig 4.12a) of the storage domain. A is the temperature profile in the storage center, B is the temperature profile near the storage walls, C is the temperature profile between the two artificial walls, D is the temperature profile in the groundwater region near the second wall and E is the temperature profile in the unsaturated gravel region near the second wall.

The evolution of temperature at different locations of the domain, which are indicated by capital letters in Fig. 4.12a are shown in Fig 4.13. The temperature in the center of the storage (A) drops to about 72 °C after 150 days, which is just 12 °C lower than the initial temperature. Near the storage walls (B) the temperature drops 46°C below initial storage conditions. The temperature between the walls (C) increases in the first month from 12 °C to about 25°C. Then it drops slowly to 20°C after 5 months. The temperature in the groundwater region (D) near the walls is constant and not effected by the hot water in the storage, because in this run it is assumed that the temperature of the groundwater is constant. At the top of the unsaturated gravel region near the walls (E) the temperature increases from 12°C to about 30 °C.

Fig. 4.14 shows the power output and the cumulative heat transferred through the boundaries of the storage system for the storage case (Run 6). After 5 months the storage system loses -1250 kWh of heat at which the loss in the first 15 days is the highest. The highest amount of heat is lost through the first storage wall, amounting to -568 kWh. The lowest amount of heat, -295 kWh, is lost through the storage bottom, which is the gravel - clay marl interface. About -380 kWh of heat is transferred through the storage top, the gravel - loess interface.

(a)

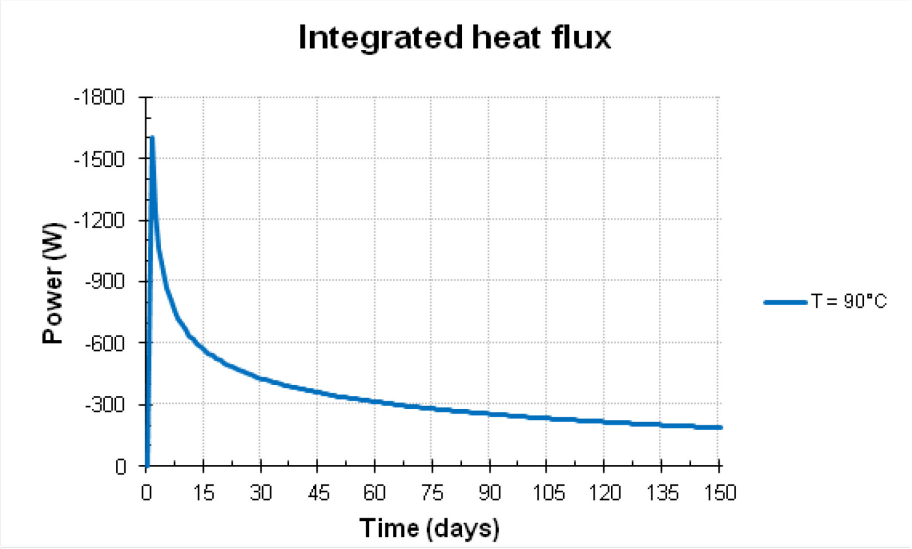

(b)

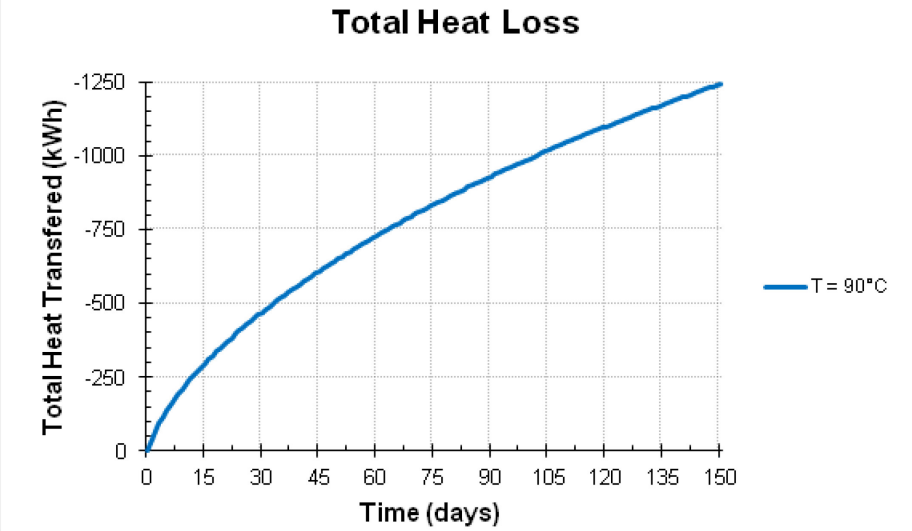

Fig. 4.14: a) Integrated heat flux through inner concrete wall, top -and bottom material interface of the storage system for Run 6 b) Total heat transferred through the gravel-material boundaries of the storage system for Run 6. The initial temperature in the storage is 90 °C.

4.2 Simulations with the CDCS

These simulations model the charging and discharging period of the thermal storage system with a connection to the control system for providing optimal corn drying flow rates and temperatures. The main purpose of these simulations is to identify the hottest regions in the storage system to optimize the discharging process. I have changed the number of active wells, the charging process and the operation modes for Runs 2 - 6 to investigate the temperature distribution and overall system efficiency. For Run 1 the storage is set to an initial uniform temperature of 85°C in the gravel region, which is the charging temperature from the CHPU. The CHPU delivers the unused energy in the form of hot water to the storage from June until September.

The active wells in the first run are for injection Well 1 and for production Well 3. Table 4.4 provides the simulation parameters, which are complementary to the information provided in Table 3.4, Table 3.6 and Table 3.7.

Table 4.4: Simulation parameters of discharging for Run 1 - 6. There is no initial domain temperature for Run 2 - 6, because the charging process is simulated. Also the active injection and production wells are different for Run 2 - 6.

Simulation Parameters for discharging	Symbol	Unit	Value
Initial domain temperature for Run1	T_i	°C	85
Injection well temperature at Well 1	T_{inj}	°C	variable
Reference pressure	p_{ref}	Pa	101325
Injector/Producer absolute rate at Well 1/Well 3	q	m^3/s	variable
Time step	Δt	days	1
Total simulation time	t	days	56

Fig. 4.15 and Fig. 4.16 show the temperature distribution and the velocity vectors of the storage system and its surrounding, when discharging the initially hot system with cold water. The Peclet number is approximately in the same range as in the charging period, which indicates that heat in the UTES is transferred via advection and diffusion. This process and the accumulation of hot fluid at the top are visible in the figures below.

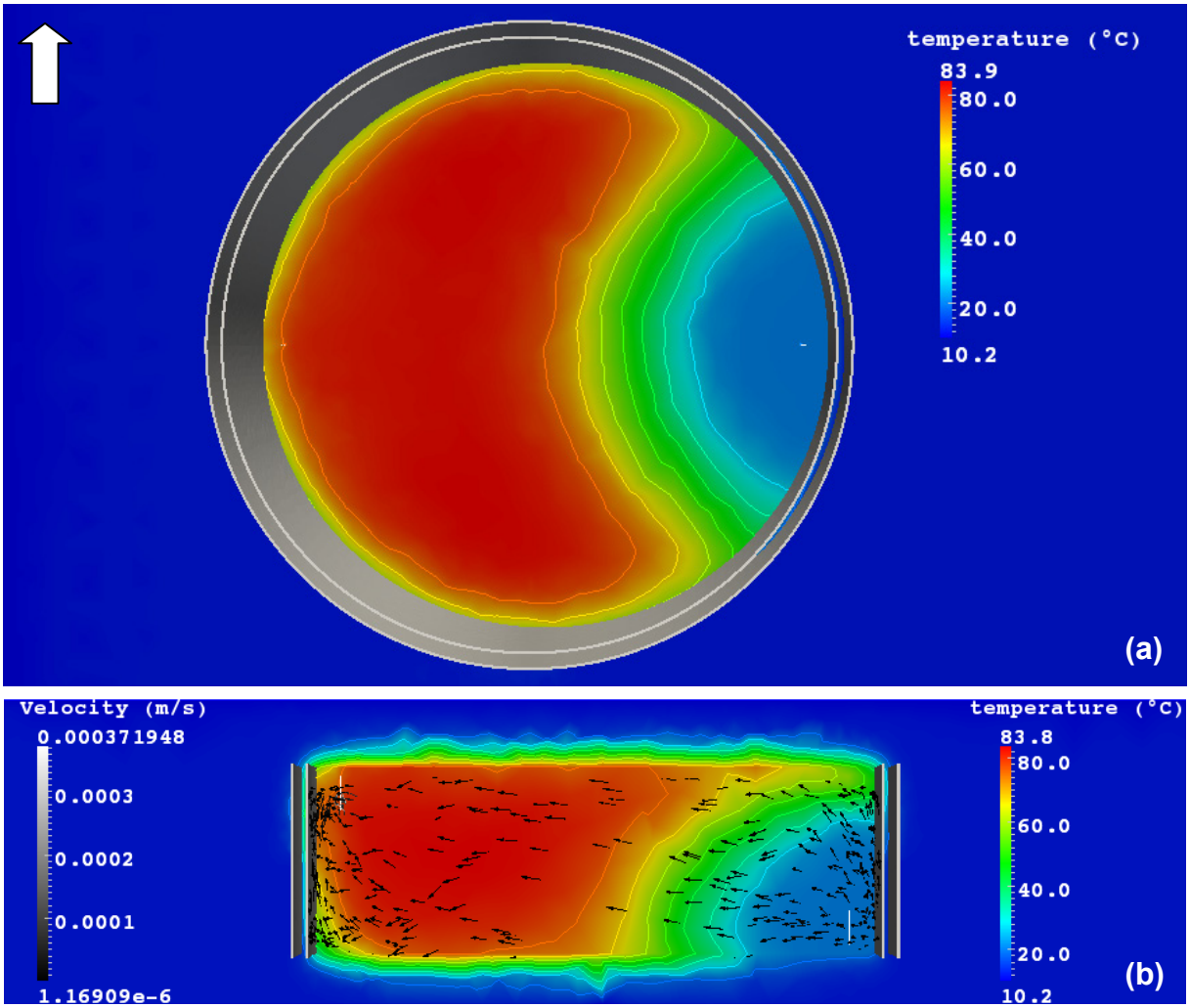

Fig. 4.15: Temperature cross section and velocity vectors after 10 days of discharging for Run 1. a) Horizontal cut-plane through the injection (right) and production (left) wells. b) Vertical cut-plane through both wells. The injection well is located at the bottom right and the production well is located at the top left of the storage system. The two grey hollow cylinders represent the walls of the storage. The arrow shows the direction of the groundwater flow. Temperature contours are separated by 10 °C.

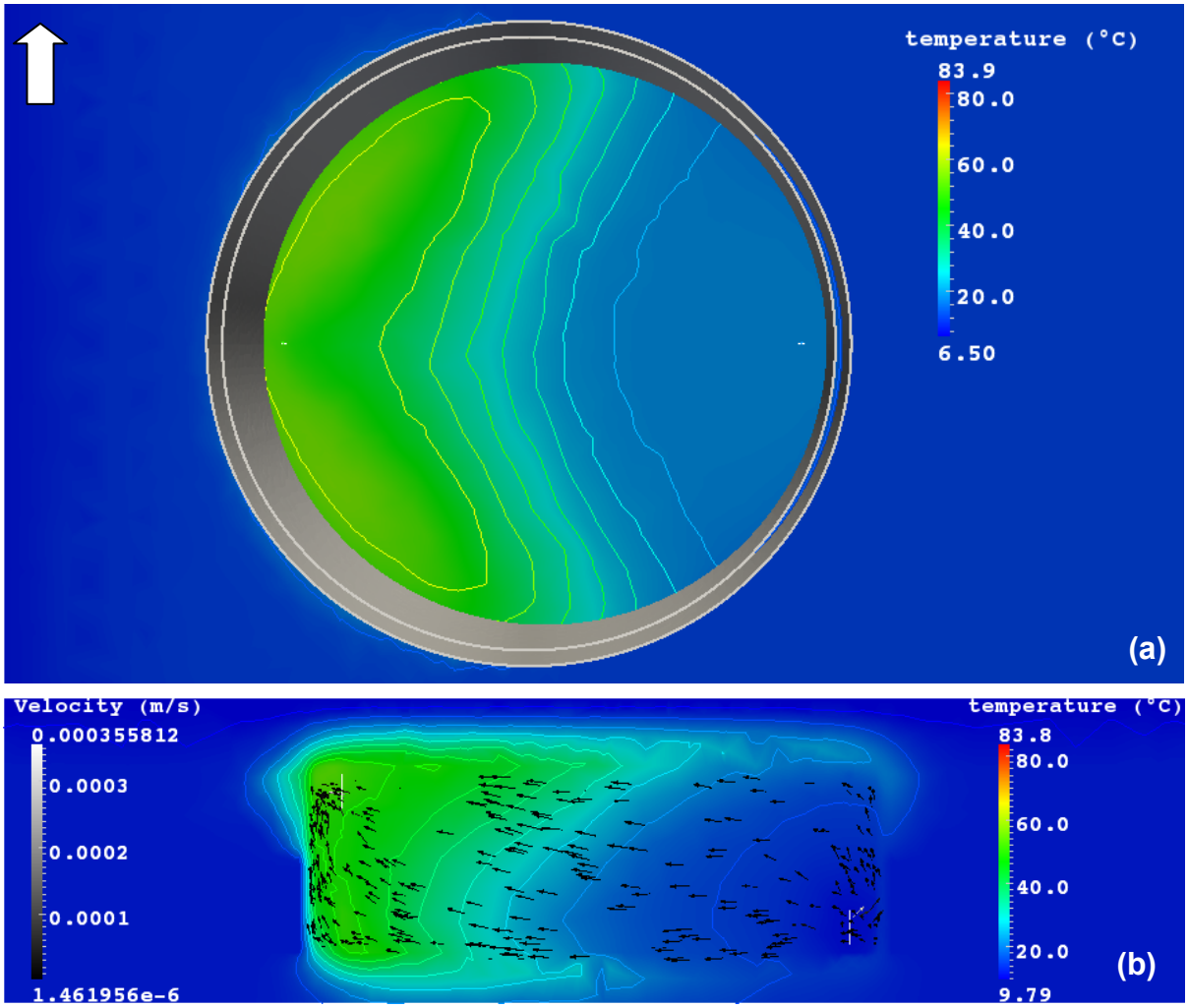

Fig. 4.16: Temperature cross section and velocity vectors after 42 days of discharging for Run 1. a) Horizontal cut-plane through the injection (right) and production (left) wells. b) Vertical cut-plane through both wells. Fluid flows from right to left and rises with increasing temperature. Cool fluid has a higher density than hot fluids and therefore cooler regions are at the bottom of the storage system.

In the next 5 runs the charging process is simulated to get a more realistic condition for discharging. The simulation parameters for the charging process of Run 2 and 4 are shown in Table 4.5. The temperature distribution of the storage system looks quite similar to Fig. 4.3, but the charging time is 30 days longer. The simulation parameters for the discharging process of Run 2 and 4 are shown in Table 4.5. Run 2 and Run 4 a quite similar, only the input parameters for operation mode 3 (Table 3.8) have been changed to increase the efficiency (Table 4.9 and Table 4.10).

Table 4.5: Simulation parameters of charging for Run 2 and 4.

Simulation Parameters for charging	Symbol	Unit	Value
Initial domain temperature	T_i	°C	12
Injection well temperature at Well 1	T_{inj}	°C	85
Reference pressure	p_{ref}	Pa	101325
Injector/Producer absolute rate at Well 1/Well 3	q	m^3/s	0.00108
Time step	Δt	days	1
Total simulation time	t	days	120

Fig. 4.6 shows that the temperature at production well 1 is the hottest. This well is located directly above injection well 1. Therefore I produce the hot fluid from production well 1 and inject the cold fluid from injection well 3 during the discharging phase. This well configuration allows me to produce for a quite long time hot water also because of the greatest possible distance between injection and production well.

Fig. 4.17 and Fig. 4.18 show the temperature distribution and the velocity vectors of the storage system and its surrounding during the discharging phase. The 56 days of discharging starts immediately after the 120 days of charging to avoid heat loss. The figures below show, that the hottest regions are in the vicinity of production well 1, but also near injection well 1. It is obvious that hot fluid rises and accumulates at the top of the storage system, however I haven't expected such hot regions near the bottom. Fig. 4.3 shows that during the charging phase heat diffuses from the gravel region to the clay marl region and this region doesn't lose much heat during the discharging phase, because of the absence of heat transport through convection and lower heat transfer due to conduction.

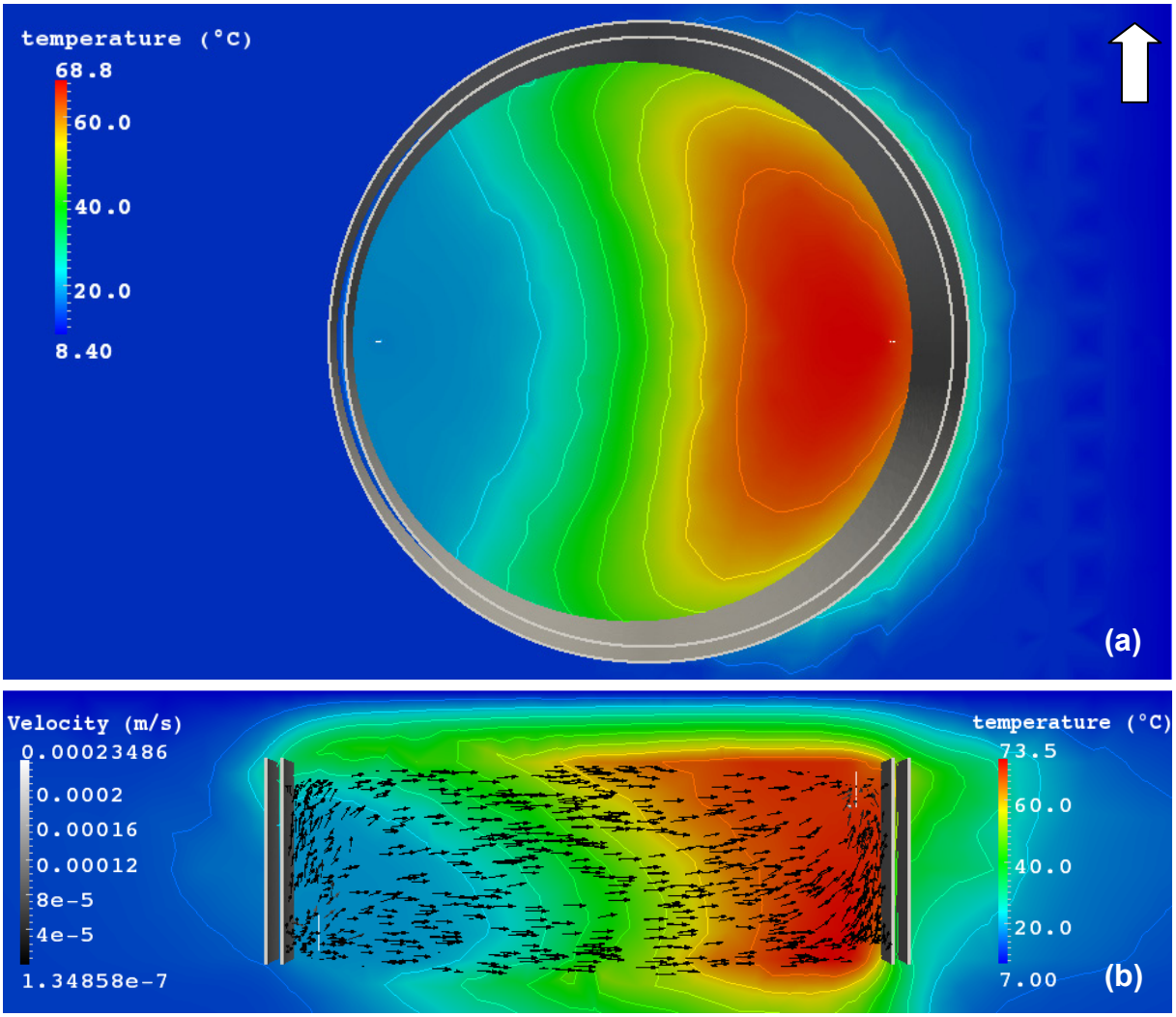

Fig. 4.17: Temperature cross section and velocity vectors after 20 days of discharging for Run 2. a) Horizontal cut-plane through the injection (left) and production (right) wells. b) Vertical cut-plane through both wells. The injection well is located at the bottom left and the production well is located at the top right of the storage system. Therefore fluid flows from right to left. Temperature contours are separated by 10 °C.

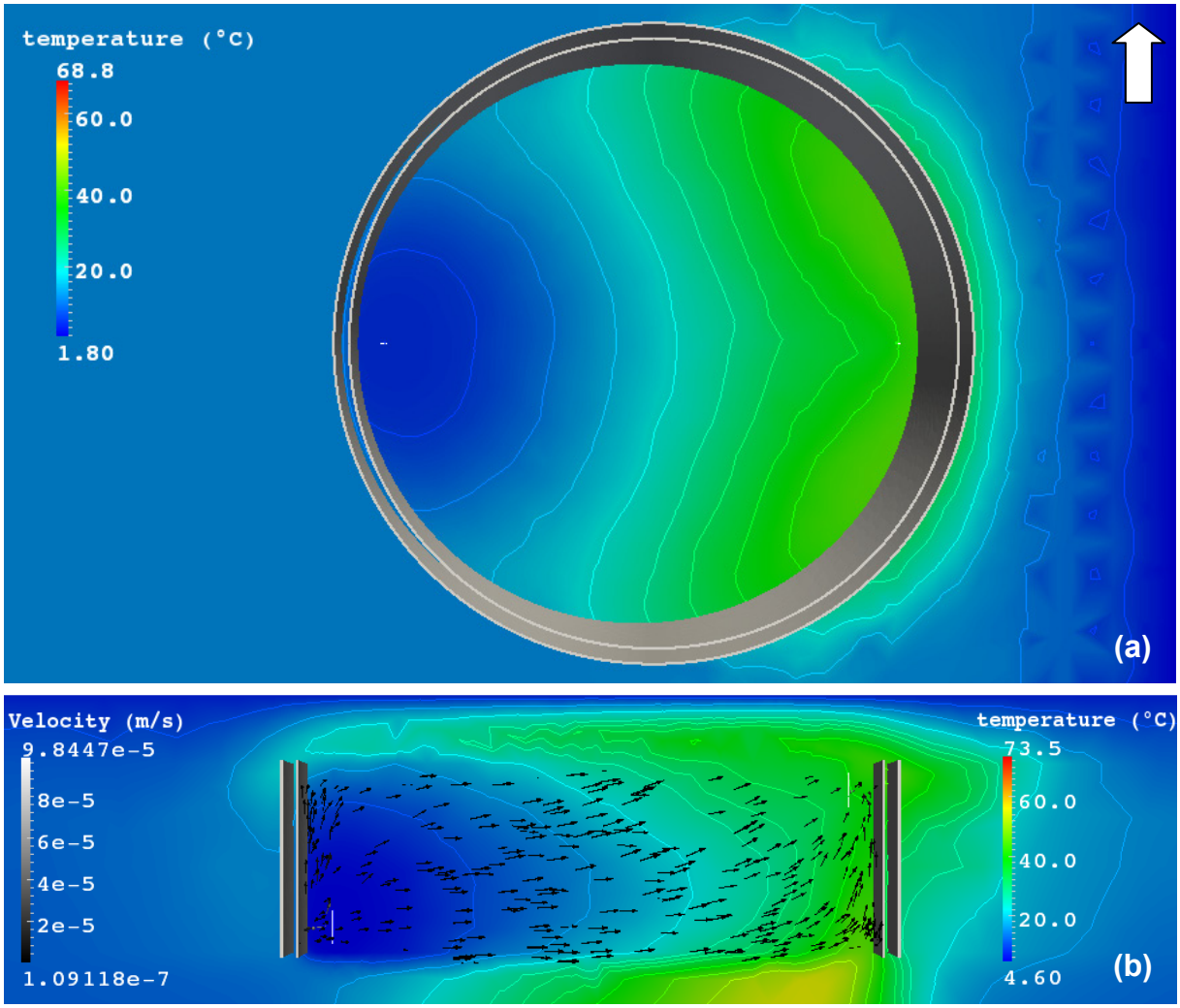

Fig. 4.18: Temperature cross section and velocity vectors after 56 days of discharging for Run 2. a) Horizontal cut-plane through the injection (left) and production (right) wells. b) Vertical cut-plane through both wells. Fluid flows from right to left and rises with increasing temperature. Cool fluid has a higher density than hot fluids and therefore cooler regions are at the bottom of the storage system.

For Run 3 I have changed the numbers of active wells. In the runs before I have used one injection and production well for charging and discharging. Now I inject from 2 wells and produce from 2 wells. Thus I get a bigger region of hot fluid, however the injection rate is half. The simulation parameters for the charging process of Run 3 are shown in Table 4.6 and for the discharging process in Table 4.4.

Table 4.6: Simulation parameters for Run 3.

Simulation Parameters for charging	Symbol	Unit	Value
Initial domain temperature	T_i	°C	12
Injection well temperature at Well 1 and Well 2	T_{inj}	°C	85
Reference pressure	p_{ref}	Pa	101325
Injector/Producer absolute rate at Well 1, 2 /Well 3, 4	q	m^3/s	0.00054
Time step	Δt	days	1
Total simulation time	t	days	120

Hot fluid is produced from production well 1 and 2 and cold fluid is injected from injection well 3 and 4 during the discharging phase. Fig. 4.19 shows the temperature distribution of the storage system and its surrounding during the discharging phase after 20 days.

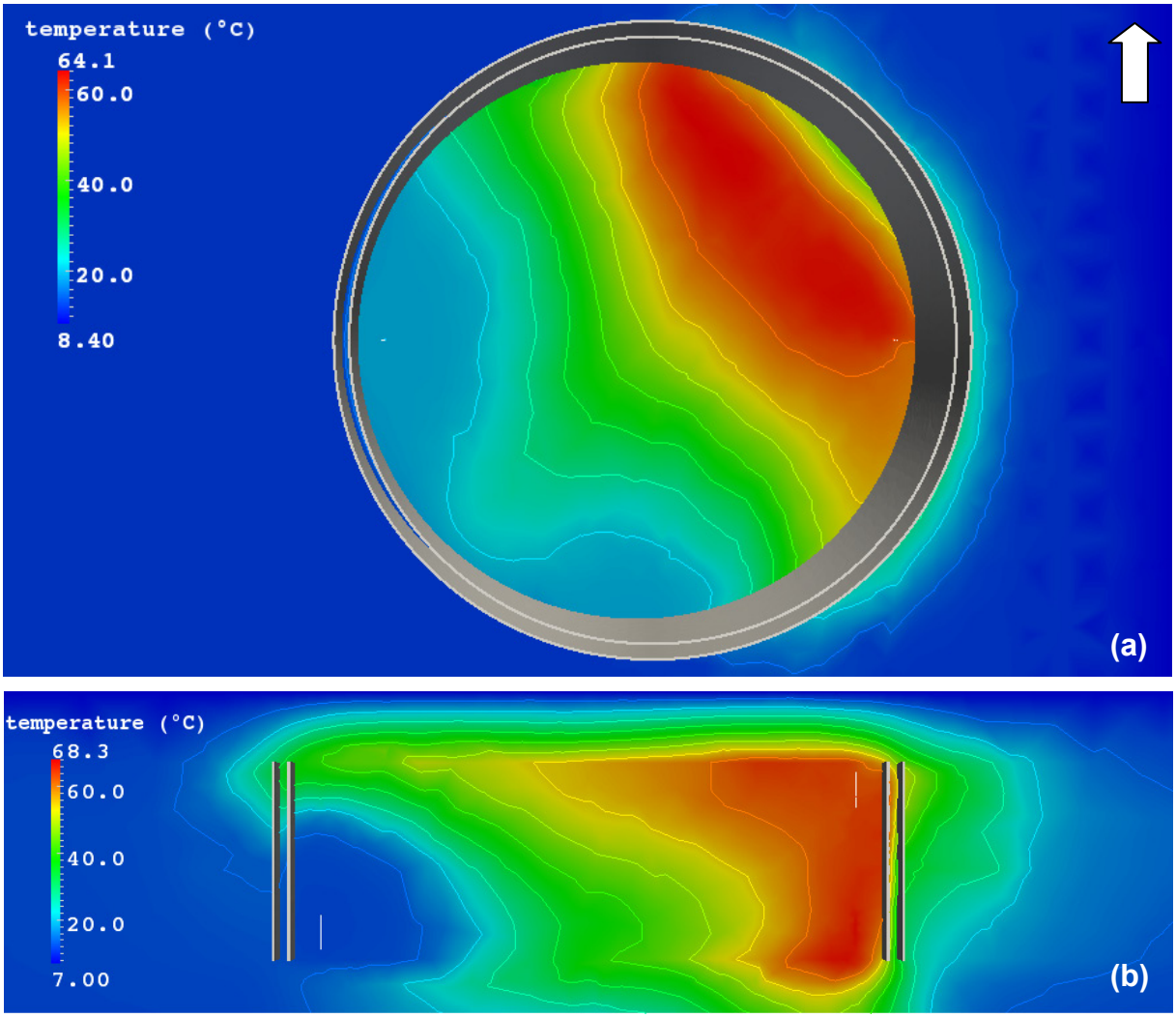

Fig. 4.19: Temperature cross section of discharging for Run 3 a) Horizontal cut-plane through injection well 3 (left) and production well 1 (right) showing the temperature distribution after 20 days of discharging. b) Vertical cut-plane through injection well 3 (left) and production well 1 (right) after 20 days. The hottest region inside the storage is at the top left, at the location of the production well. The hottest region outside the storage is in the clay marl region below injection well 1. Temperature contours are separated by 10°C

For Run 5 I have changed the charging strategy. I inject the hot fluid at the top and not at the bottom as in the previous runs. The idea is to reduce mixing of hot and cold fluid during charging and thus get a better thermal stratification inside the storage. The simulation parameters for the charging process of Run 5 are shown in Table 4.7 and for the discharging process in Table 4.4. The well configuration for discharging is the same as for Run 2.

Table 4.7: Simulation parameters for Run 5

Simulation Parameters for charging	Symbol	Unit	Value
Initial domain temperature	T_i	°C	12
Injection well temperature at production well 1	T_{inj}	°C	85
Reference pressure	p_{ref}	Pa	101325
Injector absolute rate at "production well 1"	q	m^3/s	0.00108
Producer absolute rate at "injection well 3"	q	m^3/s	-0.00108
Time step	Δt	days	1
Total simulation time	t	days	120

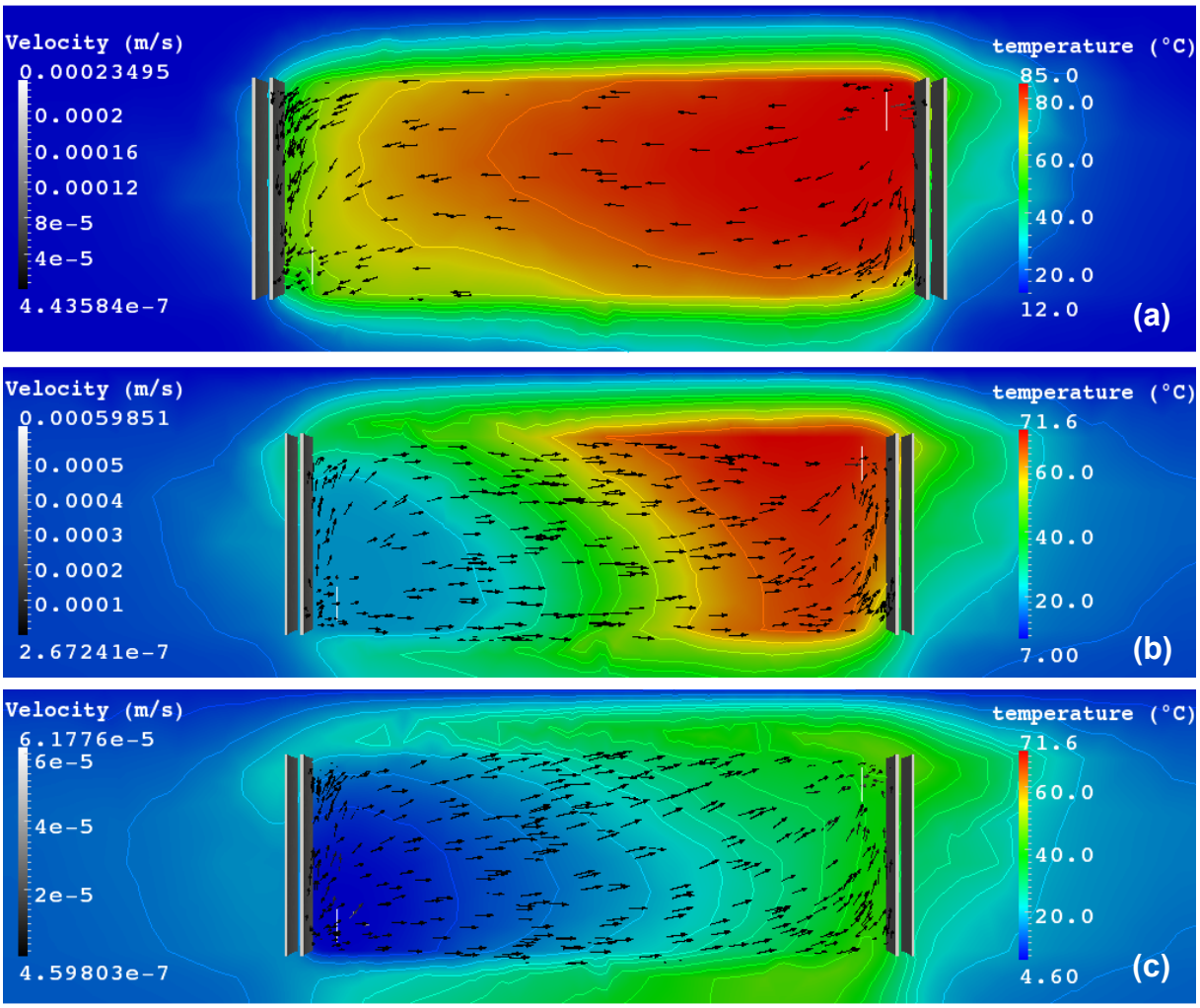

Fig. 4.20: Temperature cross section and velocity vectors for Run 5. a) Vertical cut-plane through the injection well (right) and the production well (left) after 120 days of charging the storage system with 85°C hot fluid. The hottest region is at the top of the storage system. Fluid moves from left to right and cools down as it approaches the producer and consequently moves downward. b) Vertical cut-plane through the injection well (left) and the production well (right) after 20 days of discharging the storage system. c) Vertical cut-plane through both wells after 56 days of discharging The temperature at the production well is about 38°C.

Fig. 4.20 shows the temperature distribution of the storage system and its surrounding during the charging and discharging phase after 20 and 56 days. Due to diffusion a relative high amount of heat spreads downward during charging (Fig. 4.20a). The temperature distribution during discharging looks similar as in Run 2.

For Run 6 I have used a new well location. Production well 6 is in the center and near the top of the storage system. During charging I inject hot fluid at this well and produce the cold fluid from all 4 injection wells at the bottom. In the discharging process the well configuration is vice versa. The simulation parameters for the charging process of Run 6 are shown in Table 4.8 and for the discharging process in Table 4.4.

Table 4.8: Simulation parameters for Run 6

Simulation Parameters for charging	Symbol	Unit	Value
Initial domain temperature	T_i	°C	12
Injection well temperature at production well 1	T_{inj}	°C	85
Reference pressure	p_{ref}	Pa	101325
Injector absolute rate at "production well 6"	q	m^3/s	0.00108
Producer absolute rate at "injection well 1,2,3,4"	q	m^3/s	-0.00027
Time step	Δt	days	1
Total simulation time	t	days	120

Fig. 4.21 shows the temperature distribution of the storage system and its surrounding during the charging and discharging phase after 20 and 56 days. Due to diffusion a relative high amount of heat spreads downward during charging (Fig. 4.21a) The hottest regions during discharging (Fig. 4.21b) are near the top of the storage system.

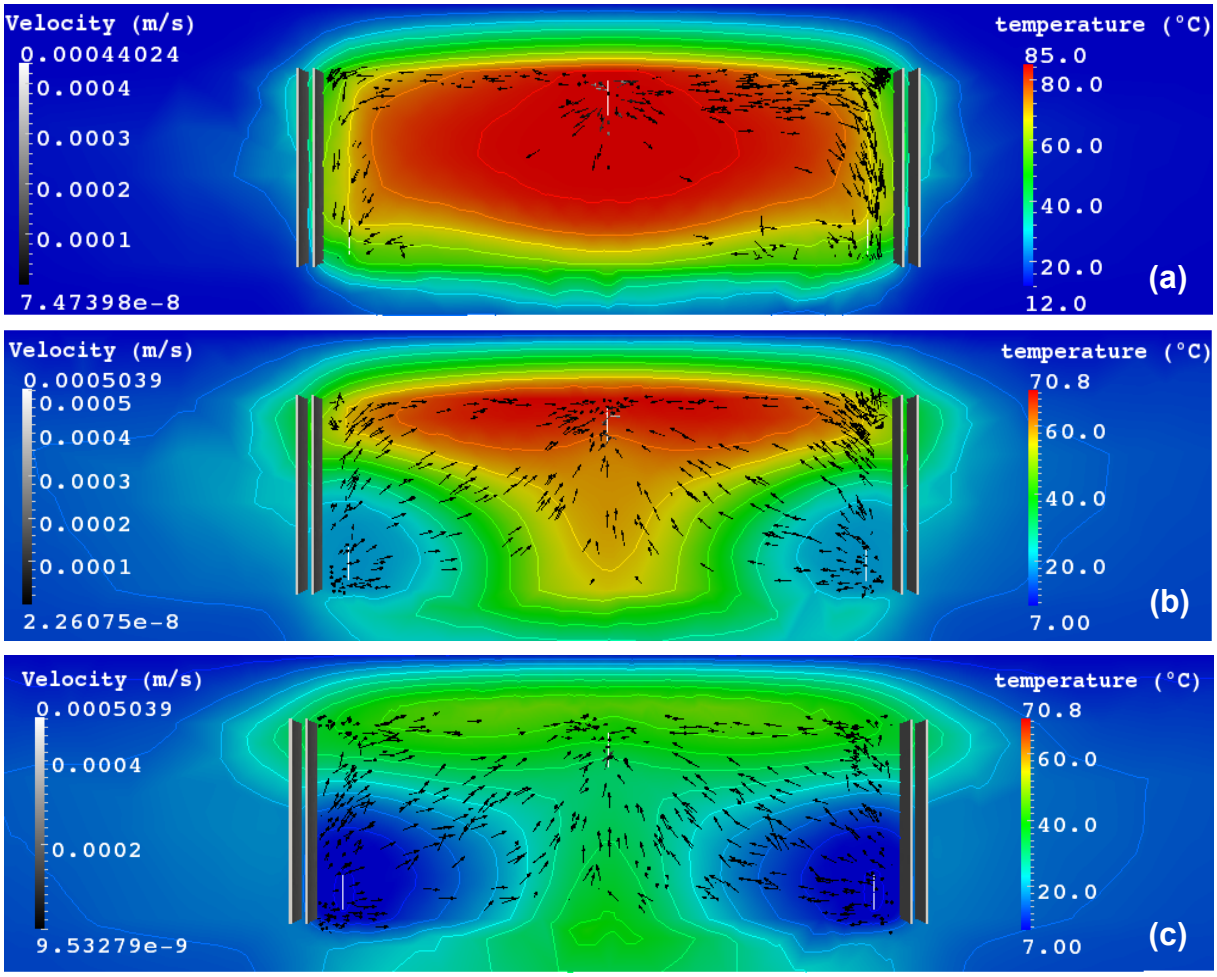

Fig. 4.21: Temperature cross section and velocity vectors for Run 6. a) Vertical cut-plane through the injection well (centered) and the production wells (left and right) after 120 days of charging the storage system with 85°C hot fluid. The hottest region is at the top of the storage system. Fluid moves from the center to left and right and cools down as it approaches the producer and consequently moves downward. b) Vertical cut-plane through the injection well (centered) and the production well (left and right) after 20 days of discharging the storage system. c) Vertical cut-plane after 56 days of discharging.

The graphs below (Fig. 4.22) show the energy and exergy input for the 4 different charging strategies. They are calculated using equation (4.1) and (4.2). The highest energy input is achieved by charging the storage from the top (Run 5) and the lowest by charging from the bottom with two wells (Run 3). It is also seen that the final temperature at the production well is for all runs about the same.

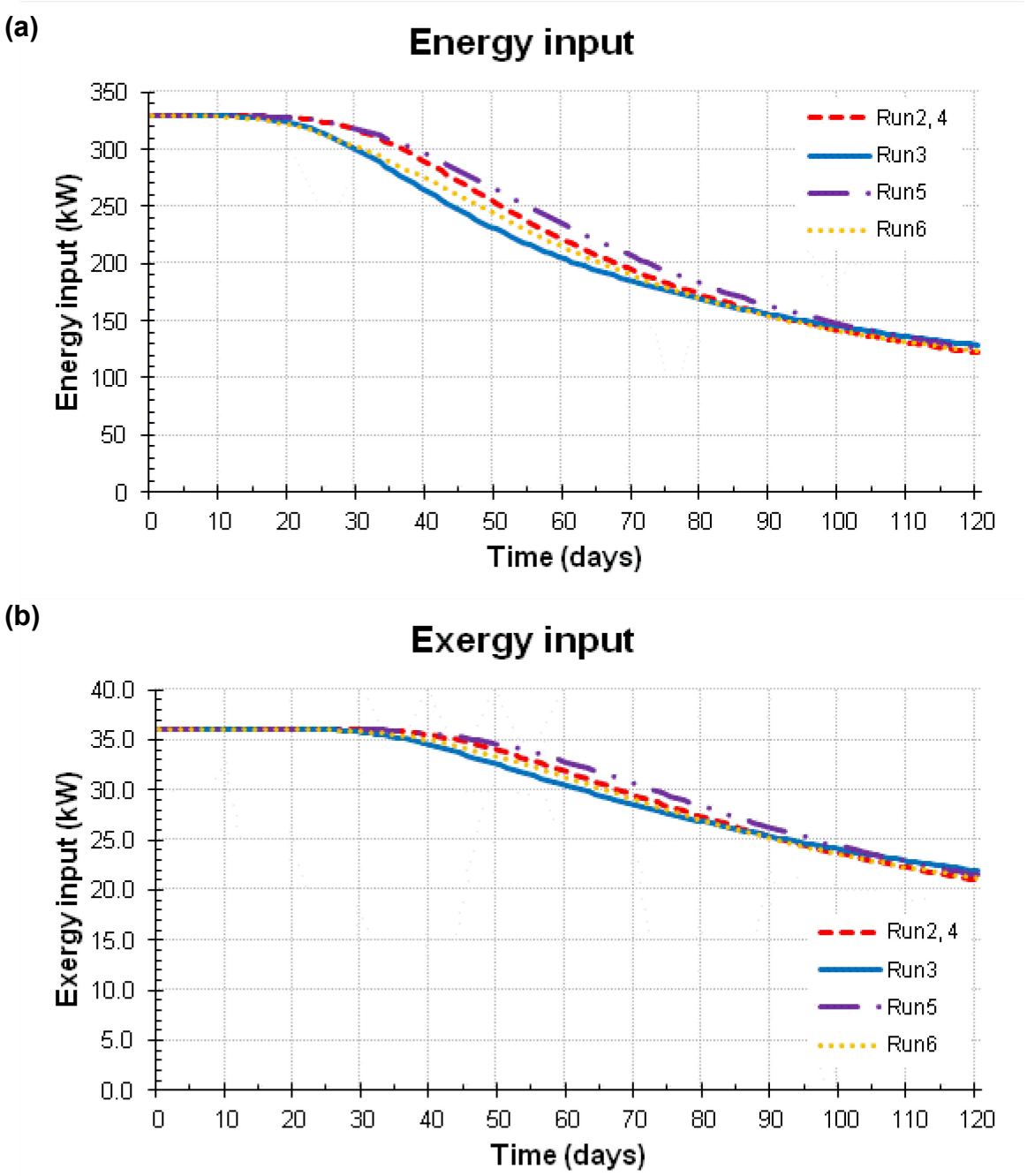

Fig. 4.22: a) Energy flow rate over the 120 days charging period for Run 2 - 6. At temperature breakthrough - after about 25 days - the energy flow rate starts decreasing due to decreasing temperature difference between injection and production well. b) Exergy flow rate over the 120 days charging period for Run 2 - 6.

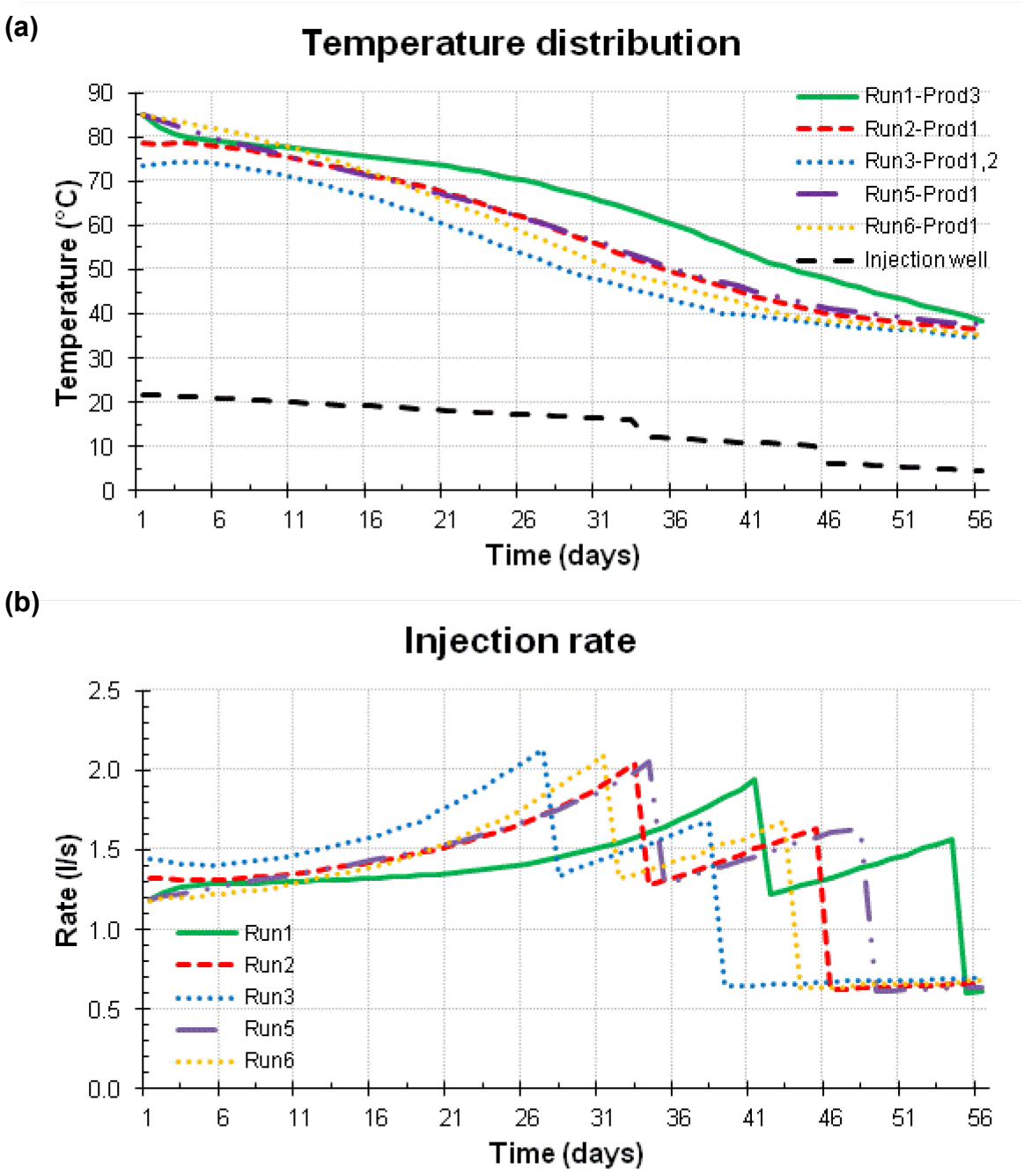

Fig. 4.23: a)Temperature at the production well(s) during the discharging period for Run 1 - 6 and temperature at the injection well. The temperature at the injection well for Run 2. At the discontinuities the discharging process changes the operation mode. b) Injection rate during the discharging phase for Run 1 - 6. The discontinuities are the consequence of the 3 different operation modes during the discharging process.

The temperature profiles at the production well during the discharging phase are shown in Fig. 4.23a. A closer look to the temperature distribution in the first week show a quite constant temperature for Run 2 and 3, which are charged with hot fluid from the bottom. This could be, because the region at the bottom is a bit hotter than at the top, which causes fluid movement of hot water to the top.

As already mentioned the injection rate during discharging changes to deliver a constant energy to the corn drying process. This is possible by increasing the injection rate while output temperature decreases. The discontinuities in the injection rates are the consequence of the different operation modes during the discharging process. Fig. 3.15 explains the three operation modes. As long as the storage system can deliver a certain temperature (52°C for Run 1, 2, 4, 5, 6) operation mode 1 is active. However, if the temperature decreases below this value, operation mode 2 becomes active. The longer the first mode is active, the more energy can be delivered to the corn drying process. In this case Run 1 delivers the most energy.

To analyze the efficiency of a thermal energy storage system energy and exergy analyses are performed. The energy efficiency of a storage system is the ratio of energy recovered from the storage to that originally input (Dincer and Rosen, 2002) and calculated with following formula:

$$\eta = \frac{Energy\ recovered\ from\ UTES\ during\ discharging\ E_d}{Energy\ input\ to\ UTES\ during\ charging\ E_c} = \frac{\dot{m}_d c t_d (T_{out} - T_{in})}{\dot{m}_c c t_c (T_{in} - T_{out})} \qquad (4.3)$$

The exergy efficiency is defined as:

$$\psi = \frac{Exergy\ recovered\ from\ UTES\ during\ discharging\ \varepsilon_d}{Exergy\ input\ to\ UTES\ during\ charging\ \varepsilon_c} = \frac{E_d - \dot{m}_d c t_d T_0 \ln\left(\frac{T_{out}}{T_{in}}\right)}{E_c - \dot{m}_c c t_c T_0 \ln\left(\frac{T_{in}}{T_{out}}\right)} \qquad (4.4)$$

For the calculation of energy and exergy it is assumed that the heat capacity of water and the ambient air temperature is constant.

The energy and exergy flow rate for all 6 runs are shown in Fig. 4.24 and the energy and exergy efficiency are shown in Table 4.9 and Table 4.10. There are no major efficiency differences for all 6 runs, however the highest energy and exergy output is achieved with Run 5.

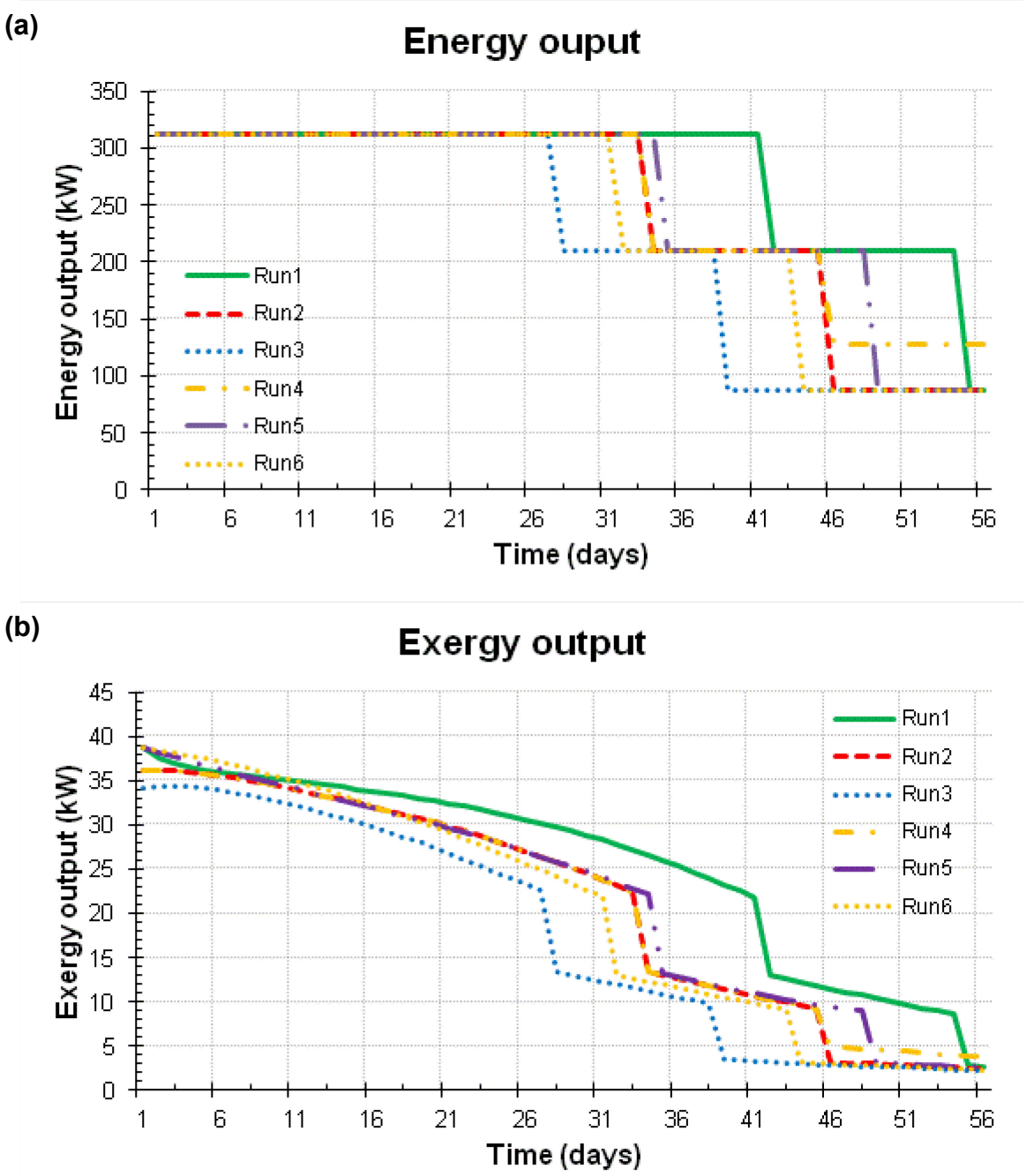

Fig. 4.24: Energy and exergy flow rate during the discharging period. a) The energy flow rate during an operation mode is because of a variable injection rate constant. The longer an operation mode can be maintained, the more energy can be delivered to the corn drying process. b) Exergy flow rate for all 6 runs.

Table 4.9: Energy analyses of the storage system for Run 1 - 6

	Energy Input (MWh)	Energy Output (MWh)	Unused Energy (MWh)	Efficiency (%)
Run 1	---	377.3	---	---
Run 2	666.5	331.3	335.2	49.7
Run 3	645.4	296	349.4	50
Run 4	666.5	341.6	324.8	51
Run 5	684.4	342.5	341.9	50
Run 6	651.2	320.5	330.7	49.2

Table 4.10: Exergy analyses of the storage system for Run 1 - 6

	Exergy Input (MWh)	Exergy Output (MWh)	Unused Exergy (MWh)	Efficiency (%)
Run 1	---	34.4	-	-
Run 2	88.5	28.5	60	32.2
Run 3	87.5	23.7	63.8	32
Run 4	88.5	28.9	59.6	33
Run 5	90.0	29.4	60.6	32.7
Run 6	87.8	27.5	60.3	31.3

5. Discussion

There are different types of UTES and simulation software to model them. The storage system in this thesis is similar to a gravel-water pit, but it uses the natural underground for the storage of hot water. Except of the artificial walls there are no artificial structures in the UTES. The gravel - water storage in Chemnitz (Benner et al., 2003) is similar to the storage presented in my thesis. The storage volume is about 8000 m^3 , and rock properties like porosity, heat conduction and heat capacity are similar. The gravel is very well sorted and has therefore a small standard deviation of grain size, which yields a very high permeability. Calculations and charging and discharging strategies for gravel - water storage systems were performed by the University of Chemnitz (Urbaneck et al., 2002, 2003). TRNSYS software, type 343 (Hornberger, 1997) from the component library was used to simulate. This type is used for vertically stratified storage beds for heat and cold storage.

The strategy for charging and discharging the UTES is very similar (Sweet and McLeskey Jr., 2012; Urbaneck et al., 2003). Usually for charging hot water is injected at the top and cold water is produced at the bottom and for discharging cold water is injected at the bottom and hot water is produced from the top. I have used the same strategy for discharging and also consider that injection and production wells have the greatest possible distance. This strategy avoids major mixing of hot and cold water inside the storage and allows producing hot water for a long time, because of a late temperature breakthrough of cold water.

I charged the simulator with hot water from the bottom and from the top. The output energy and efficiency is for both strategies about the same and therefore not so important for this application. The charging strategy from the bottom is just applicable if heat in the UTES is transferred by a certain amount of diffusion so that thermal stratification in the storage is relative low. Furthermore the diameter of the UTES should not be smaller than 30m. However, generally UTES should be charged with hot water from the top to support thermal stratification.

The usage of a greater number of injection and production wells allows for wider distribution of hot and cold water. However such well configurations yield to a slightly

lower energy output, because of the low concentration of hot water which leads to lower temperatures at the production well.

6. Conclusions

This thesis presents the simulation of heat transport in an underground thermal storage facility with and without a corn drying control system (CDCS). The thermal reservoir simulator is part of this optimization program, replacing the real world system. It has to account for daily and seasonal changes which affect corn drying. The created simulator is based on the Boussinesq approximation and uses the CSMP++ software library. It is based on the hybrid finite-element finite-volume discretization method, which uses operator splitting for solving advection -dominated problems, with the capability of FEM to handle diffusion-dominated problems. The simulator is verified by comparing the numerical solution with analytical ones, as well as benchmarking it against TOUGH ("Transport of Unsaturated Groundwater and Heat") simulator and the PHT ("Pressure Enthalpy Temperature") simulator. PHT is a compressible flow simulator, also generated from the CSMP++ libraries. The geothermal simulator used in this thesis achieves simulation capabilities beyond those of the PHT simulator.

The simulation results indicate following characteristics on flow behavior and heat transfer in the storage system:

- The hotter regions are at the top of the storage, because the density of hot water is lower than of cool one and hence moves upward.
- Due to heat conduction through the walls the unsaturated gravel region outside of the storage is heated, also the region below, where groundwater flow occurs.
- The velocity magnitude within the storage is in the range of 10^{-5} and 10^{-7} m/s and is the highest in the vicinity of the wells and near the storage walls.
- The highest amount of heat is lost through the artificial walls of the storage system. The high temperature difference between storage inside and the region of groundwater flow could be a reason for that.

The different charging and discharging simulations with the control system show that the following strategy is the most efficient:

- The charging and discharging of the storage should be as quick as possible, meaning that injection and production should be at the highest possible rate to reduce diffusive heat loss through the storage walls. Also, any storage period (i.e without and injection or production) should be avoided.
- The UTES can be charged with hot water injected at the bottom or at the top, if there is no storage period. However the energy output is a slightly higher, if the UTES is charged with hot water injected at the top.
- In the discharging process the production wells should be located in the hotter regions near the top and the walls, and the injection wells near the bottom. Furthermore, the distance between injection and production wells should be as far as possible to avoid an early temperature breakthrough.

7. Outlook

To further improve the discharging of the UTES and with it the efficiency of the corn drying process, a sensitivity analysis will be performed. There are still many options to change the well configurations or well locations to investigate the impact to the corn drying process. Charging and discharging the storage system using up to 9 wells is with the actual model possible, however new well locations could also be added. Parameters from the calculation sheet of the corn drying process could be changed. The preheating air stream temperature can be changed to modify the three different operation modes during the discharging process. Initial water content of the corn and other input parameters can be varied to achieve a higher outcome. Further a new storage geometry can be created and simulated.

8. References

Ahmed, Tarek (2006): *Reservoir Engineering Handbook*. Third Edit. Elsevier. — ISBN: 9780750679725

Arpaci, V. S.; Selamet, A.; Kao, S. (2000): *Introduction to Heat Transfer*. Prentice-Hall. — ISBN: 013391061X

Bakema, G.; Snijders, A.L.; Nordell, B. (1995): *Underground Thermal Energy Storage - State of the Art 1994*. Arnheim

Baliga; Patankar (1980): „A new finite element formulation for convection diffusion problems“. In: *Numerical Heat Transfer*. 6 , pp. 245 - 261.

Bear, J. (1972): *Dynamics of Fluids in Porous Media*. American Elsevier Publishing Company.

Bejan, A. and Kraus, A.D. (2003): *Heat Transfer Handbook*. John Wiley & Sons, Inc.

Benner, M.; Bodmann, M;; Mangold, D.; et al. (2003): *Solar unterstützte Nahwärmeversorgung mit und ohne Langzeit-Wärmespeicher*. Universität Stuttgart. — ISBN: 3980527425

Bird, R.B.; Stewart, W.E.; Lightfood, E.N. (2007): *Transport Phenomena*. Second Ed. John Wiley & Sons, Inc.

Boussinesq, Joseph (1897): *Théorie de l'écoulement tourbillonnant et tumultueux des liquides dans les lits rectilignes a grande section*. Paris, Gauthier-Villars et fils.

Coumou, Dim; Driesner, Thomas; Geiger, Sebastian; et al. (2006): „The dynamics of mid-ocean ridge hydrothermal systems Splitting plumes and fluctuating vent temperatures“. In: *Earth and Planetary Science Letters*. 245 , pp. 218-231

Darcy, H. (1856): *Les Fontaines Publiques de la Ville de Dijon*. Paris.

Dincer, I. and Rosen, M.A. (2002): *Thermal Energy Storage Systems and Applications*. Second Edi. John Wiley & Sons, LTD. — ISBN: 9780470747063

Eftring, B. and Hellström, G. (1989): „Stratified Storage Temperature Model“. Lund, Sweden.

FFG (2011): *Basisprogramm - Nutzbarmachung von geologischen Strukturen, zum Zweck der thermischen Energiespeicherung*.

Fourier, Joseph (1829): *Théorie analytique de la chaleur*. Paris.

Geiger, S; Driesner, T; Heinrich, C A; et al. (2005): „On the dynamics of NaCl-H 2 O fluid convection in the Earth ' s crust“. In: *Journal of Geophysical Research*. 110

Geiger, Sebastian; Driesner, Thomas; Heinrich, Christoph A; et al. (2006a): „Multiphase Thermohaline Convection in the Earth ' s Crust . A New Finite Element – Finite Volume Solution Technique Combined With a New Equation of State for NaCl – H 2 O". In: pp. 399-434

Geiger, Sebastian; Driesner, Thomas; Heinrich, Christoph A; et al. (2006b): „Multiphase Thermohaline Convection in the Earth ' s Crust II . Benchmarking and Application of a Finite Element – Finite Volume Solution Technique with a NaCl – H 2 O Equation of State". In: pp. 435-461

Geiger, Sebastian; Emmanuel, Simon (2010): „Non-Fourier thermal transport in fractured geological media". In: *Water Resources Research*. 46 , pp. 1-13

Haar, J.S.; Gallagher, L.; Kell, G.S. (1984): *NBS/NRC Steam Tables*. Washington D.C.

Hess, H. (1840): *Thermochemische Untersuchungen, Annalen der Physik und Chemie*. Poggendorff, Leipzig.

Hornberger, M. (1997): *ICEPIT. Simulationsprogramm für vertikal geschichteten Erdbecken-Speicher zur Wärme- und Kältespeicherung*. Stuttgart.

Ievers, Simon; Lin, Wenxian (2009): „Numerical simulation of three-dimensional flow dynamics in a hot water storage tank". In: *Applied Energy*. Elsevier Ltd 86 (12), pp. 2604-2614

Incropera, F.P.; Dewitt, D.P.; Bergman, T.L. et al. (2007): *Fundamentals of Heat and Mass Transfer*. Sixth Edit. John Wiley & Sons.

Ingebritsen, S.E.; Sanford, W.E. (1998): *Groundwater in Geologic Processes*. Cambridge University Press.

Ingebritsen, S.E.; Sanford, W.E.; Neuzil, C. (2006): *Groundwater in Geologic Processes*. New York: Cambridge University Press.

Kaviany, M. (2011): *Essentials of Heat Transfer*. Cambridge University Press. — ISBN: 9781107012400

Kawada, Yoshifumi; Yoshida, Shigeo; Watanabe, Sei-ichiro (2004): „Numerical simulations of mid-ocean ridge hydrothermal circulation including the phase separation of seawater, In: pp. 193-215.

Kreith, F.; Manglik, R.M.; Bohn, M.S. (2010): *Principles of Heat Transfer*. Pacific Grove, Calif.: Brooks/Cole.

Lindblom, U (1980): „UTILIZATION OF UNDERGROUND FOR SOLAR AND WASTE HEAT STORAGE“. In:

Matthäi, S K; Geiger, S; Roberts, S G (2001): *Complex Systems Platform: CSP3D3.0: User's Guide*.

Müller, E.; Schön, J. (2012): *Bodenphysikalische Parameter : Erste Versuchsreihe*.

Nield, D A; Barletta, A (2010): „Extended Oberbeck – Boussinesq approximation study of convective instabilities in a porous layer with horizontal flow and bottom heating“. In: *International Journal of Heat and Mass Transfer*. Elsevier Ltd 53 (4), pp. 577-585

Novo, Amaya V; Bayon, Joseba R; Castro-fresno, Daniel; et al. (2010): „Review of seasonal heat storage in large basins: Water tanks and gravel – water pits“. In: *Applied Energy*. Elsevier Ltd 87 (2), pp. 390-397

Ogata, A.;; Banks, R.B. (1961): „A Solution of the Differential Equation of Longitudinal Dispersion in Porous Media“. In: *U.S. Geological Survey Professional Paper*.

Paluszny, A.; Matthäi, S. K.; Hohmeyer, M. (2007a): „Hybrid finite element – finite volume discretization of complex geologic structures and a new simulation workflow demonstrated on fractured rocks“. In: *Geofluids*. 7 , pp. 186-208

Paluszny, a.; Matthäi, S. K.; Hohmeyer, M. (2007b): „Hybrid finite element-finite volume discretization of complex geologic structures and a new simulation workflow demonstrated on fractured rocks“. In: *Geofluids*. 7 (2), pp. 186-208

Papanicolaou, E.; Belessiotis, V. (2009): „Transient development of flow and temperature fields in an underground thermal storage tank under various charging modes“. In: *Solar Energy*. Elsevier Ltd 83 (8), pp. 1161-1176

Refsgaard, J. C. and Henriksen, H. J. (2004): „Modelling guidelines - terminology and guiding principles“. In: *Advances in Water Resources*. 27 , pp. 71-82.

Reuß, M; Beuth, W; Schmidt, M; et al. (2006): „Solar District Heating with Seasonal Storage in Attenkirchen“. In: *Applied Energy*. New Jersey.

Reuß, Manfred (2003): *Saisonale Wärmespeicherung im Untergrund – eine Lösung für die effiziente Wärmenutzung auch bei Biogas ?* Garching.

Rysanek, Adam M (2009): „SECOND LAW PERFORMANCE ANALYSIS OF A LARGE THERMAL ENERGY STORAGE VESSEL USING CFD“. Queen's University.

Schmidt, T. (2005): „Erdsonden- und Aquifer-Wärmespeicher in Deutschland“.

Schmidt, Thomas (2007): „Solare Nahwärme mit saisonaler Wärmespeicherung in Deutschland“. *Solites*. Retrieved am from http://www.carmen-ev.de/dt/portrait/symposien/symp_11/vortraege_symp_11/schmidt_symp_11.pdf.

Schoofs, Stan (1999): „Thermochemical Convection in Porous Media. An Application to Hydrothermal Systems and Magmatic Intrusions“. Geologica Ultraiectina. — ISBN: 9057440369

Strang, Gilbert (1968): „On the Construction and Comparison of Difference Schemes“. In: *SIAM Journal on Numerical Analysis, vol. 5, no. 3, pp. 506-517*.

Stüben, K. (2002): *User's Manual SAMG Release 21b1*. St. Augustin, Germany.

Sweet, M.L; McLeskey Jr., J.T (2012): „Numerical simulation of underground Seasonal Solar Thermal Energy Storage (SSTES) for a single family dwelling using TRNSYS“. In: *Solar Energy*. Elsevier Ltd 86 (1), pp. 289-300

Terziotti, L.T.; Sweet, M.L.; McLeskey, J.T. (2012): „Modeling seasonal solar thermal energy storage in a large urban residential building using TRNSYS 16“. In: *Energy and Buildings*. Elsevier B.V. 45 , pp. 28-31

Ucar, A; Inalli, M (2005): „Thermal and economical analysis of a central solar heating system with underground seasonal storage in Turkey“. In: 30 , pp. 1005-1019

Urbaneck, T.; Platzer, B.; Schirmer, U. (2002): *Berechnung von Kies-Wasser-Speichern*. Regensburg.

Urbaneck, Thorsten; Platzer, Bernd; Schirmer, Ulrich (2003): „Direkte Be- und Entladung von Kies-Wasser-Speichern“. In:

Yumrutas, R (2000): „Analysis of solar aided heat pump systems with seasonal thermal energy storage in surface tanks“. In: 25 , pp. 1231-1243.

Appendix

A.1 Dimensionless Numbers

There are two important dimensionless numbers, which are useful in heat transport theory. The first one is the Peclet number, which defines the ratio between rate of transport by convection to the rate of transport by diffusion (Arpaci et al., 2000; Bear, 1972):

$$Pe = \frac{v\Delta x}{\kappa}$$

Where v [m/s] is the velocity, Δx [m] a characteristic length and αm [m ^{2}/s] is the thermal diffusivity. The second one is the Rayleigh number, which tells if a fluid transfer heat via conduction or convection (Bear, 1972),

$$Ra = \frac{g\beta\Delta TL^3}{\kappa\nu}$$

where β [1/K] is the coefficient of thermal expansion, L [m] is a representative length and v [m^2/s] is the kinematic viscosity. A high Rayleigh number indicates heat transfer primarily in form of convection (Ingebritsen, Sanford, 1998).